creative commons
COMMONS DEED

저작자표시-비영리-변경금지 2.0 대한민국

이용자는 아래의 조건을 따르는 경우에 한하여 자유롭게

- 이 저작물을 복제, 배포, 전송, 전시, 공연 및 방송할 수 있습니다.

다음과 같은 조건을 따라야 합니다:

저작자표시. 귀하는 원저작자를 표시하여야 합니다.

비영리. 귀하는 이 저작물을 영리 목적으로 이용할 수 없습니다.

변경금지. 귀하는 이 저작물을 개작, 변형 또는 가공할 수 없습니다.

- 귀하는, 이 저작물의 재이용이나 배포의 경우, 이 저작물에 적용된 이용허락조건을 명확하게 나타내어야 합니다.
- 저작권자로부터 별도의 허가를 받으면 이러한 조건들은 적용되지 않습니다.

저작권법에 따른 이용자의 권리는 위의 내용에 의하여 영향을 받지 않습니다.

이것은 이용허락규약(Legal Code)을 이해하기 쉽게 요약한 것입니다.

Disclaimer

dCollection

공학박사 학위논문

Functional reconstitution of G protein-coupled receptor produced in *Escherichia coli* and its applications to the high-performance biosensor

대장균에서 생산된 G 단백질 연결 수용체의
기능적 재구성 및 고성능 바이오센서로의 응용

2018년 2월

서울대학교 대학원
공과대학 화학생물공학부
양 희 홍

Abstract

Functional reconstitution of G protein-coupled receptor produced in *Escherichia coli* and its applications to the high-performance biosensor

Heehong Yang

School of Chemical and Biological Engineering

The Graduate School

Seoul National University

G protein-coupled receptors (GPCRs) are membrane proteins that have seven trans-membrane domains, which are significantly involved in many human diseases and 40% of all drug targets. For this reason, a platform containing stable and high-quality GPCR would be useful for the development of biosensor that can be applied to various fields, such as early diagnosis of diseases, environmental monitoring and drug screening. Significant efforts have been made to develop the GPCR-conjugated biosensor by combining the nanomaterials and biomolecules, such as protein, cell-derived nanovesicle and GPCR-expressing cells. Especially, the protein-based biosensor could have a great advantage in sensitivity, selectivity,

reproducibility, reusability and quantitative analysis. For the production of recombinant proteins, the *Escherichia coli* (*E. coli*) has been widely used as a host cell because of its great advantage in productivity and convenience. However, the production of GPCR in *E. coli* remains a challenge because of their strong hydrophobicity, a complicated charge distribution and different membrane inserting mechanism.

The functional reconstitution technique of GPCRs has been considered to be important tool for more stable and accurate receptor-based research. These techniques have been studied to acquire basic knowledge of the crystal structure, receptor-signaling and pharmacological research. Many studies have suggested that highly purified and well-reconstituted receptor could have native-like receptor structure and binding pocket. Especially, the receptor-embedded nanodiscs (NDs) have been considered to be a powerful tool for qualitative and quantitative biophysical analysis on receptor/ligand binding details and could be applied to practical biosensor, which can be used to various fields, such as assessment of food quality, disease diagnosis and drug-interaction researches.

In this thesis, GPCRs were produced in *E. coli* with high productivity, solubilized with detergent and purified with column chromatography. Then, the functional reconstitutions of purified receptors as a detergent micelles or NDs were successfully optimized and their characteristics were monitored and analyzed. Their binding properties were also confirmed by comparing it with the responses in cell-based assay. And, they were applied to nano-electronic sensors using field-effect transistor (FET) to develop the protein-based platforms, which lead to high-performance biosensor.

First, the receptor-based analysis method for studying receptor agonism and

antagonism was developed. The dopamine receptor D1 (DRD1)-conjugated FET system was constructed by combining the FET and reconstituted DRD1 protein, which is a suitable substitute for conventional cell-based receptor assays. The DRD1 was purified and reconstituted to mimic native binding pockets that have highly discriminative interaction toward DRD1 agonists/antagonists. The real-time responses from the DRD1-nanohybrid FET were highly sensitive and selective for dopamine agonists/antagonists, and their maximal response levels were clearly different depending on their DRD1 affinities. And, they could successfully demonstrate the DRD1 agonism and antagonism.

Second, for the more stabilization of the functional receptors, the receptor-embedded NDs were successfully optimized and assembled. A trace amine-associated receptor 13c (TAAR13c) binding to death-associated odor cadaverine (CV) was produced in *E. coli*, purified and reconstituted into NDs. Their characteristics were analyzed by tryptophan fluorescence assay, dynamic light scattering and scanning electron microscopy. Also, they were applied to a carbon nanotube (CNT)-based FET with floating electrodes with desired orientation. The ND-based biosensor showed high-performance in terms of sensitivity and selectivity. Moreover, they could measure CV in diverse real-food samples for the determination of food freshness.

Third, the T13ND-conjugated Ni-decorated conducting polymer nanoparticle in FET was successfully constructed to develop the high-performance biosensor platform detecting the liquid and gaseous target. In this platform, the T13NDs could mimic the native-like binding pocket of natural receptor and exist with high-stability in the aqueous and dried conditions. The conducting polymer nanoparticle could enhance the sensor sensitivity and enable to the oriented immobilization of

NDs on the FET. The ND-based biosensor can have a high stability and reliability as well as a high sensitivity and selectivity in aqueous condition. Furthermore, they also could detect the gaseous CV with high sensitivity, stability and reusability.

Lastly, the human-like performance bioelectronic nose was successfully constructed to mimic the human sensory responses using receptor-based platform. The human olfactory receptor 1A2-embedded NDs (hOR1A2NDs) were assembled and applied to the CNT-FET with floating electrode; this is termed a bioelectronic nose. The hOR1A2NDs responded to rose scent molecules specifically, which were monitored electrically using the underlying CNT-FET. This strategy allowed the quantitative assessment of the specific rose scents with sensitivity and selectivity. Significantly, the enhanced responses of hOR1A2NDs to a rose scent by enhancer material were successfully demonstrated like a human nose. Furthermore, the method provided a means to quantitatively evaluate rose scent components in real samples such as rose oil.

As a result, the protein-based bioelectronic sensors exhibit high-performance in terms of sensitivity, selectivity, reproducibility, stability and quantitative analysis. Also, they could successfully mimic receptor agonism and antagonism, and the human olfactory response as well as detect the liquid and gaseous target molecule. This platform can be used as a practical method for the receptor-based sensing approach, which represents significant progress in nano-bio technology toward a practical biosensor.

Keywords: G protein-coupled receptor, *Escherichia coli*, purification, reconstitution, nanodiscs, biosensor

Student Number: 2014-30249

Contents

List of Figures

List of Abbreviations

GPCRs: G protein-coupled receptors

E. coli: *Escherichia coli*

ND: nanodiscs

MSP: membrane scaffold protein

CV: cadaverine

SDS: sodium dodecyl sulfate

DDM: dodecyl-β-D-maltoside

Cymal 6: 6-cyclohexylhexyl-β-D-maltoside

OG: n-octyl-β-D-glucopyranoside

CMC: critical micelle concentration

POPC: palmitoyloleoylphosphatidylcholine

POPG: palmitoyloleoylphosphatidylglycerol

CD: circular dichroism

DLS: dynamic light scattering

IPTG: isopropyl thiogalactoside

HEK: human embryonic kidney

SDS-PAGE: sodium-dodecyl-sulfate-polyacrylamide gel electrophoresis

PBS: phosphate-buffed saline

TAARs: trace amine-associated receptors

ORs: olfactory receptors

DRs: dopamine receptors

DMEM: Dulbecco's Modified Eagles Medium

FBS: Fetal Bovine Serum

SEC: size exclusion chromatography

cAMP: cyclic adenosine monophosphate

CREB: cAMP response element-binding protein

HR-TEM: high-resolution transmission electron microscopy

FE-SEM: field-emission scanning electron microscopy

MEMS: microelectromechanical system

IMA: interdigitated microelectrode array

FET: field-effect transistor

ssCNTs: single-walled carbon nanotubes

CPPy: carboxylated polypyrrole

Chapter 1

Research background and objective

Research background and objective

G protein-coupled receptors (GPCRs) are transmembrane proteins that are comprised of seven α-helical domains [1]. They are involved in diverse physiological processes, such as hormonal signaling, neuronal transmission, sensory signaling and cell signal transduction [2]. They account for approximately 50% of all human drug targets for various diseases, containing targets for cancer, metabolic, inflammatory and central nervous system diseases [3]. For this reason, many researchers have studied the expression, purification and functional reconstitution of GPCR for more stable and accurate receptor-based research; however, they remain as a challenging due to their complicated structure and strong hydrophobicity [4-6].

The purification and functional reconstitution of GPCRs have been considered to highly important for more stable and accurate receptor-based research. These techniques have been studied to acquire basic knowledge of the crystal structure, receptor-signaling and pharmacological research. Moreover, many studies have suggested that highly purified and well-reconstituted receptor, which is assembled by membrane-like environments, can have native receptor structure and natural binding pocket [7,4,5]. The purified and well-reconstituted GPCRs can be used as a powerful tool for qualitative and quantitative biophysical information on receptor/ligand binding details [8,4]. In addition, a high-quality receptor can be integrated into nanobio-technologies in various fields, such as clinical diagnosis, health control and drug discovery, leading to a high-performance human sensory system [9,5,10].

For the production of recombinant proteins, the *Escherichia coli* (*E. coli*) has

been widely used as a host cell because of its great advantage in productivity and convenience [11]. However, the production of GPCR in *E. coli* remains a challenge because of their strong hydrophobicity, a complicated charge distribution and different membrane inserting mechanism [12]. Especially, the production of GPCR in bacterial expression system could be great useful technique, in case that the function of receptor was not affected by its post-translational modification, like olfactory receptor, bitter taste receptor and dopamine receptor [8].

Among the many reconstitution techniques, such as detergent micelles, liposomes, nanodiscs (NDs) and lipid cubic phases, NDs are considered the most appropriate tool for GPCR reconstitution for various applications [4,13,14]. NDs consist of a receptor, lipid bilayer, and membrane scaffold protein (MSP) [15]. The lipid bilayer provides the receptor with a well-organized biomimetic environment and the MSP wraps around the hydrophobic edge of the lipid, which can stabilize the receptor in an aqueous environment as well as a dried condition [16].

Recently, the bioelectronic sensors based on nanomaterials have been developed to monitor the receptor/ligand binding in real time. Above all, the high-quality receptor-based biosensor could provide a great advantage in terms of being able to mimic the human sensory system. In addition, it is expected to have outstanding sensitivity and selectivity as well as stability and reusability. The high-performance GPCR-based sensor can be used for various sensing applications, such as diagnostic, therapeutic and drug-interaction researches, assessment of food quality and fragrance development [17,10,18,19].

In this research, functional reconstitution of GPCRs produced from *E. coli* and its applications to the high-performance biosensor were developed. The GPCRs were overexpressed in *Escherichia coli* (*E. coli)*, solubilized with sodium dodecyl sulfate

(SDS), purified with affinity chromatography and functionally reconstituted with detergent micelles and NDs. They were obtained with high-purity and stability, which have a native-like structure. Their characteristics were confirmed by circular dichroism (CD) analysis, tryptophan fluosescence measurement, scanning electron microscopy and dynamic light scattering (DLS). Also, the dose-dependent and selective binding of reconstituted receptor was compared with receptor-transfected cells. Moreover, the highly purified and well-reconstituted GPCRs were applied to field-effect transistor (FET) to develop the protein-based biosensor, which is used to analyze the receptor agonism and antagonism, detect the death-associated odor cadaverine (CV) and smell a rose scent with human-like performance.

This study can be used an advanced method for purification and functional reconstitution of GPCRs produced in *E. coli*. Especially, the NDs embedded with GPCR produced in *E. coli* have a native-like binding pocket, which leads it to mimic the response of a natural receptor. This work represents significant progress in nano-bio technology toward a practical bioelectronic sensor. Furthermore, this could offer the receptor-based approaches including, quality control of food, basic research on GPCR, drug discovery and disease diagnosis.

Chapter 2

Literature review

2.1 Expression and purification of G protein-coupled receptor

2.1.1 Expression of GPCR

The GPCRs form a major family of membrane proteins in human cells including about 1000 representatives. As biological sensors, they provide signal transduction and cell response to various extracellular stimuli, from inorganic ions to proteins [20]. The common structural features of these proteins include seven hydrophobic transmembrane segments, extracellular N-terminus, and intracellular C-terminus. The binding sites of small organic molecules are often located within the transmembrane segments, while peptide hormones and proteins interact with the N-terminus of the GPCR and extracellular loops [21]. Proteins of the GPCR family are associated with various human diseases and are targets for many drugs. Development of new generation drugs possessing higher specificity and lacking side effects requires detailed study of mechanisms of ligand binding and signal transduction by these proteins, which can be ensured only by exact information about their spatial structure [22].

For this reason, the molecular modeling of receptors of the GPCR family have been researched based on the spatial structure obtained by X-ray crystallographic analysis [23,24]; however, they still remain as a challenges due to difficulties in obtaining protein preparations such as low concentration of the receptors in tissues, instability, and heterogeneity. Construction of systems for heterologous expression and stabilization of GPCR molecules by protein engineering methods has enabled establishment of three dimensional structure of GPCRs [25]. However, for crystallization of each of these receptors, specific methods including individual selection of the expression system and modification of the protein molecule were

used [24].

The most important part of this approach is selection of the optimal system for expression of the GPCR gene. Mammalian and insect cells provide the most suitable medium for synthesis and post translational processing of eukaryotic receptors, but their cultivation is quite expensive [26]. In yeast cells, hyperglycosylation of recombinant proteins is often observed, and folding of the GPCR is often incorrect [27]. Expression of foreign genes in bacteria, first of all, in *E. coli*, is not followed by any post translational modifications of the recombinant proteins and can provide enough material for study of the structure by NMR spectroscopy and X-ray analysis [28]. Cultivation of bacteria does not require costly media and the equipment and is easily scaled. Thus, *E. coli* cells provide a promising system for heterologous expression of GPCR genes.

2.1.2 Purification of GPCR

The GPCRs have seven transmembrane domains, which lead to hydrophobic structures. They were produced in the cell membranes or as a inclusion body especially in *E. coli* [29]. Thus, they should be solubilized and purified for protein-based researches. To solubilize the GPCR effectively, appropriate detergents or chaotropic agents are required. For solubilization of GPCRs, various detergents and chaotropic agents have been studied. The triton X-100 was reported that it can effectively solubilize the impurities in the solution containing target proteins, but they could not solubilize the GPCRs [30]. Sarcosyl, a strong ionic detergent, was found to allow efficient solubilization; however, it was difficult to remove the detergent for the subsequent reconstitution of hOR [8]. The anionic detergent SDS was reported that it can effectively denature the GPCRs, and can be easily remove with Bio-Bead or ß-cyclodextrin for the reconstitution of target receptors [7]. After

solubilization of proteins, the solubilized receptors should be purified with proper hydrophobic condition, because they tend to be easily aggregated because of their hydrophobicity [6]. They can be purified using affinity chromatography and size-exclusion chromatography and their purity could be much higher than purified soluble protein, because they are insoluble fraction, which is already separated from soluble fraction [7].

2.2 Functional reconstitution of G protein-coupled receptor

Regardless of the choice of expression system, three steps need be carried out to reconstitute GPCRs. The first step is to solubilize the plasma membranes of the expressing cells, typically with the help of detergents [31,32]. Afterward, affinity purification can separate the target GPCR from all other membrane components of the expressing cells. Finally, detergent is removed by dialysis, gel filtration, or adsorption [33,34]. And then, the GPCR should be reconstituted and is available for quantitative biophysical investigations.

2.2.1 Detergent micelles

The most basic strategy for in vitro studies of purified GPCRs is the use of detergent micelles (**Figure 2.1**). The detergent micelles are prepared from a mixture of detergents. Since the protein contains both hydrophobic and hydrophilic regions, amphipathic molecules such as detergents provide an environment that lends some stability to the GPCR molecules and prevents their precipitation. A variety of detergents is available for studies of transmembrane proteins, but the choice must fall on a detergent that is gentle enough to avoid immediate denaturation of the protein. For example, SDS, a very common but highly denaturing detergent, is not suitable for this reason. Detergents such as cholate,

dodecyl-β-D-maltoside (DDM), and n-octyl-β-D-glucopyranoside (OG) have been used with great success [17,35,7]. In spite of these successes, it is clear that a true lipid bilayer environment is best suited for biophysical studies of GPCRs in a functional and stable form. For instance, the photochemical properties of rhodopsin are sensitive to the composition of its lipid environment [36]. Indeed, a crystal structure of bovine rhodopsin retains tightly bound phospholipid molecules [37]. This tight binding suggests an important role for these molecules in maintaining the proper structure of the receptor. Moreover, reconstitution in micelles poses a fundamental challenge to functional studies of GPCRs due to the limited accessibility of the protein in the resulting system. Even if detergent were optimized such that a given receptor could be successfully kept in solution, the micelle is a highly disordered environment compared to the native membrane. Concentration of free detergent in solution is high because total detergent concentration must exceed the critical micelle concentration (CMC) at all times. The presence of high concentrations of detergent in solution may interfere with normal ligand and G-protein binding. Hydrophobic regions within the ligand-binding or G-protein-binding domain could also be destabilized or denatured by detergent. The micelle system is also unsuitable for investigating the oligomerization of GPCRs, which is thought to be critical to many of their normal functions [38,39]. This is because the bound detergent around the protein interferes with protein–protein contacts. Finally, the presence of detergents at high concentration freely diffusing in solution may lead to high background in optical measurements or NMR [4]. All of these drawbacks make a more faithful mimic of the native membrane environment highly desirable.

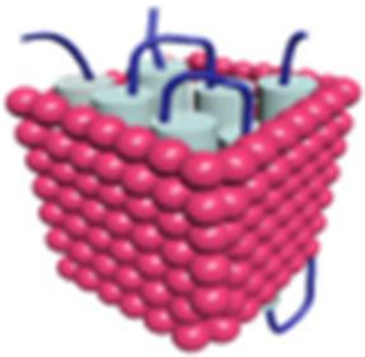

Figure 2.1 Structure of detergent micelle. The GPCRs is reconstituted with detergent.

2.2.2 Lipid vesicles

Reconstitution into lipid vesicle is the one of the most widely used methods for reconstituting membrane proteins into lipids. Lipid veisicles contain a single bilayer consisting of phospholipids that assemble spontaneously into a vesicle (**Figure 2.2**). They are usually formed by the hydration of dried lipids, which results in the formation of large multilamellar vesicles separated by a water layer. By adjusting the lipidic mixes and ratios, the nature and size of liposomes can be manipulated [40]. The size of lipid vesicles can also be tuned by subsequent procedures such as swelling, extrusion, emulsion, sonication, freeze-thaw cycles and so on [41,42]. Sonication usually results in small unilamellar vesicles (diameter 15–50 nm), whereas extrusion results mostly in large unilamellar vesicles (diameter>100 nm). During lipid vesicle self-assembly, a small amount of water is generally encapsulated and separated from the extraliposome solution. This has many advantages in terms of membrane transporter function, as proteoliposomes with reconstituted transporters can be tested functionally by their ability to selectively concentrate substrate within lipid vesicles. Similarly, if the proteoliposomes are formed in the presence of a substrate and washed, transport to the buffer can also be assessed [43]. Despite these advantages, the enclosed topology of vesicles can present a challenge. Only membrane-permeable molecules can interact with both the extracellular and the intracellular surfaces of the receptor. For biochemical and biophysical studies of ligand or effector binding and conformational dynamics of the receptor, it would be optimal to be able to probe all of the receptor's surfaces while retaining the ability to use bulk biophysical and structural techniques [44].

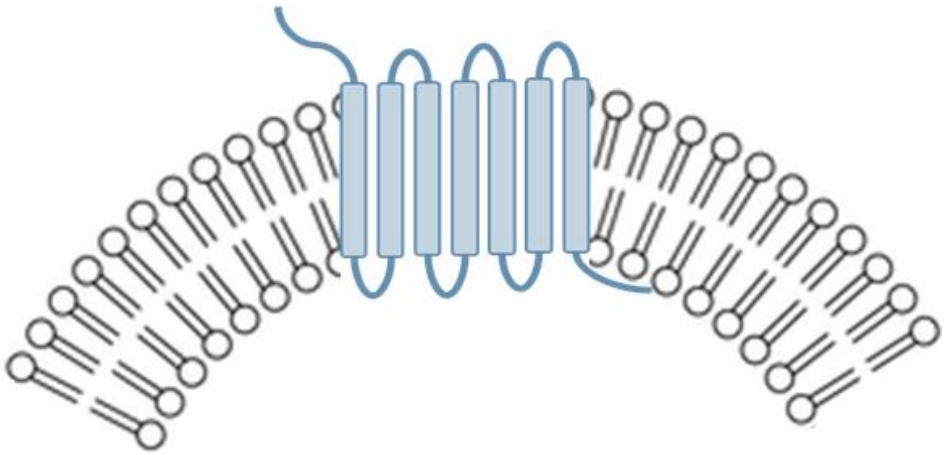

Figure 2.2 Structure of lipid vesicle. The receptor was reconstituted into lipid vesicle.

2.2.3 Bicelles

Bicelles can be formed by mixing membranes with a short chain lipid (or detergent) and a long chain lipid [45]. The long chain phospholipid forms the membrane protein-containing bilayer, which is then stabilized by the short amphiphilic chain positioning at the rim of the bilayer [46]. In the case of a GPCR solubilized in a mixed lipid/detergent micelle environment containing both long- and short-chain lipids, removal of detergent triggers formation of bicelles. Bicelles are fragments of lipid bilayer whose perimeter is stabilized by short-chain lipids or detergent molecules (**Figure 2.3**) [47]. Depending on the ratio of long- to short-chain components, bicelles have diameters of 10–30 nm, and up to 80 nm, enabling reconstitution of multiple GPCRs [48]. The diameter of a GPCR transmembrane core is ~3 nm. This means that the bicelles can accommodate multiple GPCR molecules. However, the number is limited, because the concentration of GPCRs is too low during the reconstitution procedure to make such a high density in a bicelle. Also, many GPCRs have intra- or extra-cellular domains whose diameters exceed that of the seven transmembrane core. The bicelle is a versatile system for GPCR reconstitution due to the wide range of lipid compositions it can accommodate [49]. Since it allows drastically reduced free detergent concentrations compared to micelles, this strategy minimizes detergent-induced background [78]. However, this system suffers from some of the drawbacks of micelles. Just as a concentration in excess of the CMC is needed to maintain micelles in solution, the long- and short-chain components of the bicelle structure need to be maintained above a critical concentration at all times. For GPCRs, which are often found in low abundance, this requirement can mean a large number of empty bicelles in the resulting solution, with the same consequences of high background and altered

effective concentrations of protein or lipid interacting partners as noted above for micelles. Moreover, the bicelle components need to be maintained at a specific ratio at all times in order for bicelles to persist. Thus, addition of a sample of a detergent-solubilized protein interacting partner may alter the ratio and destabilize the bicelles. The use of NDs in place of bicelles can overcome many of these drawbacks.

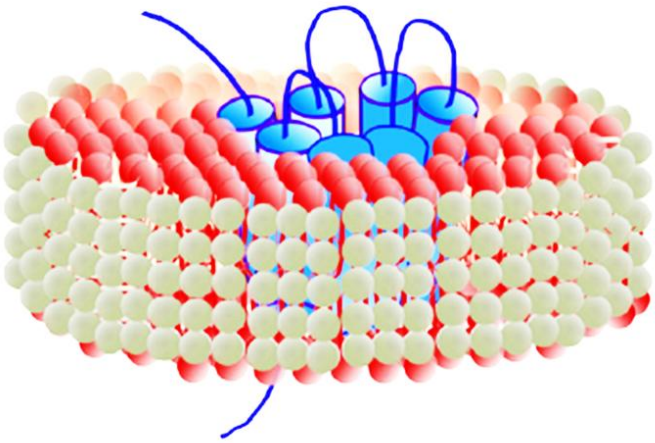

Figure 2.3 Structure of bicelles. The GPCRs is reconstituted in bicelles.

2.2.4 Nanodiscs

Among the many reconstitution techniques, such as detergent micelles, liposomes, nanodiscs (NDs) and lipid cubic phases, NDs are considered the most appropriate tool for GPCR reconstitution for various applications [4,13,14]. They resemble bicelles but provide a much more stable, well-defined membrane environment. NDs consist of a receptor, lipid bilayer, and MSP (**Figure 2.4**) [15]. The lipid bilayer provides the receptor with a well-organized biomimetic environment and the MSP wraps around the hydrophobic edge of the lipid, which can stabilize the receptor in an aqueous environment as well as a dried condition [16].

Reconstitution of GPCRs into NDs offers several advantages. The use of NDs does not lead to high concentrations of freely diffusing lipids or detergent molecules, and the ND structure is compact. These features permit relatively high concentrations of protein per volume, enabling bulk spectroscopic measurements [44]. Furthermore, the presence of MSP permits additional labeling for spectroscopic analysis. MSP can be expressed in *E. coli*, a system that allows genetic incorporation of a variety of unnatural amino acids, including fluorescent ones, by stop-codon suppression [50]. This provides a well-defined handle, for instance, for experiments using Forster resonance energy transfer or fluorescence correlation spectroscopy down to the single particle level. In such experiments, conformational dynamics can be studied in the close-to-native environment of the planar lipid bilayer core [16]. In addition, due to their stability and monodispersity, NDs represent a promising tool for structure determination of GPCRs. They may also become useful for crystallography, although crystallization may be challenging due to the rotational degree of freedom within the disc [13]. Moreover, unlike vesicles, NDs do not have an enclosed topology, so both the extracellular and

intracellular sides of the receptor are easily accessible. This property makes them very useful for reconstitution of GPCR-activated signaling cascades [4].

Furthermore, they can be effectively used to bioelectronic sensor. The size of NDs embedded with GPCRs (10-20 nm) is suitable for nanomaterial-based FET platform, which lead to effective signal transfer [14]. The ND-based bioelectronic sensor has advantages in terms of reliability and reproducibility as well as sensitivity and selectivity. Moreover, this lead to the development of highly stable biosensors, which can be utilized for practical applications.

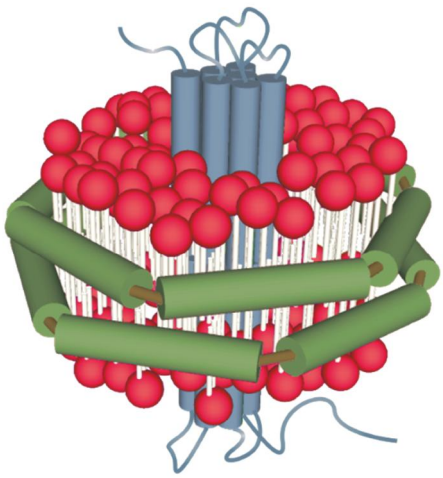

Figure 2.4 Structure of receptor-embedded NDs.

2.3 G protein-coupled receptor-conjugated biosensor based on field effect transistor

A biosensor is comprised of a biological sensing element, which acts as the primary transducer, and nanomaterial-based platform, such as carbon nanotube, conducting polymer and graphene, which plays role in the signal conversion unit (**Figure 2.5**) [51]. This sensor can detect a target molecules using biological binding affinity, and many different biomolecules can be used as sensing elements, such as DNA, aptamers, antibodies, peptides, proteins and so on [52,2].

The role of the two components in the biosensors is to detect the signal from the change of reaction and produce signals as a electrical, thermal, or optical signals, which can be converted digitally for further processing [53]. These properties are important for the high-performance sensor in its selectivity and sensitivity [54]. The sensitivity, which reflects the detection capability of the biosensor, is the magnitude of the sensor signal change in response to the change in analyte concentration [55]. The selectivity of a biosensor depends upon the choice of biological sensing element [56]. Thus, this selectivity can be modified when nanomaterial-based sensors are associated with diverse biological recognition elements [57]. Various nanomaterial-based platforms can be used as secondary transducers for efficient transport of electrons [58]. Especially, FET platforms have been widely used for high-performance biosensors [41,59,60]. This FET-based biosensor has several important features for the detection of chemical or biological species [46]. The nanomaterial, serves as the conducting channel between the source and drain electrodes. And the nanomaterials are typically located on the surface of the supporting substrate and are in direct contact with the biomolecule which can detect a target analyte [61]. The principle of detection involves charge transfer from biological interaction to the nanomaterial. If a charge transfer occurs,

the threshold voltage or current will become either more positive or more negative [62,63]. These important characteristics lead to a FET device's configuration that is extremely sensitive to minute variations in the surrounding environment [62].

Recently, Nano-electronic sensors as FETs integrated with biological receptors have been developed to detect the specific targets, which leads to the bioelectronic sensors [10,61,64]. Moreover, the device containing stable and qualitative biomolecules, especially GPCRs, precisely and rapidly binding to their specific target can be powerful tool for a development of a practical biosensor [64]. However, the development of stable bioelectric sensor with high-quality GPCRs, which allows reproducible and rapid responses, remains challenging.

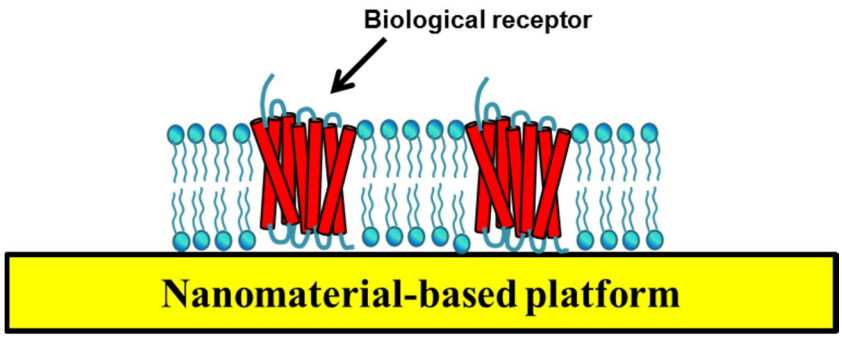

Figure 2.5 A biosensor comprised of a biological sensing element and nanomaterial-based platform.

Chapter 3

Experimental procedures

3.1 Materials

Pyrrole-2-carboxylic acid (P3CA, 99%), 1-pyrenecarboxylic acid (PCA, 97%), FeCl3 (97%), (3-aminopropyl)trimethoxysilane (97%), 4-(4,6-dimethoxy-1,3,5-triazin-2-yl)-4-methylmorpholinium chloride (DMT-MM, > 96%) were purchased from Sigma-Aldrich (USA). Zebrafish (Danio rerio) cDNA was donated by Prof. Hyunsook Lee (Seoul National University). Palmitoyloleoylphosphatidyl-choline (POPC) and palmitoyloleoylphosphatidylglycerol (POPG) were purchased from Avanti Polar Lipids (USA). Sodium cholate and HEPES were purchased from Sigma-Aldrich (USA). A pMSP1E3D1 bacterial expression vector was purchased from Addgene (USA), respectively. Semiconducting 99% single-walled carbon nanotubes (ssCNTs) were purchased from NanoIntegris, Inc. (USA) and used as received in our experiments. Geraniol, R-(+)-citronellol, benzyl salicylate, 1-phenylethanol, linalool, α-damascone, geranyl chloride, geranyl formate, 1,7-octadiene, 3,7-dimethyl-1-octanol, amyl butyrate, trimethylamine, and other chemical reagents used in our experiments were purchased from Sigma-Aldrich (USA). The natural rose oil (Damask rose) was provided by the team manager of LG Household & Health Care (Korea), Hoodeok Kim. Poly(vinyl alcohol) (PVA, M_w 9000), $FeCl_3$ (97%), dodecyltrimethylammonium bromide (DTAB, ≥98%), pyrrole (98%), and $NaBH_4$ (≥98%) were purchased from Sigma-Aldrich (USA). Hydrazine monohydrate ($N_2H_4 \cdot H_2O$, 98%), ammonium persulfate (APS, 98%) and pyrrole-3-corboxylic acid were purchased from Sigma-Aldrich and Acros Organics (USA). Nickel (Ⅱ) chloride (99%) was acquired from JUNSEI USA).

3.2 Gene cloning

The DRD1 gene (GenBank No. NC000005.9) was amplified by PCR with primers

(5' CAC CAG GAG ATA TAC AAT GAG GAC TCT GAA CAC 3′, 5′ GGT TGG GTG CTG ACC GTT TTG TGT GAT 3′) using pcDNA3.1 containing DRD1 cDNA. The PCR product was cloned into the pET-DEST42 expression vector (Invitrogen) using an entry vector (Invitrogen) and LR clonase (Invitrogen). The ApoA-I gene was designed so that it contained 6xHis and stop codon gene, and it was amplified by PCR with primers (5' CAC CAG GAG ATA TAC ATA TGA AAG CTG CGG TGC TGA CC 3', 5' CTA GTG GTG GTG GTG GTG GTG CTG GGT GTT GAG CTT CTT AGT GTA 3') using human genomic DNA. The TAAR13c gene was amplified by PCR with primers (5' CAC CAG GAG ATA TAC ATA TGA TGC CCT TTT GCC ACA AT 3', 5' TGA ACT CAA TTC CAA AAA TAA TTT ACA C 3') using the zebrafish cDNA. Amplified PCR products were inserted into the pET-DEST42 bacterial expression vector (Invitrogen, USA) using a gateway cloning system (Invitrogen, USA). The TAAR13c gene was also cloned into pcDNA3 mammalian expression vector using an amplified PCR product (primer; 5' ATG AAT TCA TGG ATT TAT CAT CAC AAG AAT 3', 5' ATC TCG AGT CAA ACC GTA AAT AAA TTG ATA 3'). The hOR1A2 genes were amplified by polymerase chain reaction (PCR) using human genomic DNA. The PCR products were cloned into a pcDNA3 mammalian expression vector and pET-DEST42 bacterial expression vector using enzyme methods and a gateway cloning system (Invitrogen, USA).

3.3 Expression

3.3.1 Expression of GPCRs in *E. coli*

The BL21 (DE3) cells were transformed with the pET-DEST42/GPCR vector and cultured in LB medium (+50 μg/mL ampicillin) at 37 °C until the OD_{600} value

reached 0.5. The expression of GPCR was induced by the addition of 1 mM IPTG, and the cells were incubated for 4 h. The cells were centrifuged (7000 g, 20 min, 4 °C), and pellets were resuspended in PBS containing 2 mM EDTA. The cells were disrupted by sonication (5 s on/off, 5 min) and centrifuged (12000 g, 4 °C, 20 min). The sonication and centrifugation were repeated, and the pellet of the sample was collected. The collected pellet was analyzed by SDS-PAGE and western blot analysis.

3.3.2 Expression of membrane scaffold protein in *E. coli*

BL21(DE3) *E. coli* cells bearing the pET-DEST42/ApoA-I construct or pMSP1E3D1 were cultured in 1 L Luria-Bertani (LB) medium (+50 μg/mL ampicillin) at 37 °C. When the cells were grown until the OD_{600} value reached 0.5, the overexpression of ApoA-I and MSP1E3D1 were induced by the addition of isopropyl thiogalactoside (IPTG) to a final concentration of 1 mM. After 3 h, the cells were centrifuged (7000 g, 20 min, 4 °C), resuspended in a lysis buffer (20 mM Tris-HCl, 0.5 M NaCl, 20 mM imidazole, pH 8.0) and disrupted by sonication (5 s on/off, 5 min). The cell lysate was centrifuged at 12,000 g for 30 min at 4 °C. The ApoA-I in the supernatant was collected

3.3.3 Expression of GPCR in HEK-293 cell

Human embryonic kidney (HEK)-293 cells were cultured in Dulbecco's Modified Eagles Medium (DMEM) (HyClone, USA) supplemented with 1 % penicillin, 1% streptomycin (Gibco, USA) and 10% Fetal Bovine Serum (FBS) (Gibco, USA) at 37 °C under 5% CO_2. The transfection was performed with Lipofectamine3000 (Invitrogen, USA) following the manufacturer's protocol. The cells were transfected with Liopofectamine3000 DNA mixture containing GPCR, pCRE-Luc,

pSV40-RL, $G_{\alpha olf}$ and RTP1S. The cells were harvested with phosphate-buffed saline, (PBS, pH 7.4) and then disrupted by sonication (2 s on/off, 2 min) (Sonics Vibracell, USA).

3.3.4 Western blot and total protein assay

All protein samples (20 μL) were analyzed by SDS-PAGE and western blot analysis. Western blot analysis was performed using anti-FLAG rabbit Ab (Cell Signaling Technology, USA), anti-His-probe mouse Ab (Santa Cruz Biotechnology, USA) and anti-V5 epitope mouse Ab (Santa Cruz Biotechnology, USA) as primary Ab. HRP-conjugated anti-rabbit Ab (Millipore, USA) and HRP-conjugated anti-mouse Ab (Milipore, USA) were used as a secondary Ab. Luminata Forte western HRP substrate (Millipore, USA) was also used. The protein concentration was measured using BCA assay kit (Pierce, USA).

3.4 Purification

3.4.1 Purification of GPCR

The collected fraction was solubilized in solubilization buffer (0.1 M Tris-HCl, 20 mM sodium dodecyl sulfate (SDS), 100 mM dithiothreitol (DTT), 1 mM EDTA, pH 8.0) at 25 °C. The solubilized proteins were dialyzed against 0.1 M sodium phosphate (pH 8.0) containing 10 mM SDS using a 10K MWCO dialysis cassette (Thermo Scientific, USA), filtered with a 0.2 μm bottle top filter (Thermo Scientific, USA), and then applied to HisTrap HP column equilibrated in 0.1 M sodium phosphate (pH 8.0) containing 10 mM SDS. The column was successively washed with gradient (pH 8.0 to 7.0) using washing buffer (0.1 M sodium phosphate, 10 mM SDS), and the TAAR13c was eluted with the same buffer at pH

6.0. The eluted protein was dialyzed against the HEPES buffer II (20 mM HEPES-NaOH, 100 mM NaCl, 25 mM cholate, 1mM EDTA, pH 8.0). The purified GPCR was analyzed by SDS-PAGE and western blot analysis.

3.4.2 Purification of membrane scaffold protein

After the production of ApoA-I or MSP1E3D1, the cells were harvested by a centrifugation at 7000g for 20 min at 4 °C. Then, they were resuspended in lysis buffer (20 mM Tris-HCl, 20 mM imidazole and 0.5 M NaCl, pH 8.0), and they were disrupted by brief sonication (5 s on/off, 5 min). The cell lysates were centrifuged at 12000g for 30 min at 4 °C. The protein was filtered by a 0.45 μm bottle top filter. Then, the protein was loaded to a HisTrap HP column (GE Healthcare, Sweden) using fast protein liquid chromatography (FPLC) (GE Healthcare). The column was successively washed with washing buffer (20 mM Tris-HCl, 50 mM imidazole and 0.5 M NaCl, pH 8.0). The target protein was collected with elution buffer (20 mM Tris-HCl, 400 mM imidazole and 0.5 M NaCl, pH 8.0). The purified ApoA-I or MSP1E3D1 was dialyzed against the HEPES buffer I using the HiTrap HP desalting column (GE Healthcare, USA) and stored at 4 °C until used. And the 6xHis-tag of purified MSP1E3D1 was removed using TEV protease.

3.5 Functional reconstitution

3.5.1 Reconstitution using detergent micelles

After dialysis of eluted proteins against 0.1 M Tris-HCl (pH 8.0), 10 mM SDS, and 0.5 mM EDTA, the sample was diluted with 0.1 M Tris-HCl (pH 8.0), 3 mM SDS, and 0.5 mM EDTA and mixed with 1 mM glutathione disulfide, 5 mM

glutathione, 6 mM *n*-dodecyl-β-D-maltopyranoside (DDM), 6 mM 6-cyclohexylhexyl-β-D-maltoside (Cymal 6), and 6 mM methyl-β-cyclodextrin. The sample was incubated at -20°C for 48–60 h, and then thawed at 4°C. After addition of 25 mM $CaCl_2$, the sample was incubated at 4°C overnight. The sample was dialyzed against 100 mM Tris-HCl (pH 7.4), 300 mM NaCl, 10% glycerol, 1 mM DDM, 1 mM Cymal 6, and 1 mM EDTA, and was maintained at 4°C. The reconstituted receptor was prepared at 250 μg/mL for all experiments.

3.5.2 Reconstitution using nanodiscs

Lipids (Palmitoyloleoylphosphatidylcholine (POPC), palmitoyloleoylphosphatidylglycerol (POPG)) were mixed in chloroform at the molar ratio of 1:1. Then, they were dried by nitrogen gas and put in a vacuum for 1h to remove residual chloroform. The lipids were solubilized with the HEPES buffer I, and they were added to the purified receptor. The lipid/receptor mixture was incubated on ice for 10 min, and successively mixed with MSP. The mixed solutions were incubated with a gentle stir for 2 h at 4 °C. The final mixture contained 1 μM receptor, 8 mM lipids, 25 mM detergents, and 100 μM MSP. Afterward, Bio-Beads (Bio-Rad, USA) were added to the mixture to adsorb detergents with agitation overnight. Finally, the mixture was loaded to size exclusion chromatography (SEC) (Superdex 200 Increase 10/300 GL, GE Healthcare, USA) to remove unbound units. The column was equilibrated with HEPES buffer II (20 mM HEPES-NaOH, 100 mM NaCl and 1mM EDTA, pH 8.0). The receptor-embedded NDs were collected and stored at 4 °C.

3.6 Characterization

3.6.1 Luciferase assay

The HEK-293 cells were cultured in Dulbecco's Modified Eagles Medium (DMEM) (HyClone, USA) supplemented with 10% Fetal Bovine Serum (FBS) (Gibco, USA), 1% streptomycin (Gibco, USA), and 1% penicillin at 37 °C under 5% CO_2. The cells were transfected with a DNA mixture containing OR, $G_{\alpha olf}$, RTP1S, pCRE-Luc, and pSV40-RL using a Lipofectamine 3000 (Invitrogen, USA) following a manufacturer's protocol. The Dual-Glo Luciferase Assay System (Promega, USA) was introduced to measure the responses of OR to various odorants. The HEK-293 cells expressing OR were stimulated with serum-free DMEM, and then incubated in solutions containing various odorants. The luminescence intensity was measured with a Spark 10M multimode microplate reader (TECAN, USA). The normalized luciferase activity was calculated using a formula [CRE/Renilla(N) – CRE/Renilla(0)]/[CRE/Renilla(FSK) – CRE/Renilla(0)]. In this measurement, 10 μM FSK and odorant-free DMEM solution were used as a positive and negative control, respectively.

3.6.2 Analyses of functional receptor

After the dilution of reconstituted receptor (250 μg/mL) with 300 mM NaCl, 100 mM Tris-HCl (pH 7.4), 1 mM DDM, 1 mM Cymal 6, 1 mM EDTA, and 10% glycerol, CD spectra were recorded between 190 and 260 nm using a Chirascan-plus CD spectrometer (Applied Photophysics). The sizes of NDs were analyzed using a dynamic light scattering spectrophotometer (DLS) (DLS-7000, Japan). The NDs was also confirmed by using a SUPRA 55VP field-emission scanning electron microscope (FE-SEM) (Carl Zeiss, Germany). The intrinsic fluorescence of NDs was measured in real-time using a LS 55 luminescence spectrometer (Perkin Elmer, USA) (excitation 290 nm; emission 340 nm). The real-time intrinsic fluorescence of receptor was measured using 1-10 mM of various amines.

3.7 Fabrication and immobilization

3.7.1 Dopamine receptor-conjugated cPPy-coated CNT-FET

Pristine CNTs were pretreated by PCA in a water-ethanol (3:1) solution for 24 h. To remove the PCA residue D.W. surface-functionalized CNTs (0.2 g) were immersed into a $FeCl_3$ solution (0.02 g), as an initiator, and the CNTs were dried in the reactor. Under vacuum, a mixture (0.05 mL; pyrrole monomer and P3CA) was injected into the reactor for vapor deposition polymerization and then stored in an 80 ^{o}C oven. A conventional microelectromechanical system (MEMS) was used to design the interdigitated microelectrode array (IMA) on glass substrates. A positive photoresist (AZ5214, Clariant Corp.) was spin-coated onto a glass wafer and exposed to ultraviolet (UV) with a high-resolution film mask, followed by image reversal and development. To deposit Cr/Au (10 nm / 100 nm, respectively) on the wafer, a thermal evaporator was used and a lift-off process was performed. The IMAs were modified by 10 wt% (3-aminopropyl)trimethoxysilane overnight, which resulted in the amine functional groups. The amine groups were reacted with the carboxylic groups of the surface of the nanohybrids using 1 wt% aqueous DMT-MM as a condensing reagent for 12 h. Then, the same reaction was carried out with DRD1 and nanohybrids by DMT-MM for 6 h, leading to the strong covalent bonding (-CONH-) between the DRD1 and nanohybrids.

3.7.2 Nanodisc-based CNT-FET with floating electrode

For ssCNTs dispersion, ssCNTs were dispersed in 1,2-dichlorobenzene using an ultrasonic cleaner for 5 h to the final concentration of 0.05 mg/mL. For the assembly of ssCNTs, an octadecyltrichlorosilane self-assembled monolayer with nonpolar terminal groups was formed on a SiO_2 substrate (3000 Å) via

photolithography. For the selective adsorption of ssCNTs, the substrate was immersed into the ssCNTs solution for 20 s and washed with 1,2-dichlorobenzene. Afterward, source, drain, and five floating electrodes were fabricated using photolithography and thermal evaporation (Pd/Au 10 nm/15 nm). Each floating electrode has the dimensions of 200 μm width and 10 μm length. The CNT network channel has the dimensions of 3 μm width and 170 μm length. Lastly, a passivation layer (Photoresist, DNR) was formed using photolithography to prevent leakage currents during sensing measurement in aqueous environments. N-acetyl-L-cysteine powder was dissolved in distilled water to the final concentration of 0.5 M. A cysteine monolayer was formed on the gold floating electrodes of CNT-FETs by incubation in the N-acetyl-L-cysteine solution for 10 min at 37 ^{o}C. Then, the CNT-FETs were washed with distilled water. Subsequently, the CNT-FETs with floating electrodes were immersed in a solution containing half-V5 Ab fragments. 2-Mercaptoethylamine hydrochloride (2-MEA) which is a reducing agent was used to divide the V5 Ab into two half-V5 Ab fragments. After the incubation for 1 h at 37 ^{o}C, the CNT-FETs were washed with PBS buffer. The half-V5 Ab fragments were selectively adsorbed onto the gold floating electrodes of the CNT-FETs via their thiol groups. Lastly, the immobilization of hOR1A2NDs on the floating electrodes was carried out by incubation in a solution containing hOR1A2NDs for 1h at room temperature. As a result, the hOR1A2NDs were immobilized on the gold floating electrodes using half-V5 Ab fragments and thiol groups as a linker.

3.7.3 Nanodisc-conjugated Ni-decorated cPPyNP in FET

Uniform sized cPPy nanoparticles (cPPyNP) with 100 nm diameter were prepared with PVA, $FeCl_3$, and the mixture of pyrrole and pyrrole-3-carboxylic acid monomers in previous work [65]. The prepared cPPy nanoparticles were dissolved

in 60ml distilled water at 0.05 wt% and 0.1 g of hydrazine monohydrate was injected. 0.01 g of $NaBH_4$ powder and 1.5 ml of 1 wt% $NiCl_2$ aqueous solution were simultaneously added to mixed solution and the solution was stirred with 450 rpm for 3 h at room temperature. Same process was repeated once. Then, the solution was centrifuged with water and acetone several times to eliminate impurities. The solution was dried for 12 h at 60 °C to form Ni/cPPyNP powder. To construct FET sensor, IDA, composed of pairs of 25 lines of gold fingers on the glass plate, was used as immobilization substrate of Ni/cPPyNPs. IDA electrode was treated with 5 wt% amino-silane (3-aminopropyltrimethoxysilane, APS) aqueous solution for 12 h to adopt amino groups to the electrode surface. Then, the treated electrode was exposed to 0.2 wt% Ni/cPPyNP aqueous solution (150 μL) and 1 wt% 4-(4,6-dimethoxy-1,3,5-2-yl)-4-methylmorpholinium chloride (DMT-MM) aqueous solution (150 μL) for a day. Finally, the Ni/cPPyNPs immobilized electrode was rinsed with distilled water and exposed to receptor solution, ND or micelle shaped, for 2h at room temperature.

3.8 Electrical measurement

3.8.1 Preparation of tested samples

The DRD1 agonists and antagonists were purchased from Tocris. DA, epinephrine and serotonin were purchased from Sigma-Aldrich. All the DRD1 agonists and antagonists were solubilized in DMSO, and diluted in PBS. The sample solutions were freshly prepared immediately before the experiment.

All the tested amines were prepared at 1 mM in 100% DMSO, and serially diluted 1:10 with HEPES buffer. Fresh foods (salmon (Norway), beef (Korea), pork fat (Korea)) were purchased from a local grocery store. Each food sample

(100 mg) was soaked in HEPES buffer solution (1mL) and incubated at 37 °C for 4 weeks to prepare the real samples. The spoiled foods samples were collected weekly (0 - 4 weeks) and kept in microtubes at -80 °C. The frozen samples were thawed at once just before the electrical measurements. The sample solutions were diluted to 1/1000 and filtered by 100,000 nominal molecular weight cut-off (NMWCO) ultrafiltration membranes (Ultracel YM-100, Millipore, USA) with centrifugation at 1000g for 10 min to remove floating matter in the sample solutions.

The Geraniol, R-(+)-citronellol, benzyl salicylate, 1-phenylethanol, linalool, α-damascone, geranyl chloride, geranyl formate, 1,7-octadiene, 3,7-dimethyl-1-octanol, amyl butyrate, trimethylamine, and other chemical reagents used in our experiments were dissolved in the HEPES buffer II solution. A volume of 50 μL of the natural rose oil stock solution was mixed with 4.95 mL of the HEPES buffer II solution (1% v/v). The mixed rose oil solution was filtered through a 0.45-μm-pore-size syringe filter (Advantec, Dublin, CA). Then, the rose oil solution was additionally diluted with HEPES buffer II solution to prepare rose oil solutions diluted from $1/10^{11}$ to $1/10^{5}$.

3.8.2 Signal measurement

A Keithley 2612A sourceMeter was used to obtain the electrical signal that was converted to a real-time response between the target molecules (DA, agonists, and antagonists) and the DRD1-conjugated nanohybrid transistors. The current level was normalized by the equation $\Delta I / I_0 = (I - I_0) / I_0$, where I_0 and I indicate the initial and measured real-time currents, respectively.

For the detection of the responses of a bioelectronic nose, a CNT-FET functionalized with NDs was connected to the Keithley 4200 semiconductor

analyzer. A 9 μL droplet of the HEPES buffer II was placed on the channel region of the device. The source-drain bias voltage of 0.1 V was applied during electrical measurement. Source-drain currents were monitored upon the addition of 1 μL various odorants solutions and reagents.

All electrical measurements for chapter 6 were measured using Keithley 2612A source meter and probe station (MS TECH, Model 4000) in pH 7.4 of PBS solution. To utilize the solution-based measurement, a glass bath was designed and used. The change in the current was as follows

$$\left[\frac{\Delta I}{I_0}\right]_{SD}(\%) = \frac{(I - I_0)}{I_0} \times 100$$

where I_0 represents the initial current and I is the real-time measured current.

The resistance changes of receptor attached Ni/cPPyNPs fixed IDA electrodes were monitored with a source-meter connected to a computer. The sensors were placed in a 350mL chamber, and then various CV gas concentrations were injected into the chamber by the N_2 bubbler. The resistance values were recorded in real time at a constant applied current of 10^{-9} A. After receptor attached Ni/cPPyNPs interacted with CV gas for several minutes, each vapor was replaced by compressed N_2 air to remove the CV molecules attached on the surface of the transducer nanomaterials. This process was performed repeatedly several times. The real-time resistance was monitored at a constant applied current of 10^{-9} A. The change in the resistance was as follows

$$\left[\frac{\Delta R}{R_0}\right](\%) = \frac{(R - R_0)}{R_0} \times 100$$

where R and R_0 are the real-time resistance and the initial resistance, respectively.

Chapter 4

Functional reconstitution of human dopamine receptor into micelle for the analysis of receptor agonism and antagonism

4.1 Introduction

GPCRs, which act as molecular switches within the cell, are found only in eukaryotes and are considered seven-domain receptors [66]. Their major role is to transfer external signals into the cell through a conformational change in response to ligand binding, thus, resulting in the production of hundreds of second messenger molecules. Through this consecutive protocol, GPCRs can promote functions throughout the entire human body from sensation to hormone responses [67,20]. Specifically, in pharmacology, the functions of GPCRs provide unique binding events between drug-target interactions. Therefore, many researchers have designed GPCR-response-behavioral screening of new drugs by measuring the receptor agonist-antagonist efficacy to determine whether the substrate fully or partially activates the receptors [68,69]. Although a few screening methodologies are based on GPCRs, including surface plasmon resonance, intrinsic fluorescence assays and in-vitro pharmacological assessment, they have critical limitations for real-time monitoring and competitive responses. In addition, many pharmacological methods only use cell-based signal transduction, rather than receptor-based transduction [70,71]. In the previous studies, a receptor-based FET, such as a bionanoelectronic nose and bioelectronic tongue, provided attractive advantages for real-time monitoring, rapid responses and highly sensitive and selective responses [8,4,72,5]. Moreover, the minimum detection level in the FETs was at the *ca*. pico- or femtomolar (10^{-12} - 10^{-15} M) level and their equilibrium constants can be characterized by their dose-dependent responses, which are suitable for comparing systems using agonists and antagonists.

The purification and functional reconstitution of GPCRs have been studied to acquire basic knowledge of the crystal structure, receptor-signaling and

pharmacological research. Moreover, many studies have suggested that the receptor with high-purity and good-reconstitution can be used as a powerful tool for qualitative and quantitative biophysical information on receptor/ligand binding details [73,74]. In addition, a high-quality receptor can be integrated into nanobio-technologies in various fields, such as clinical diagnosis, health control and drug discovery, leading to a high-performance human sensory system [75,76]. Although the importance of GPCR purification has been well demonstrated, GPCR purification methodology remains a challenge because of their strong hydrophobicity and complicated structures [77,78].

Dopamine (DA), which is an amine chemical synthesized from its precursor chemical L-3,4-dihydroxyphenylalanine in the brain and kidneys, performs highly important functions in the brain and the central nervous system as a neurotransmitter released by nerve cells and as a local chemical messenger that controls the immune system, digestive system, and others [79,80]. DA is critical for monitoring dysfunctions of the DA system in the human body to prevent several significant medical conditions, including Parkinson's disease, Alzheimer's disease, schizophrenia, depression, and addiction [81-83]. Specifically, in the development of new pharmaceuticals (*e.g.* anti-Parkinson's drugs), the principles underlying the functional potency of DA agonists and antagonists are preferentially studied using human dopamine receptors (DRs) [84,54]. However, those innovative analytical methodologies cannot provide real-time, rapid, highly sensitive and selective detection for studying DR agonism and antagonism. Therefore, research establishing the DR agonist-antagonist relationship should be continuously discussed.

In this chapter, advanced methodologies were demonstrated for analyzing the affinity between DR and DR agonists and –antagonists using a DR-modulated FET

assay. The DRD1 was successfully overexpressed in *E. coli*, purified using affinity column chromatography and then reconstituted using detergent micelles. To investigate the functional potency between DR and DA agonists and antagonists, the FET assay was designed based on previous works [85,51]. Specifically, an ultra-thin-layer (*ca*. 5 nm) of carboxylated polypyrrole (cPPy), which can block the signal noise caused by the physical adsorption of DA on carbon nanotubes CNTs, was coated onto the CNTs as a transducer for the FET system, and the CNTs were chemically combined with reconstituted DRD1 using a coupling reaction. The DRD1-conjugated nanohybrid FET assay was utilized to characterize DRD1 agonism-antagonism, leading to a simple, accurate methodology for new drug discovery.

4.2 Purification and functional reconstitution of DRD1

Overexpression of the GPCR in bacterial cell membranes is very difficult because their domains contain positive charges, and eukaryotic membrane proteins have a complicated insertion mechanism. However, previous reports demonstrated the possibility of a high level of expression of GPCRs in *E. coli* using specific vectors such as pDEST15, pDES17, and pET-DEST42 [7,30]. In this experiment, a fabrication process, which uses human receptors as bioprobes in a FET system enhancing the performance of the device, was previously developed [76,85]. **Figure 4.1a** shows the experimental results of the sodium-dodecyl-sulfate-polyacrylamide gel electrophoresis (SDS-PAGE) for purified DRD1 expressed in *E. coli*. The DRD1 overexpressed by the *lacO* gene was dissolved in a buffer solution containing SDS and was purified using Ni^{2+} column chromatography. DRD1 was found at 49 kDa with a clear band in the eluted fraction. The DRD1 purified using a His-probe antibody was analyzed by western

blot, as shown in **Figure 4.1b**. These results indicate that DRD1 was prepared with high purity.

Generally, purified DRD1 is formed in the denatured structure and must be reconstituted into its native form. Various GPCRs have also been successfully reconstituted in artificial membrane-like environments, and their efficient folding was demonstrated using detergent micelles that are hydrophobic at levels greater than their CMC. Moreover, proper detergent conditions could maintain the receptor in its native structure in the solution. Therefore, nonionic detergents, Cymal 6 and DDM, were used to form the detergent micelles in previous method [7,17], resulting in the preparation of the purified DRD1 using a biomimetic membrane environment. To evaluate the correct folding of the reconstituted proteins, the circular dichroism (CD) spectrum of the reconstituted DRD1 was recorded. **Figure 4.1c** displays the CD spectra of both the solubilized DRD1 and reconstituted DRD1. The figure indicates that the reconstituted receptor recovered its secondary structure. Although, the spectra, which were obtained from protein solubilized in the solution containing SDS, represented decreased ellipticity, the CD spectra of the reconstituted DRD1 demonstrated recovered ellipticity. Moreover, this result exhibited α-helical features (≈50%) corresponding to an α-helical content, as did the CD spectra of other functional GPCRs. Natural GPCRs have been reported to contain more α-helical elements [20,7].

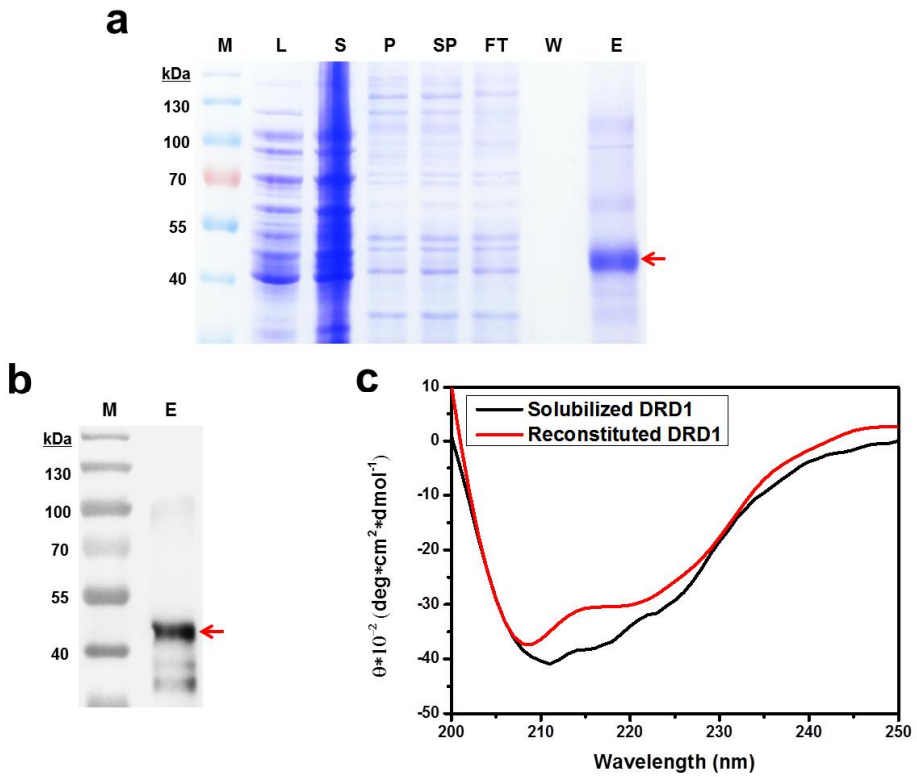

Figure 4.1 Purification and functional reconstitution of DRD1. (a) SDS-PAGE analysis of DRD1. M, Molecular weight marker; L, Cell lysate; S. Supernatant of the cell lysate; P, Pellet of the cell lysate; SP, Solubilized P after solubilization; FT, Flow-through after Ni^{2+} column purification. (b) Western blot of the purified DRD1 using an anti-His-probe antibody. The arrows indicate the size of the purified DRD1. (c) CD spectra of DRD1 (black line, solubilized and purified; red line, reconstituted).

4.3 Chemical immobilization of DRD1 on nanohybrids

Reconstituted DRD1 was attached to the surface of the cPPy-CNT hybrid structure. The nanohybrids were prepared using a chemical vapor deposition process reported in a previous work [86], to remove the background noise response caused by the physical interaction between DA and bare CNTs in the FET system (**Figure 4.2**). **Figure 4.3a** schematically shows the fabrication process of the DRD1-immobilized nanohybrid. An ultrathin cPPy layer was uniformly coated on the CNT surface and the amine groups of the DRD1 were chemically reacted with the carboxylic groups of cPPy using the coupling reagent, 4-(4,6-dimethoxy-1,3,5-triazin-2-yl)-4-methylmorpholinium chloride (DMT-MM), resulting in covalent amide bonding (**Figure 4.4**) [51]. To characterize the surface of the nanohybrid, high-resolution transmission electron microscopy (HR-TEM) was used (**Figure 4.3b and c**). HR-TEM images show the bare CNT with a *ca*. 30 nm diameter (**Figure 4.3b**) and the ultra-thin cPPy layer is clearly observed with a thickness of *ca*. 5 nm (**Figure 4.3c**). The immobilization of DRD1 on the nanohybrid surface was also confirmed using field-emission scanning electron microscopy (FE-SEM). **Figure 4.3d** and **e** show typical FE-SEM images of the nanohybrid before and after the introduction of DRD1, respectively. The DRD1-nanohybrids exhibited a considerably more rugged surface due to the attached reconstituted DRD1. The ultra-thin cPPy layer plays several critical roles in the construction of DA FET biosensors. Namely, it i) blocks the nonspecific binding of DA on the surface of the bare CNT through a π- π interaction, ii) provides efficient charge transfer in the liquid state, iii) provides significantly better stability in the biosensing system than the noncovalent approach, and finally, iv) enables controlling various chemical

functionalities without structural surface defects [9,73]. Therefore, the nanohybrids were introduced as a transducer in a liquid-ion gated FET system.

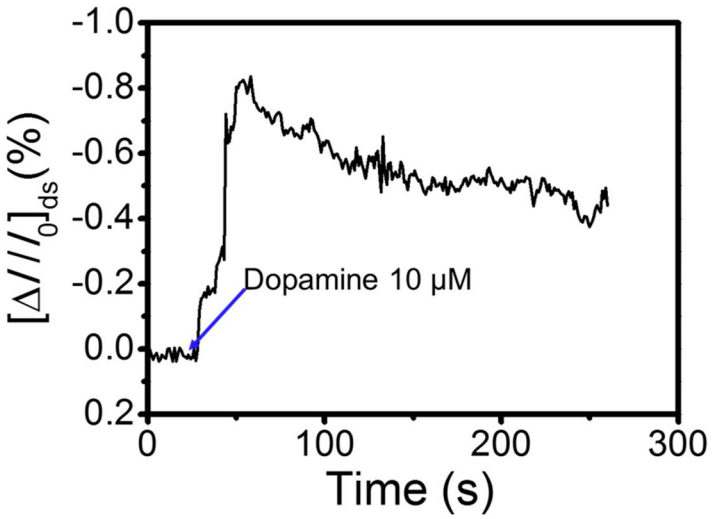

Figure 4.2 Real-time response using bare CNT FET assay.

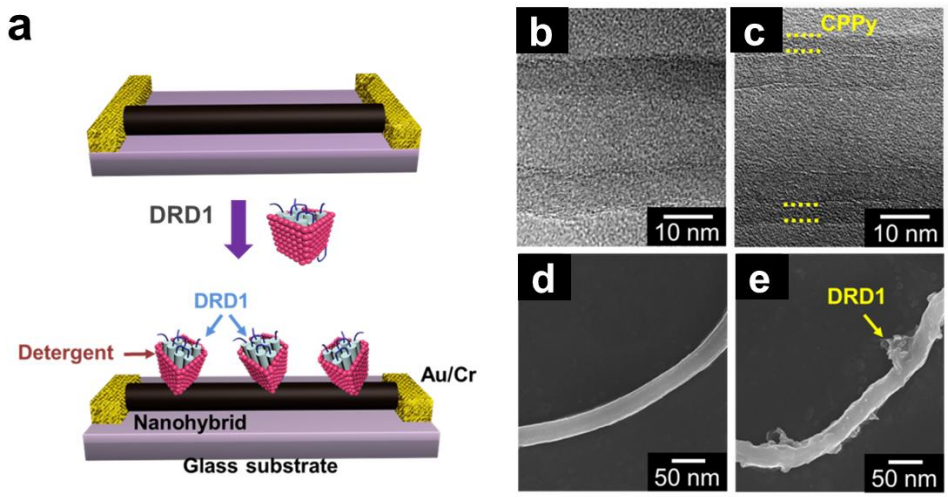

Figure 4.3 (a) Schematic illustration of the process of immobilizing DRD1 on the nanohybrids. Characterization of the nanohybrids: HR-TEM images of (b) the bare CNT and (c) ultrathin cPPy-coated CNT hybrids, and SEM images of (d) a bare nanohybrid and (e) a DRD1-conjugated nanohybrid. The dotted yellow line indicates the thickness of the cPPy layer in (c), and the arrow in (e) indicates DRD1 with detergent.

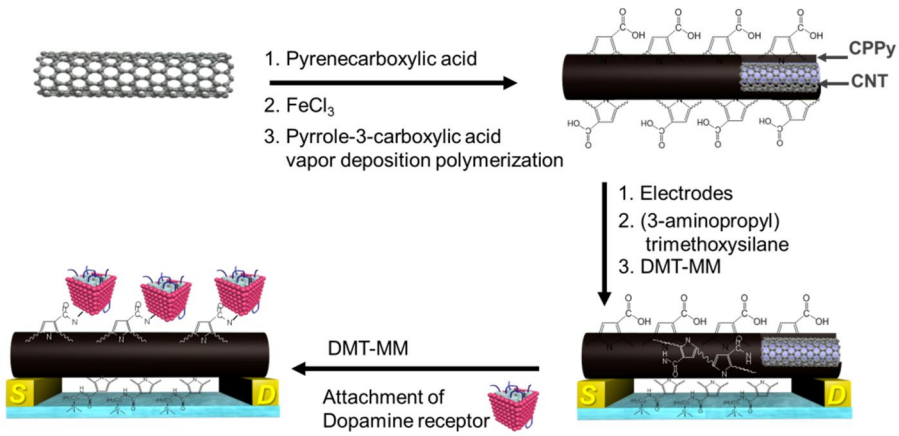

Figure 4.4 Schematic diagram of the fabrication process of DR-nanohybrid-immobilized microelectrodes on substrates.

4.4 Electrical properties of nanohybrids in the FET geometry

To confirm the electrical properties of the nanohybrids in the FET geometry, nanohybrids were assembled using interdigitated microelectrode arrays (IMAs) that were designed on glass wafers using a microelectromechanical system (MEMS) (**Figure 4.5**). Based on previous works, the surface of the IMAs was hydrolyzed, and the condensation process was then conducted using the nanohybrids. First, the electrical contact between the nanohybrids and the IMAs was characterized using current-voltage (*I-V*) measurement. **Figure 4.6a** shows the *I-V* results of the nanohybrids and DRD1-nanohybrids over a range of -1.0 to 1.0 V (10 mV step). Both *I-V* curves were linear with slopes (d*I*/d*V*) of *ca*. 8.6 for the nanohybrids and *ca*. 5.6 for the DRD1-nanohybrids due to the introduction of DRD1. This difference in slope is an indirect sign of the successful attachment of DRD1, and indicates a stable ohmic contact between the electrodes and the nanomaterials. Generally, one way to achieve high sensitivity in biosensors is to increase the amount of bioprobes, which is DRD1 in this case. Thus, *I-V* curves were recorded with increased in the amounts of DRD1 by Bicinchoninic Acid (BCA) assay under fixed conditions: *ca*. 2.88 μg for DRD1, *ca*. 6.03 μg for 2DRD1, and *ca*. 12.58 μg for 4DRD1. The slope values were similar to the above results: DRD1 (5.6) > 2DRD1 (4.7) > 4DRD1 (2.9) (**Figure 4.6b**). Moreover, the maximum amounts of DRD1 were indirectly identified by introducing 8DRD1 and comparing of the slope values, which indicated a limited capacity for DRD1 on the nanohybrids (**Figure 4.7**). Thus, nanohybrids with amounts of DRD1 ranging from DRD1 to 4DRD1 were used for the liquid-ion gated FET geometry.

To analyze the DRD1 agonists-antagonists responses, the liquid-ion gating system was constructed with DRD1-nanohybrids with phosphate-buffered saline (PBS; pH 7.4) as the electrolyte for the IMAs. **Figure 4.6c** shows a schematic illustration of

the liquid-ion gated FET geometry using the DRD1-nanohybrids, which is also composed of two passivated electrodes (source (*S*) and drain (*D*)) to avoid unexpected DA interactions. This strategy using the DRD1 gating modulator has great potential to overcome the limitations of conventional biosensors due to the intimate contact area between the target biomolecules and the DRD1-nanohybrids. To characterize the electrical properties of this FET system, the transfer curve was monitored using a DRD1 gating modulator on the nanohybrids. **Figure 4.6d** shows the I_{ds}-V_{ds} transfer curve at room temperature under controlled gating values (from 0 to -100 mV). Generally, the charge carriers in the p-type transistor, which are holes, accumulated on the surface of the transistor when a negative gating voltage was applied through the liquid environment, leading to negatively increasing current values. However, the amount of a hole will decrease with the increasing positive gating voltage. In the case of this nanohybrid, the I_{ds} values of the transfer curve in **Figure 4.6d** negatively increased when the negative gating voltages increased, resulting in p-type FET characteristics, represented by holes as the charge carrier. Therefore, this FET geometry can be used to observe the DRD1 agonism and antagonism by controlling the DRD1 gating modulator.

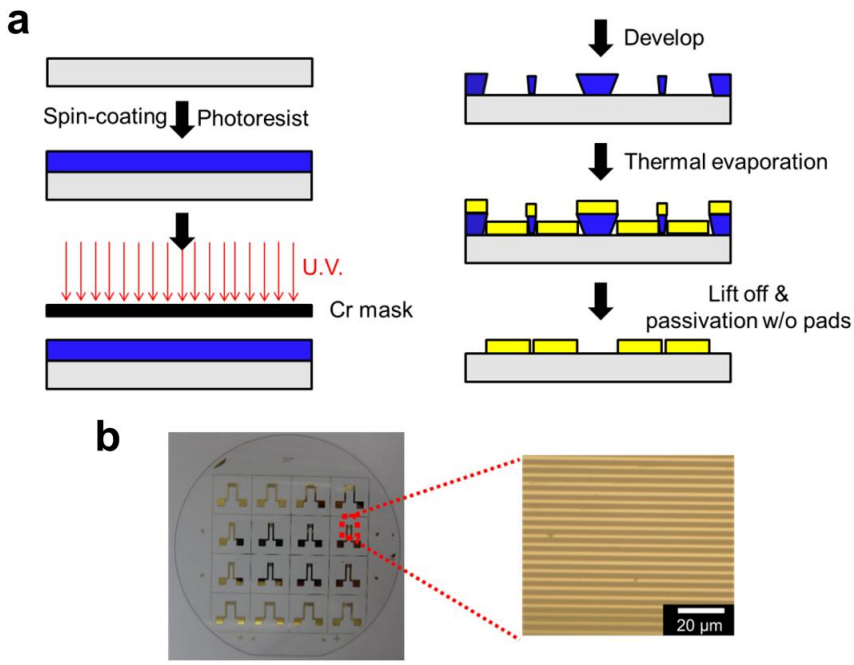

Figure 4.5 (a) MEMS protocol for designing IMAs. (b) Photo image of the IMA electrodes and optical microscopy of the extended IMAs.

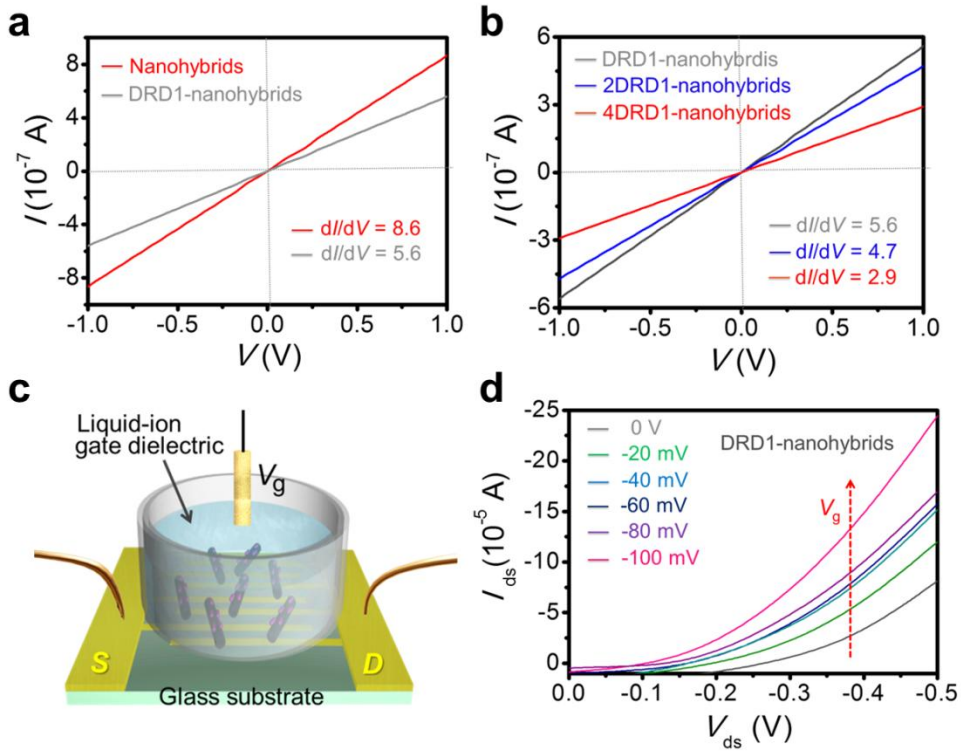

Figure 4.6 Electrical characteristics of the FET geometry: *I-V* values of (a) the nanohybrids and the DRD1-nanohybrids (b) Nanohybrids with various numbers of DRD1. (c) Schematic illustration of liquid-ion gated FET geometry (*S*: source, *D*: drain, V_g: gating voltage). (d) I_{ds}-V_{ds} curves from the DRD1-nanohybrids FET assay with various gating voltages from 0 to -100 mV.

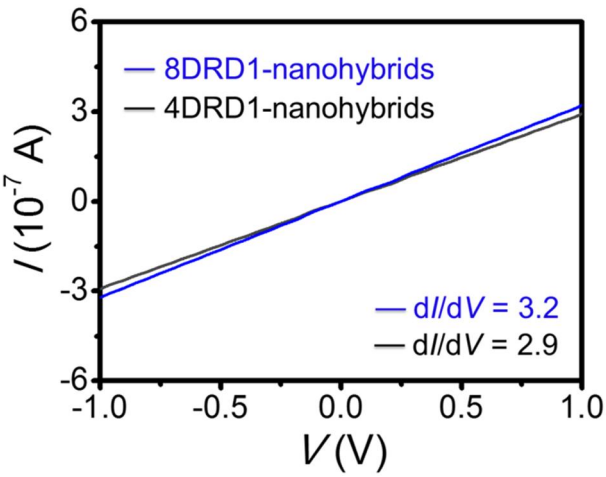

Figure 4.7 *I-V* value of 4DRD1 and 8DRD1 nanohybrids in FET geometry.

4.5 Sensing behaviors of DRD1-nanohybrid FET

To achieve DA sensing with the liquid-ion gated FET system using DRD1-nanohybrids, various chemicals (DA, epinephrine: EP, and serotonin: SE) including agonists (dihydrexidine: DI and SKF 83959: SKF) and antagonists (SCH 23390: SCH and ecopipam: EC) were prepared (**Figure 4.8a**). The real-time response of the FET system was observed while sequentially adding increasing amounts of DA. Significant current changes were observed by introducing various DA concentrations (PBS caused no significant response), and the minimum detectable level (MDL) of the DRD1-nanohybrid FET was *ca.* 10 nM DA. The increasing concentrations of DA generated increasing current in the FET biosensor. Holes, which are the charge carrier of the nanohybrid transistor, accumulated on the surface of the nanohybrids due to the structural recombination of DRD1. Generally, DRD1, which is a gate modulator, has a potential positive charge value in liquid (pH 7.4) because its isoelectric point (p*I*) is 8.64 [87]. The charge state of the DRD1 gate modulator was finely affected by the structural change in the conformation of DRD1. Therefore, the charge of DRD1 changed from positive to the negative when the DA combined with the binding pocket of DRD1, leading to an indirect gating effect [88]. In the real-time response, the DRD1-DA relationship could be monitored using the current values, which increased as the DA concentration increased, as shown in **Figure 4.8b**. Moreover, more DRD1 resulted in greater sensitivity, which is also explained by the indirect charge effect of the DRD1 gate modulator.

To study DRD1 agonism and antagonism, the reliability of the assay is critical and thus the equilibrium constants (K) and the selectivity of the FET assay were characterized. First, to compare the performances of the FET biosensing systems, the most efficient method is to estimate the K value assuming a small molecule

because the Langmuir isotherm model, which is related to the equilibrium between analyte molecules and binding sites, enables predicting their response characteristics. In previous work, *K* was founded using the adsorption and desorption of an olfactory receptor and a small analyte [51]. As a benchmark for the process, *K* is characterized as following equation:

$$N = \frac{C}{1/k + C}$$

K can be calculated from the odorant concentrations (*C*) in the solution and the normalized sensitivity (*N*), which is the same as the $\Delta I/I_0$ values in **Figure 4.8b**. Each *K* value was calculated from the dose-dependent responses and their curve shapes were similar to the curve shapes in **Figure 4.8c**. The *K* values were as follows: 1.4×10^8 (4DRD1) > 1.2 x 10^7 (2DRD1) > 1.2×10^6 (DRD1) > 1×10^{-3} (w/o DRD1). The *K* value (1.4×10^8) significantly corresponds with classical pharmacological methods ($1\text{-}2 \times 10^8$) [89,90]. Second, a selectivity test using the 4DRD1-nanohybrid FET was performed because 4DRD1 exhibited the most sensitive responses. The chemical structures of the introduced EP and SE only differ by one carbon atom, and these chemicals coexist in the nervous system. **Figure 4.8d** shows a real-time response from the 4DRD1-nanohybrid FET. The FET assay showed a current change when 0.1 nM DA was injected, whereas no significant response was observed with high concentrations of SE and EP (PBS was introduced as a control experiment). The results indicate that the FET assay has high selectivity at a low DA concentration. This is due to the native function of DRD1, not the FET itself, immobilized on the nanohybrids. In other words, the result shows that function of the receptor was retained throughout the production, purification, isolation and conjugation of the DRD1. In addition, the stability of

DRD1-nanohybrid FET devices was also characterized by storage test during 10 days. The sensitivity change was observed with *ca*. 5~8 % decrease in sensitivity change (**Figure 4.9**). Thus, this DRD1-nanohybrid FET assay demonstrates high sensitivity and selectivity and is therefore suitable for studying DA agonists and antagonists.

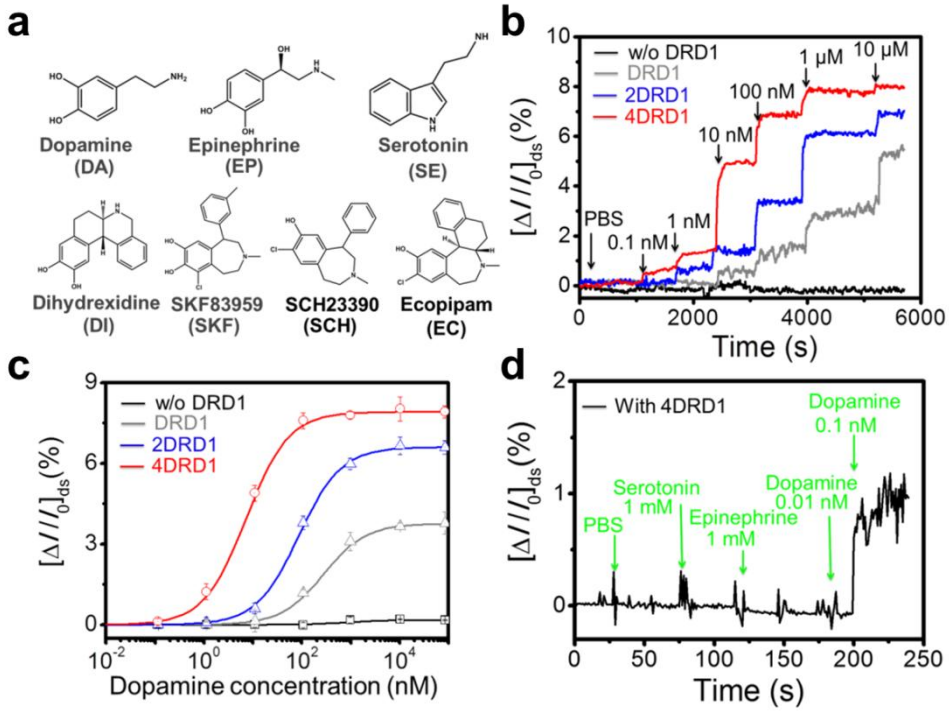

Figure 4.8 (a) Chemical structures of the target (DA), non-target (EP and SE), agonists (DI and SKF) and antagonists (SCH and EC). DA sensing characteristics using DRD1-nanohybrid FET devices: (b) real-time responses for sensitivity at increasing DA concentrations, (c) dose-dependent responses (n=5) and (d) the real-time response for selectivity among the various molecules at high concentrations.

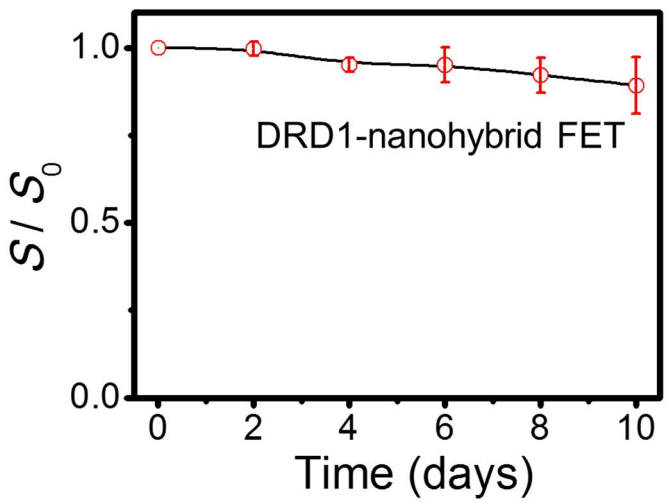

Figure 4.9 Stability test of the DRD1-nanohybrid FET assay at 0.1 nM dopamine concentration (each sample (n=3) were tested at different days from 1 day to 10 day). The nanohybrid FET devices with 4DRD1 were prepared and their stability tests were investigated by storing them in dry air in a sealed vessel at 25 ^{o}C during 10 days. The DRD1-nanohybrid FET assay showed *ca*. 5~8 % decrease in sensitivity change (S/S_0) during 10 days.

4.6 Analyzing DRD1 agonism and antagonism characteristics

Generally, when studying receptor agonism and antagonism, the preparation of the reconstituted DRD1 is critical because well-reconstituted GPCR allows native binding pockets, which determine the strength of the affinity between the receptors and the agonists and antagonists [91]. Therefore, the reconstituted DRD1-attached FET assay was utilized to compare the binding activity for each agonist. First, the DRD1 agonism on the FET was characterized by the real-time responses with DA, DI, and SKF molecules because DA agonists have different affinities to DRD1 and enable the transfer of significant signals (**Figure 4.10a**). When the DA and DA agonists bind DRD1, the different binding signals for each case can be detected using the DRD1-immobilized FET. The structural change of the receptor, which is indirectly proportional to the binding activity, leads to the gating effect of the FET biosensing systems. **Figure 4.10b** shows the real-time responses to DA and DA agonists at low concentrations. For the DA detection levels using the FET system, DI shows a similar DA sensitivity level (1 nM), while SKF has a relatively low sensitivity level (1 μM). To compare their *K* values, the dose-dependent responses were characterized as shown in **Figure 4.10c**. The order of the *K* values was as follows: DA (1.4×10^8) > DI (1.8×10^7) >> SKF (3.3×10^5). This finding shows that DI is a fully effective DRD1 agonist, and SKF is a partially effective agonist. Interestingly, this result agrees well with classical pharmacological studies that show that the binding effect of partial or potent agonists on the structural change of the receptor is less than the effect of the ligand or strong agonists [92,93]. Moreover, the curves of *K* in **Figure 4.10c** shift to the right as the receptor affinity of the agonists decreases.

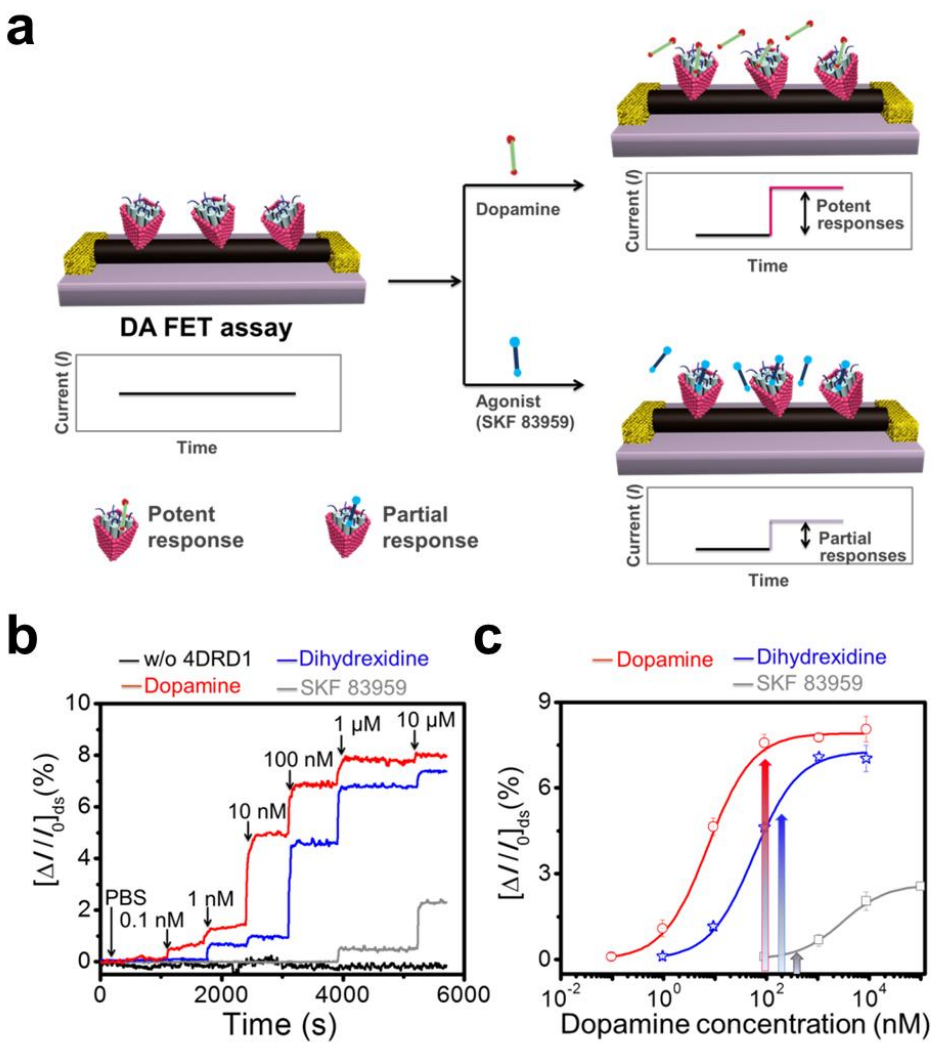

Figure 4.10 Analyzing DRD1 agonism using the DRD1-nanohybrid FET assay: (a) schematic diagram of the DRD1 agonism mechanism, (b) real-time responses to dihydrexidine, SKF 83959 and DA ((from 0.1 nM to 10 μM) and (c) related dose-dependent responses (n=5).

To confirm the DRD1 binding affinity to DA using antagonists as the DRD1 blocker, the antagonism was first considered to design the experimental conditions. Antagonists can block receptor/ligand binding by competitively or non-competitively binding with the ligand. Antagonists can bind to receptors through various mechanisms, but there were no efficacy toward their receptors. Therefore, no receptor signal transfers were observed (**Figure 4.11a**) [57,94]. Based on the DRD1 antagonism, antagonists such as SCH and EC were previously introduced into the liquid-ion gated FET assay to interfere with DA binding. Although each antagonists has a different affinity for the DRD1 (EC > SCH) [95], no significant response was observed when the antagonists were injected into the liquid-ion gated DRD1-nanohybrid FET system (**Figure 4.12**). However, each affinity levels of the antagonists enables significant differences in the sensing performances of the FET assay, as shown in **Figure 4.11b**. The real-time responses using the FET assay are displayed for DA and for two different antagonists (SCH and EC). The real-time response of DA is shown in **Figure 4.10b** for a consistent comparison of the results. The affinity differed significantly before and after antagonist pretreatment; the current change level of the DA without the antagonist pretreatment was fully reached at the saturated concentration, whereas the current levels for DA after antagonist pretreatment of antagonists were clearly reduced, and the MDL (0.1 nM) of the DRD1-FET system with no pretreatment was 2 or 5 orders of magnitude less than the MDL of the FET systems with the antagonists. Moreover, comparison of the two antagonists, indicated that, the affinity to DRD1 is lower for SCH than for EC because the MDL (1 μM) of DA after EC pretreatment of EC is higher than that of SCH (1 nM). Moreover, the normalized current change value found using the FET assay was greater than 8 at 10 μM DA. However, the maximum normalized current values after SCH and EC pretreatment were as high as to 80 % and 20 % at

the same DA concentration (10 μM). These results are explained by the remarkably reduced binding of DA toward DRD1 because of the response blocking of SCH and EC as surmountable antagonists. The maximum response of DRD1 could be expected to be almost recovered when the higher concentration of DA is treated to the blocked DRD1. This finding also corresponds to previous reports showing that the strongest blocking effect of reconstituted DRD1 is found for EC rather than SCH [95]. Furthermore, to investigate the DRD1 antagonism, the dose-dependent responses from the FET system were characterized by fitting the experimental data in **Figure 4.11b** and the *K* values were estimated based on the Hill equation. The *K* value (8.1×10^6) from the FET assay after SCH pretreatment was higher than the *K* value (3.5×10^4) from the FET with EC, the result of which was highly consistent with the previous results from conventional cell-based assays [96,97]. Moreover, the curves with these *K* values shifted to the right when the *K* values decreased, resulting in the same theoretical DRD1 agonism foundation, as shown in **Figure 4.10b**.

When comparing these *K* values with the values from the classical cell-based method, the shift in the calculated *K* values is consistent with the *K* of DRD1 in the cell-based assay. However, the *K* values from the FET assay could be different from the *K* values calculated from conventional cell-based assay, because the FET platform is consisted of purified DRD1, not the G protein complex. The general receptors exist with G protein in mammalian cells, while the purified receptor was solely reconstituted in detergent micelles, which lead to binding affinity that is slightly different from the receptor in the native membrane [4]. In addition, when the reconstituted receptor was treated with agonists or antagonists, it would have a thermodynamically stable state that is slightly different from the native receptor with the G protein complex, which could result in a different affinity of the

receptor to the agonists and antagonists [74]. For these reasons, the *K* value from the reconstituted receptor without accessory proteins in the ligand binding assay would be lower than that of the receptor in an intact cell, the result of which could also increase with the G protein complex in the FET assay [98,99].

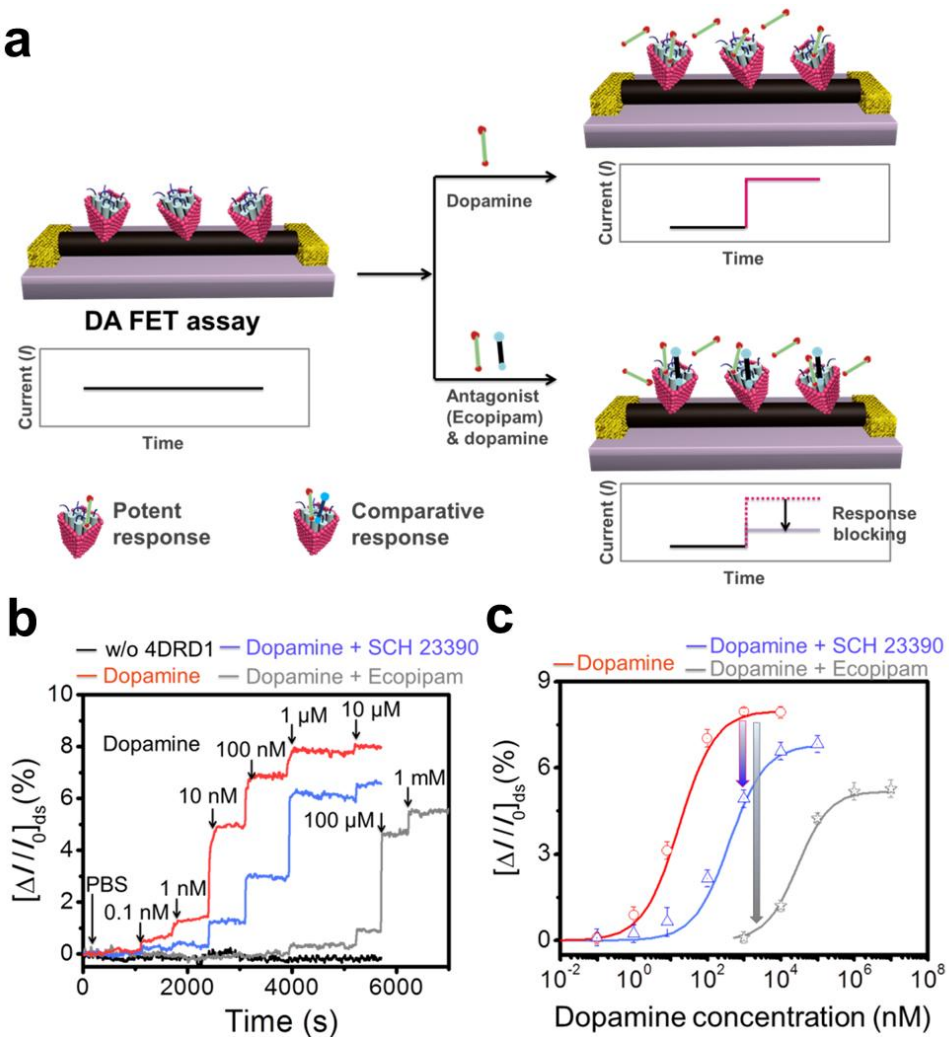

Figure 4.11 Analyzing the DRD1 antagonism using the DRD1-nanohybrid FET assay: (a) schematic illustration of the DRD1 antagonism mechanism, (b) real-time responses to DA (from 0.1 nM to 10 μM) after the introduction of 100 nM SCH 23390 and 100 nM Ecopipam and (c) the related does-dependent responses (n=5).

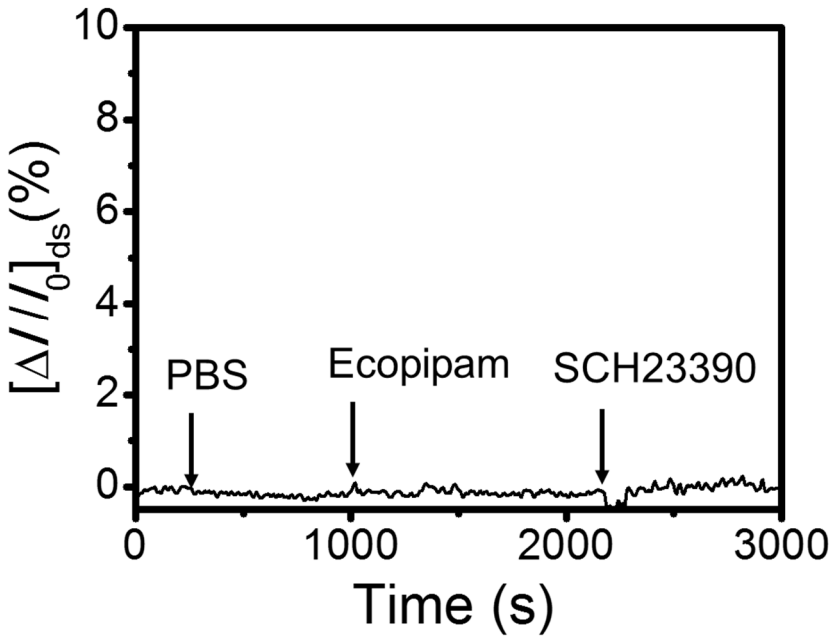

Figure 4.12 Real-time responses of FET assay with antagonists (100 nM Ecopipam and 100 nM SCH 23390).

4.7 Conclusions

We proposed an analytical method to replace cell-based receptor agonism and antagonism studies; this method is termed a reconstituted DRD1-conjugated nanohybrid FET assay. Well-designed and reconstituted DRD1 allows native binding pockets and high sensitive and selective DA detection, mimicking the DRD1 agonism and antagonism. The FET assay exhibited a significant response to the DRD1 agonists and antagonists. Specifically, the equilibrium constants (K) were estimated by fitting the experimental data (real-time responses), and the equilibrium constants exhibited a rightward shift with a decrease in the K value, which indicates strong DRD1 agonists and antagonists. This finding suggests that the well-reconstituted GPCRs conjugated FET system could successfully replace cell-based assays and could mimic native-receptor functions. In addition, a GPCR-based FET biosensor had a significant advantage in the highly specific and sensitive recognition of ligands and could offer well-organized systems for multiplexed agonist and antagonist detection in a mixture. Furthermore, this could be applied to receptor-based research, such as protein/protein interaction, drug discovery and GPCR localization studies.

Chapter 5

Assembly of receptor-embedded nanodiscs and its application to the biosensor for the assessment of death associated-odor cadaverine

5.1 Introduction

GPCRs play important roles in the cellular responses of the human body. Thus, they are significantly involved in many human diseases and are the target of approximately 40% of all modern medicinal drugs [71,70]. Trace amine-associated receptors (TAARs), a class of GPCR, are conventional amine receptors binding to endogenous compounds structurally related to classical biogenic amines. It has been reported that TAAR13c in the zebrafish (*Danio rerio*) functions as an olfactory receptor (OR) and has an efficient specificity to the death-associated odor CV [100-103]. CV, generated by bacterial decarboxylation of lysine, is an extremely repulsive odor to humans, among various biogenic amines. In addition, CV is one of the important markers for decayed foods because various kinds of food products contain lysine. Therefore, it has been suggested that the detection of CV can be applied to various fields of industrial applications and scientific investigations [100,104].

For the production of recombinant proteins, the *E. coli* has been widely used as a host cell because of its great advantage in productivity and convenience. However, the production of GPCR in *E. coli* remains a challenge because of their strong hydrophobicity, a complicated charge distribution and membrane inserting mechanism of bacterial cells [105,106,7].

Among many reconstitution techniques of receptors, NDs have been considered the most appropriate tool for GPCR reconstitution [16,4]. NDs are composed of a receptor, a lipid bilayer and MSPs, which tightly wrap the edge of the a lipid bilayer, thus NDs can be stable in an aqueous environment[10, 12-14] and mimic the native structure of the receptor in a cell [14,107]. An ND-based biosensor using Sf9 insect cells has also been reported [14]. However, an ND-based biosensor

using an *E. coli* system, which has great advantages in productivity over other systems, has not been previously reported. A CNT-FET with floating electrodes can exhibit improved performance compared with a conventional CNT-FET [108,109]. The floating electrode structure on a CNT-FET can enhance the sensitivity of the device *via* the increased effect of Schottky barrier modulation. The Au floating electrodes also have advantages in the functionalization of specific biomolecules on their surfaces. The surfaces of floating electrodes have larger areas than conventional devices as well as more suitable conditions for the functionalization of biomolecules.

Here, the development of an oriented ND-functionalized bioelectronic nose (ONBN) using T13NDs with high selectivity and sensitivity was reported for the detection of CV. The T13NDs using receptors produced in *E. coli* enable the immobilized receptor to have stability and a natural binding pocket. Moreover, the T13NDs were immobilized on floating electrodes of a CNT-FET in a desired orientation, which increased the total binding sites of T13NDs. As a result, the ONBN exhibited improved performance in terms of sensitivity and selectivity, as well as reliability and reproducibility. Furthermore, the ONBN could distinguish the target molecules in food samples with differing degrees of spoilage. This approach can offer a remarkable sensing system toward a practical bioelectronic sensor to enable the detection of death-associated compounds.

5.2 Binding property analysis of TAAR13c using cell-based assay

A dual-glo luciferase assay system, which was suitable for the characterization of the TAAR13c in terms of its selectivity, was used to measure the dose-dependent response of TAA13c expressed in HEK-293 cells (**Figure 5.1a**) [110]. TAAR13c-expressed cells exhibited a significant response to CV, but mock vector-

transfected cells had no meaningful responses. This supports the conclusion that TAAR13c was successfully expressed in HEK-293 cells (**Figure 5.1a, 5.2a**). **Figure 5.1b** shows the selective responses of TAAR13c to 1 μM stimulus of various amines. TAAR13c was co-expressed with RTP1S and $G_{\alpha olf}$, increasing the level of expression and efficiency of signal transduction. The selective binding properties of TAAR13 were investigated using various amines, which had different amine moieties and structures (**Figure 5.2b**). This results show TAAR13c responded selectively to CV among various amines. Although putrescine (PT) appeared to stimulate the TAAR13c partially, there were no significant responses. The results are consistent with previous reports that TAAR13c is the most sensitive and selective receptor to CV [102,100].

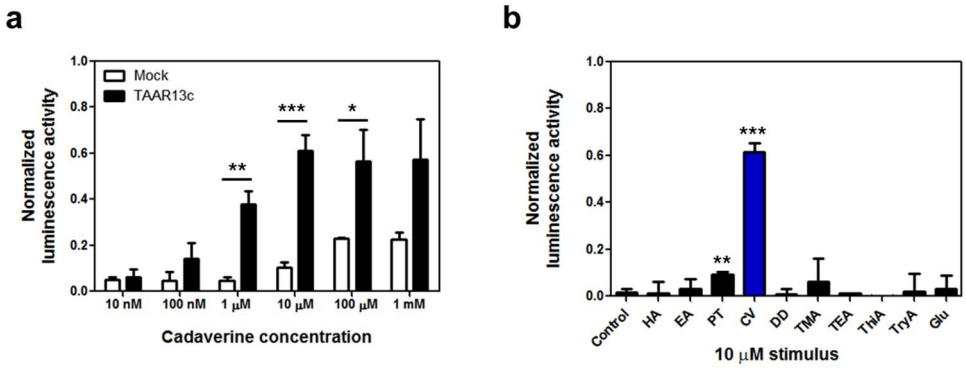

Figure 5.1 Characterization of TAAR13c expressed in HEK-293 cells. (a) Dose-dependent response of TAAR13c to the CV ($^{*}p<0.05$, $^{**}p<0.01$, $^{***}p<0.001$) (n=3). The error bars represent the standard error of the mean. (b) Selectivity of TAAR13c with various amines (HA, hydroxylamine; EA, ethanolamine; PT, putrescine; CV, cadaverine; DD, diaminodecane; TMA, trimethylamine; TEA, trimethylamine; ThiA, thiamine; TryA, tryptamine; Glu, glutamine) (n=3). The error bars represent the standard error of the mean.

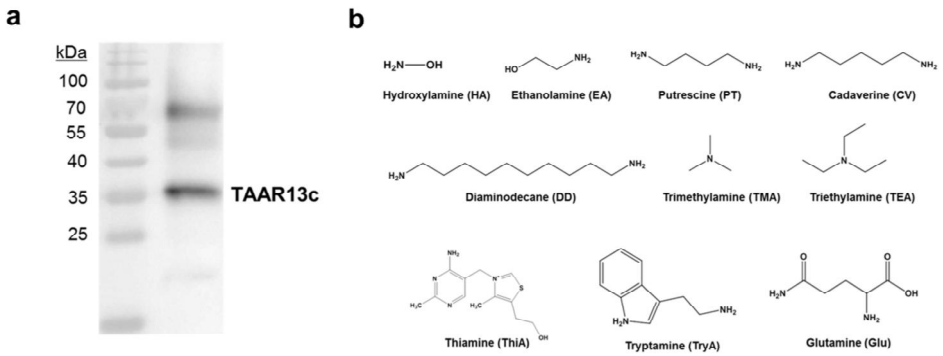

Figure 5.2 (a) Western blot analysis of HEK-293 cells expressing TAAR13c. The western blot analysis was performed with FLAG Ab. (b) Various tested amines which were organized by amine moiety and carbon-atomic differences.

5.3 Production, optimization and characterization of TAAR13c-embedded nanodiscs

Toward a receptor-based research, the TAAR13c expressed in *E. coli* (**Figure 5.3a**) was purified with a high-purity and applied to the formation of receptor NDs. The purification and functional reconstitution of GPCRs for the development of receptor-based biosensors were reported previously.[7,30] For the production of T13NDs, TAAR13c and lipids were mixed as detergent micelles, and then the membrane scaffold protein apolipoprotein A-I (ApoA-I) was added to enclose the lipid/receptor complex. The T13NDs were finally obtained after the removal of detergent using Bio-bead. The bands of TAAR13c in gel staining indicate that TAAR13c was purified with a high-purity. Moreover, the observed bands were successfully confirmed as TAAR13c by a western blot analysis using V5 epitope Ab, confirming that TAAR13c was prepared with a high-quality.

For the assembly of the T13NDs, ApoA-I, the representative membrane scaffold protein, was successfully expressed in *E. coli* and purified with a high-purity (**Figure 5.3b**). Dynamic light scattering (DLS) measurement of T13NDs (**Figure 5.3c**) indicated that size distribution of optimized T13NDs. After the assembly of the NDs, the ND-complex solutions were subjected to size exclusion chromatography (SEC) for the removal of residual unbound proteins (**Figure 5.4**). The fraction of T13NDs from the SEC separation was collected and analyzed by DLS [111]. A various conditions were tested, such as lipid sonication time and protein concentration for the formation of receptor-NDs and found the best choice for the formation of optimized T13NDs (**Figure 5.5**). This results in a quite narrow size distribution of T13NDs with *ca.* 20 nm in diameter (**Figure 5.3c**), which is close to the diameter values estimated by FE-SEM images (**Figure 5.3d**). These

results clearly demonstrate that the T13NDs were successfully self-assembled in homogeneous discoidal shapes.

In order to analyze the affinity of T13NDs with CV, the real-time tryptophan fluorescence of T13NDs was measured (**Figure 5.3e**). With the sequential addition of increasing CV amounts up to 7 mM, a significant fluorescence change of T13NDs was displayed. On the other hand, there was no response to the control buffer solution. The T13NDs responded selectively to CV in real-time tryptophan fluorescence (**Figure 5.3f**) in comparison with various amines which have different structures and amine moieties. The intrinsic tryptophan fluorescence of T13NDs was significantly quenched only by a stimulus of CV. Many researches have reported that the intrinsic fluorescence of functional receptor is quenched by selective binding of a ligand to the receptor.[7,6,17] Therefore, these results show that the TAAR13c was effectively reconstituted in NDs.

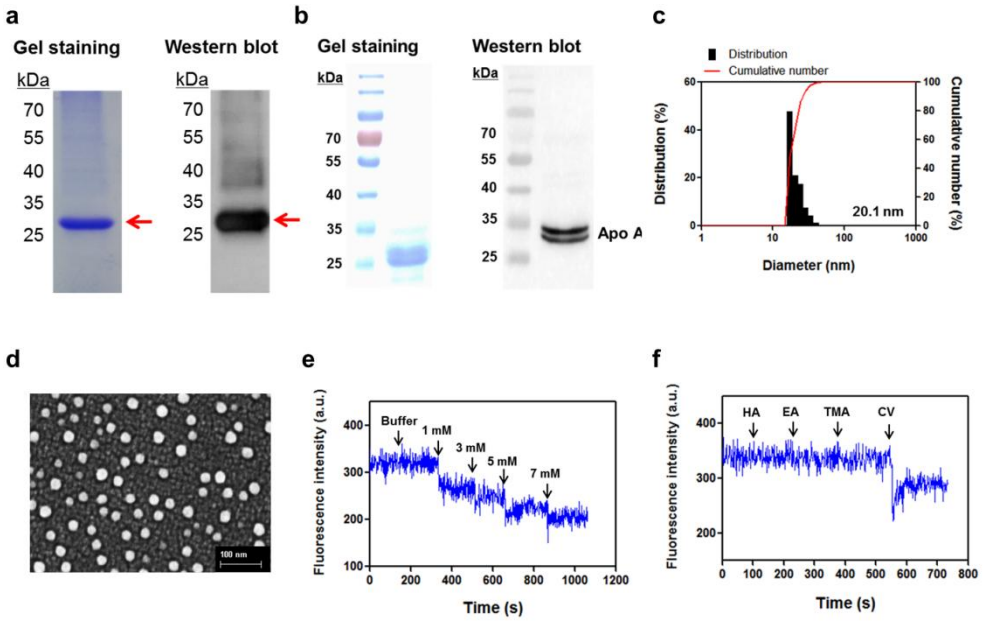

Figure 5.3 Characterization of high-quality TAAR13c-embedded NDs. The purified TAAR13c in NDs was produced in *E. coli*. (a) SDS-PAGE analysis of purified TAAR13c produced in *E. coli*. The western blot analysis was performed with V5 Ab. (b) Gel staining and western blot analysis of purified ApoA-I. The ApoA-I was highly purified. And the western blot analysis was performed with His-Probe Ab. (c) DLS size distribution of optimized T13NDs. (d) FE-SEM image of T13NDs. (e) Real-time tryptophan fluorescence of T13NDs with increasing concentration of the CV. (f) Selective response of T13NDs to CV measured by real-time tryptophan fluorescence.

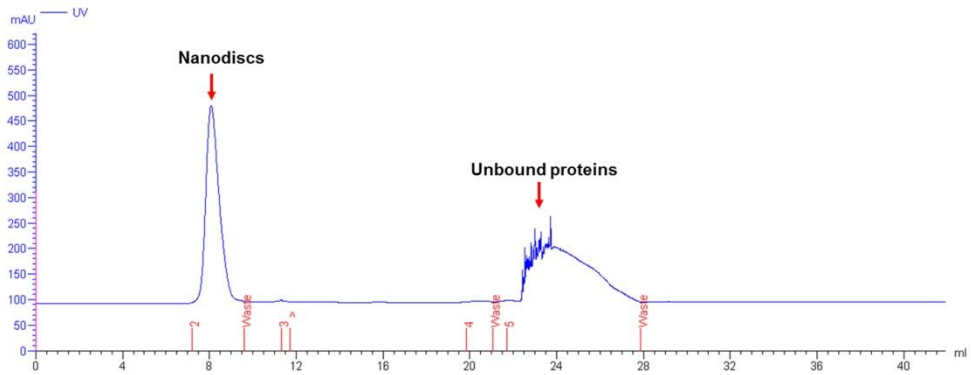

Figure 5.4 Separation of T13NDs from ND-mixture solutions using size exclusion chromatography. The TAAR13c-embedded NDs were successfully purified with the SEC column.

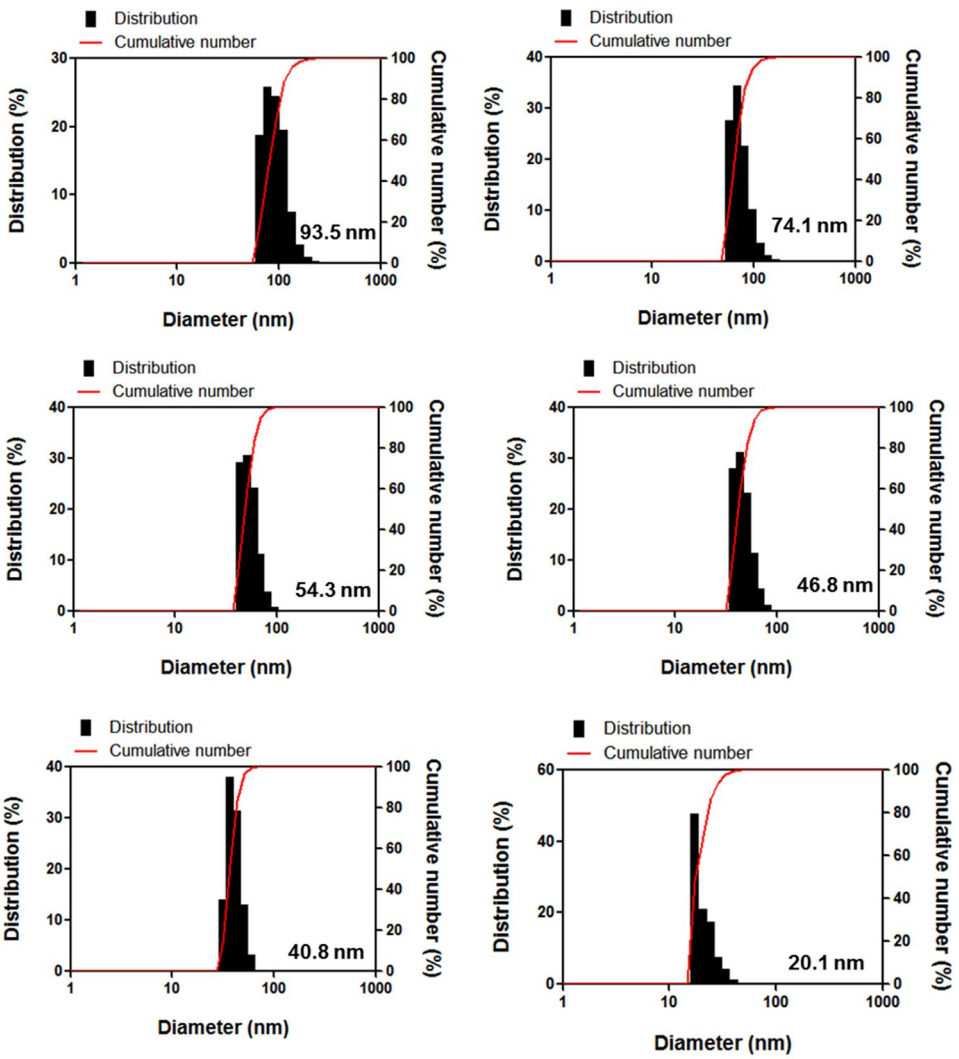

Figure 5.5 DLS results of T13NDs purified in various conditions. The size of NDs was minimized (~20 nm) with optimization such as lipid sonication time (10-60 min) and protein concentrations (0.5-2 μM). The optimized condition was 30 min (lipid sonication time) and 1 μM (protein concentration).

5.4 Concept of oriented ND-functionalized bioelectronic nose (ONBN) for the assessment of death-associated odor cadaverine

Figure 5.6 depicts the schematic diagram and the predicted electrical response of an ONBN. A CNT-FET with floating electrodes was fabricated following previously-reported processes. A detailed method is described in Supporting Information (**Figure 5.7**). In brief, CNTs were patterned on a SiO_2 substrate as transistor channels, and then, Pd/Au electrodes were fabricated *via* thermal evaporation method. Finally, the source and drain electrodes were passivated using a photoresist to avoid a current leakage in an aqueous environment. After the fabrication of the device, T13NDs were immobilized on the Au surfaces of the floating electrodes. In this research, the half V5 antibody (Ab) was used as linker molecules for oriented immobilization of T13NDs on gold floating electrode. It has been reported that half-fragment antibodies can be immobilized onto the gold surfaces with an orientation *via* their native thiol groups [112]. The receptor TAAR13c has a V5 epitope at C-terminal. Therefore, the T13NDs can be immobilized with the desired orientation using half-fragment V5 Ab as a linker. Here, the V5 epitope of T13NDs binds to the half-fragment V5 Ab on the Au surface. The immobilized T13NDs on the Au surfaces were oriented such that the binding pockets of TAAR13c on the device were on the exposed side. In previous work, devices with randomly immobilized biomolecules also have been reported [113,60]. However, randomly oriented sensors have a limited capability to bind target molecules. Therefore, ONBNs could provide an ideal method for the detection of specific target molecules.

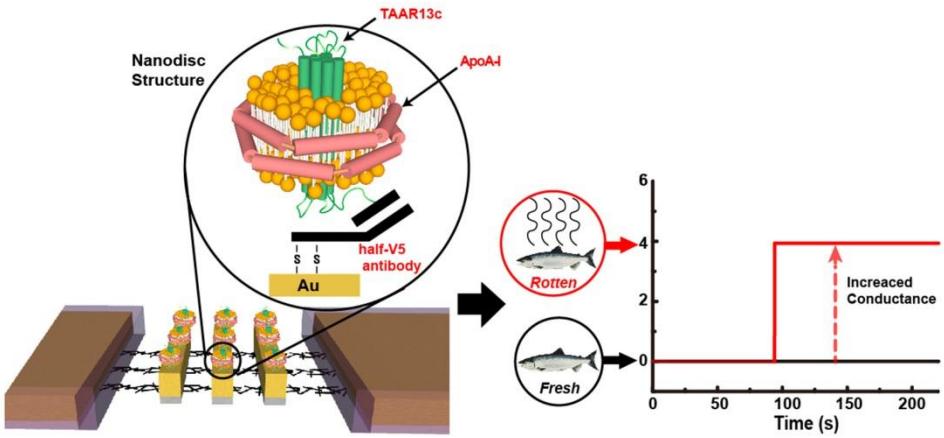

Figure 5.6 Schematic diagram of an ONBN. This figure illustrates the ONBN and possible sensor response curves of an ONBN. T13NDs were successfully immobilized on floating electrodes of a CNT-FET, which leads to a high-performance ONBN. The ONBN could selectively discriminate spoiled foods from fresh samples.

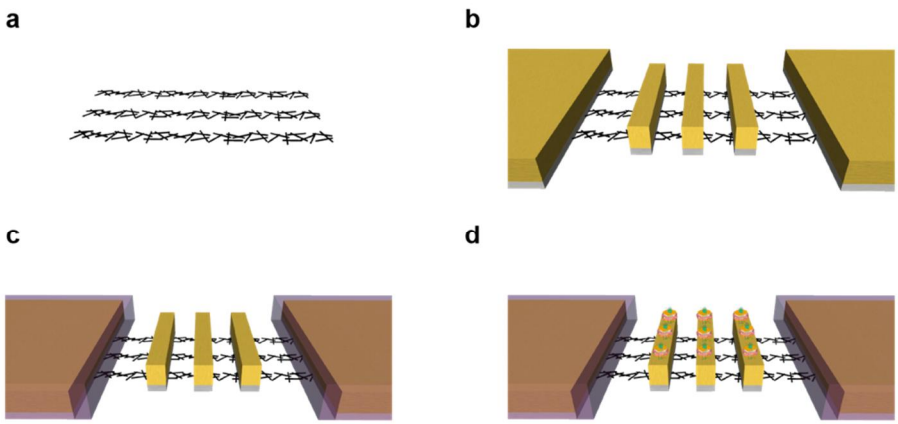

Figure 5.7 The fabrication process of an ONBN. (a) CNTs were patterned in SiO_2 substrates as the channels (b) Source, drain and floating electrodes (Pd/Au, 10/30 nm) were fabricated *via* thermal evaporation method. (c) The source and drain electrodes were passivated by the photoresist to prevent current leakage in aqueous conditions. (d) T13NDs were immobilized on the Au surfaces of the floating electrodes.

5.5 Sensing performance of ONBN

Figure 5.8a shows the real-time response of an ONBN to various concentrations of CV. Here, while adding various concentrations of target solutions, drain-source currents of the ONBN were measured using a semiconductor analyzer. The drain-source bias voltage was maintained as 0.1 V during the measurement. To monitor the response of ONBNs to CV, the buffer zone of 9 μL HEPES solution was developed. After 100 s, 10 pM CV solution of 1 μL was consecutively added onto the buffer zone. In a similar manner, CV solutions were introduced from a low concentration to a high concentration by the factor of 10 at each time. The concentrations of added solutions were calculated by considering the increased solution volume. Then, the measured data of current changes during the additions of CV were normalized by the original current values to estimate the normalized conductance change G/G_0. Note that the conductance of the ONBN was sharply increased after adding various concentrations of CV solutions. The ONBN exhibited increased conductance by CV solutions with concentration as low as 10 pM, indicating the high sensitivity of device. The control experiment using TAAR5 which does not respond to CV was also performed. The TAAR5-embedded NDs (T5NDs) were assembled, immobilized the T5NDs on floating electrode of CNT-FET and tested with increasing concentration of CV (**Figure 5.9**). The CV was added up to 100 μM; however there is no meaningful response. Thus it could be concluded that the ONBN selectively binding to CV was effectively constructed. Moreover, for CV, in sauerkraut, fish, cheese, fermented sausages and seasonings, maximum tolerable levels are about 4.2, 5.0, 5.3, 10.6 and 15.07 μM, respectively [114]. The limit of detection of ONBN is about 10 pM which is much lower than that of tolerance of CV in various foods. Therefore, this platform could be practically used to assessment of food quality. The plausible mechanism for this

response is that the binding of protonated positively-charged CV molecules to TAAR13c increased the work function of the floating electrode [102]. Thus, the binding of CV decreased the Schottky barrier for hole carriers in the device and increased the conductance of the ONBN device [115].

Figure 5.8b shows the graph for the normalized sensitivity N of ONBNs at different concentrations of CV. The normalized sensitivity was estimated by normalizing the sensor sensitivity ($|\Delta G/G_0|$) with respect to its maximum sensitivity value [116-118,53]. The measured response curves can be analyzed using the model based on the Langmuir isotherm theory as previous studies [119]. In this model, the density C_s of CV molecules bound to the T13NDs on an ONBN can be written as

$$C_s = \frac{C_{s\,max} \cdot C}{1/K + C} \tag{1}$$

where C and K represent *the concentration of odorant in a solution* and *an equilibrium constant between odorant and T13NDs*, respectively. $C_{s\ max}$ is the density of T13NDs on the electrodes of an ONBN. The binding events between CV and T13NDs induced increased conductance. If it is assumed that a conductance change ΔG is linearly proportional to the number of bound CV molecules on T13NDs, a sensor sensitivity can be approximated as $|\Delta G/G_0| \sim kC_s$, where k is a constant representing the response characteristics of an ONBN. Therefore, the sensor sensitivity could be written as

$$|\Delta G/G_0| = k\frac{C_{s\,max} \cdot C}{1/K + C} \tag{2}$$

As C becomes very large, the sensor sensitivity $|\Delta G/G_0|$ could converge to $k \cdot C_{smax}$. Thus the normalized sensitivity N can be written as

$$N = \frac{C}{1/K + C} \tag{3}$$

By fitting the measured data with this model, the equilibrium constant *K* between T13NDs and CV as 3.63×10^{11} M^{-1} could be estimated, which is a rather large compared with previously-reported values measured using cells or biological systems. This result implies that the ONBN device can detect target CV molecules with a much higher sensitivity than cells or biological systems. Moreover, these results demonstrate that the ONBN show the reproducible signals in repeated experiments.

Figure 5.8c shows the real-time response of an ONBN to various molecules containing amine functional groups. Here, diaminodecane (DD), trimethylamine (TMA), ethanolamine (EA), glutamine (Glu) and CV molecules were injected to the ONBN in series while measuring the sensor responses. DD and EA have the similar structures with CV, TMA has a fishy odor, and Glu is an amino acid. The structures of these molecules are presented in **Figure 5.2b**. Note that the ONBN device exhibited negligible sensor responses to non-target molecules even at a relatively high concentration of 1 μM. However, the conductance of the ONBN increased sharply by adding CV at a concentration of 1 nM, which is 1000 times lower concentration than that of non-target molecular species. This result clearly shows that the ONBN can selectively detect CV at a very low concentration even in the presence of high concentrations of similar molecular species.

Figure 5.8d shows the responses of ONBNs to various real-sample solutions obtained from spoiled foods. Each tested food sample was prepared in HEPES buffer solution and filtered by ultrafiltration membranes (see METHODS section). The ONBN exhibited a higher response to samples from salmon and beef with a longer spoilage period. On the other hand, the samples from salmon with sorbic acid, one of the preservatives, exhibited decreased sensor responses, presumably due to the reduced spoilage of the salmon by sorbic acid. It indicates that the

ONBN devices can be used to evaluate the quality of real-food samples *quantitatively*. Interestingly, the pork fat sample showed negligible sensor responses even after a long spoilage period. This is presumably because CV, the target of the ONBN device, is the product of a decarboxylation of lysine which existed in salmon and beef at a large quantity, but not in pork fat [120]. These results indicate the ONBN devices can be utilized to evaluate the quality of various real-food samples quantitatively under complex environmental conditions.

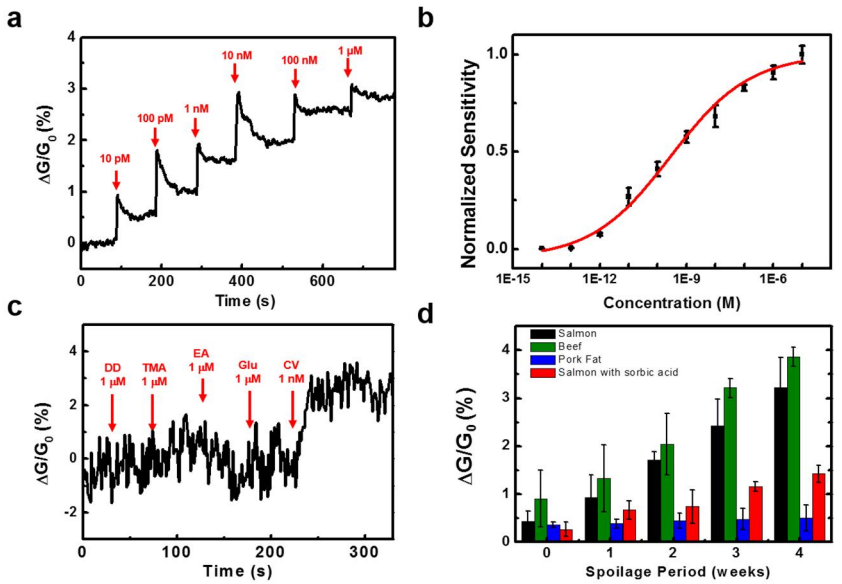

Figure 5.8 Responses of ONBN devices to various samples. (a) Real-time response of an ONBN to the various concentrations of CV. The additions of CV solution induced the increase of conductance of the ONBN in dose-dependent manner. (b) Dose-dependent response curve of the ONBN to CV (n=3). The error bars represent the standard error of the mean. By fitting the data using Eq. (3), the equilibrium constant K was estimated as 3.63×10^{11} M^{-1}. (c) Real-time response of an ONBN to various molecular species with amine functional groups. Non-target molecules caused negligible conductance changes of the ONBN. (d) Comparison of the sensor responses of ONBN devices to different spoiled food samples (n=3). The error bars represent the standard error of the mean. As the spoilage period for salmon and beef increased, the ONBN devices exhibited higher sensor responses.

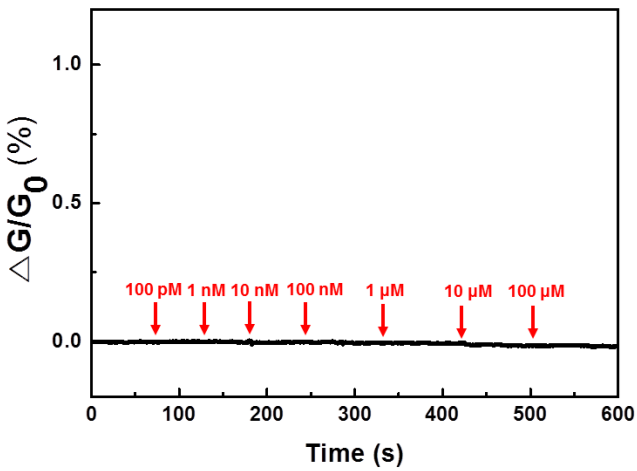

Figure 5.9 Real-time response of T5NDs-immobilized CNT-FET with floating electrode to the various concentrations of CV. The CV was added up to 100 μM; however, there is no meaningful response.

5.6 Conclusions

In conclusion, a highly-stable ND-based bioelectronic nose was developed for the detection of CV. The NDs were successfully constructed with TAAR13c produced in *E. coli*. TAAR13c receptors in ND keep the native receptors properties and permit highly sensitive and selective detections of CV. Especially, the immobilization of T13NDs in a desired orientation on floating electrodes *via* linker molecules enabled a high density of recognition elements and active binding pockets in the ONBN devices, which results in its high sensitivity and selectivity. Furthermore, an ONBN measured CV quantitatively in real-food samples with different spoilage periods. These results show that the ONBN device based on high-quality GPCR-conjugated FETs is attractive technique for the detection of food spoilage and has a great potential for other practical applications such as detection of corpses.

Chapter 6

Development of nanodisc-based high-performance biosensor for the detection of liquid and gaseous cadaverine

6.1 Introduction

Nano-electronic sensors using FET have been developed to detect the specific targets, which leads to the development of bioelectronic sensors [3]. Moreover, the device containing stable and qualitative biomolecules, especially GPCRs, precisely and rapidly binding to their specific target can be powerful tool for a development of a practical biosensor [15]. Especially, the detection of gaseous target can be practically used to various fields, such as a diagnosis of disease, healthcare monitoring and disaster responses [12]. However, the development of stable bioelectric sensor with high-quality GPCRs, which allows reproducible and rapid responses, remains a challenging, because of the stability, reliability and reusability of biomolecules and nanomaterials [12].

CV is the highly strong repulsive odor to human among the various biogenic amines. This smell is often generated by bacterial decarboxylation [121]. Many reports have investigated that the specific amine sensing system can be applied to monitoring the food spoilage, clinical diagnosis and health care services [122,123]. Moreover, it has been expected that the sensitive and selective detection of the CV can be applied to various fields of the industrial applications and scientific investigations [12]. Although a lot of efforts have been made to develop amine-detection sensors for several decades, their specificity still remains challenges because the detection of the target molecule was relied on the interaction to amine moiety [55,122].

The Ni-decorated cPPyNP could provide the NDs of stable immobilization with highly uniform and efficient charge transfer [124]. Moreover, the immobilization using Ni particle enable to much better stability than other approach for sensing of

analyte in the sensing phase and quantitative analysis [17]. The oriented immobilization of receptor on the device enable to increase the total number of recognition elements [1]. It has been reported that randomly oriented recognition elements may reduce the amplitude of the signal emitted after ligand binding, thus they lead to have a limited capability to bind target molecules [60].

Here in, the ND-based high-performance biosensor was developed for the detection of liquid and gaseous cadaverine. The T13NDs was successfully constructed and the T13ND-conjugated Ni-decorated cPPyNP in FET were successfully assembled to detect the liquid and gaseous CV. The T13NDs could mimic the native-like binding pocket of natural receptor and exist with high-stability in the aqueous and dried conditions. The Ni-decorated cPPyNP could enhance the sensor sensitivity and enable to the oriented immobilization of NDs on the FET. As a result, the ND-based biosensor can have a high-stability and reliability as well as a high-sensitivity and selectivity. Moreover, they also can detect the gaseous CV with high sensitivity, stability and reusability. Furthermore, this platform detects the CV in the real-samples by the extent of corruption. This study can be used as an attractive methodology for the receptor-based detection of liquid and gaseous target.

6.2 Fabrication of nanodisc-conjugated Ni-decorated cPPyNP in FET

To detect the CV effectively, T13NDs were applied. The TAAR13c-detergent micelles (Mi) were also formed and tested to be compared with T13NDs. **Figure 6.1** schematically shows T13NDs-conjugated Ni/cPPyNPs (ND_Ni/cPPyNPs) based FET sensor configuration and **Figure 6.2** illustrates the detailed fabrication steps of ND_Ni/cPPyNPs based FET sensor. Above all, **Figure 6.2a** suggests the sequence of steps for the fabrication of Ni/cPPyNP. Nickel nanoparticles were

easily decorated on the cPPyNPs surface through chemical reduction process. As shown in **Figure 6.3a**, mono-dispersed cPPyNPs with ~100 nm diameter were prepared by the method in previous work [125]. The cPPyNPs aqueous solution was stirred uniformly and hydrazine monohydrate was injected to make base condition. $NiCl_2$ aqueous solution was added to the solution at room temperature to make covalent bonding between the Ni^{2+} ions and the negative charges of the O atoms of the carboxylate groups in the cPPyNP structure [126]. $NaBH_4$ powder was added to mixed solution to reduce Ni^{2+} ions to Ni nanoparticles. The mixed solution was stirred vigorously to blend cPPyNP, Ni^{2+} and $NaBH_4$ uniformly. **Figure 6.3b** shows the TEM image of Ni/cPPyNP. Ni nanoparticles were decorated with *ca.* 5 nm diameters and dispersed uniformly on the surface of cPPyNP. The HR-TEM image of Ni/cPPyNP surface presents that Ni nanoparticles indicate interplanar spacings 0.20 nm, 0.23 nm and 0.204 nm for the (200), (111) and (220) of face centered cubic (FCC)-Ni in **Figure 6.3c**, respectively. It confirms growth of pure crystalline Ni nanoparticles.

The stable state of the liquid-ion-gate FET sensor is one of the critical factors in the fabrication of sensor. The immobilization of transducer materials on the sensor electrode and T13NDs on the transducer materials were achieved to improve stability of FET sensor. **Figure 6.2b** shows the schematic diagram of the sequence for the ND_Ni/cPPyNP-based FET sensor configuration. 3-aminopropyl-trimethoxysilane (APS) was treated on the sensor electrode to functionalize the substrate with amine ($-NH_2$) groups. Ni/cPPyNPs were fixed on the electrode substrate due to covalent bonding between the $-NH_2$ groups of the substrate and the carboxyl functional groups (-COOH) of the Ni/cPPyNPs. 4-(4,6-dimethoxy-1,3,5,-triazin-2-yl)-4-methylmorpholinium chloride (DMT-MM) aqueous solution was used as the involving agent for peptide bonding between Ni/cPPyNPs and electrode

substrate. After previous process, nanodisc-shaped receptor solution was treated on the surface of electrode to attach nanodisc-shaped receptors on Ni/cPPyNPs. In this process, 6xHis-tag of the receptor was worked as biomolecular glue because the 6xHis-tag generally attaches well to Ni^{2+} or Ni [60]. As a result, T13ND binds stably to Ni nanoparticles on the surface of cPPyNP like **Figure 6.1** when the ND solution was incubated on the Ni/cPPyNP immobilized sensor electrode for 2 h.

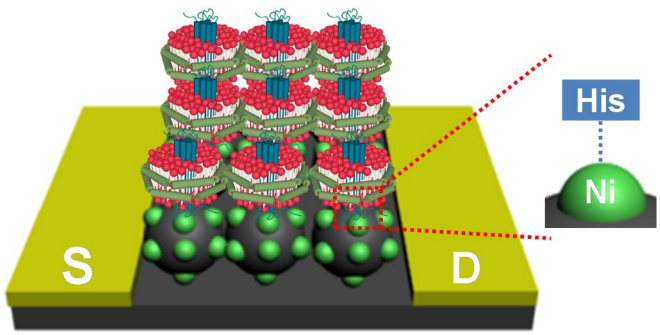

Figure 6.1 Schematic diagram of T13ND-conjugated Ni-decorated cPPyNP in FET.

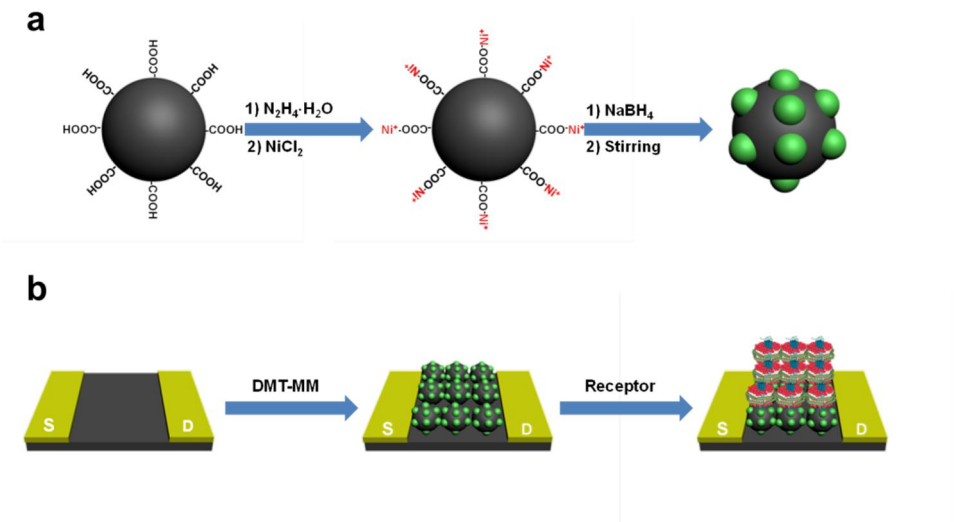

Figure 6.2 Illustrative diagram of fabrication steps of (a) Ni/cPPyNP and (b) ND-attached Ni/cPPyNPs-fixed sensor electrode for CV detection.

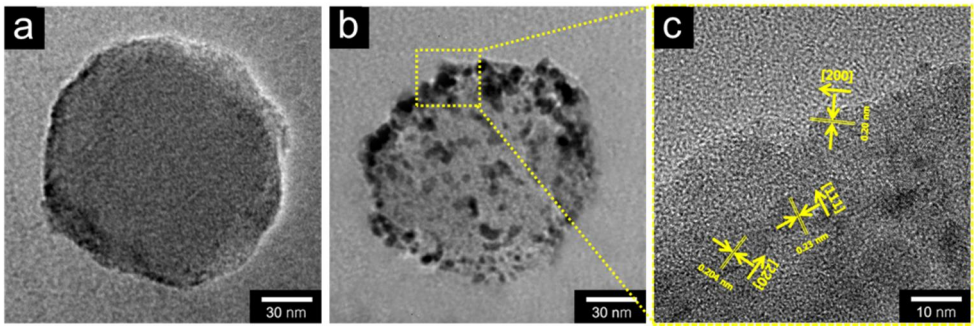

Figure 6.3 TEM images of (a) cPPyNP and (b) Ni/cPPyNP and HR-TEM image of (c) surface of Ni/cPPyNP.

6.3 Characteristics of nanodisc-conjugated Ni-decorated cPPyNP in FET

To characterize the electrical properties and stability of the ND_Ni/cPPyNPs in liquid phase, a liquid-ion-gate FET configuration was built using electrolyte (**Figure 6.4a**). Furthermore, ND-attached Ni/cPPyNP was confirmed by SEM image in **Figure 6.4a**. **Figure 6.4b** displays I_{SD}-V_{SD} plot of ND_Ni/cPPyNP electrode for variable V_G. The I_{SD} increases negatively with negatively increasing V_G, meaning p-type semiconducting behavior of transducer materials. It was caused by an increase in the oxidation level of the polymer chains. In addition, Ni/cPPyNP and Mi_Ni/cPPyNP immobilized electrode also shows similar tendency with ND_Ni/cPPyNP in **Figure 6.5a** and **b**.

Figure 6.4c exhibits the I_{SD}-V_{SD} plots of various FET electrode at V_G=0. These plots are used to estimate the electrical contact of the transducer materials on the electrode substrate. Each transducer material shows linearity, ohmic contact, for voltage range from -0.1 to 0.1V. The *dI/dV* value of Ni/cPPyNP is larger than that of cPPyNP owing to metal nanoparticles. Although the *dI/dV* values of ND_Ni/cPPyNP are decreased rather than Ni/cPPyNP, the ohmic contact is endured. The liquid-ion-gate system can achieve bigger transconductance than back-gate system because of the intimate contact between the transducers and the gate. As a result, it could be operated more effectively as an electrochemical sensor.

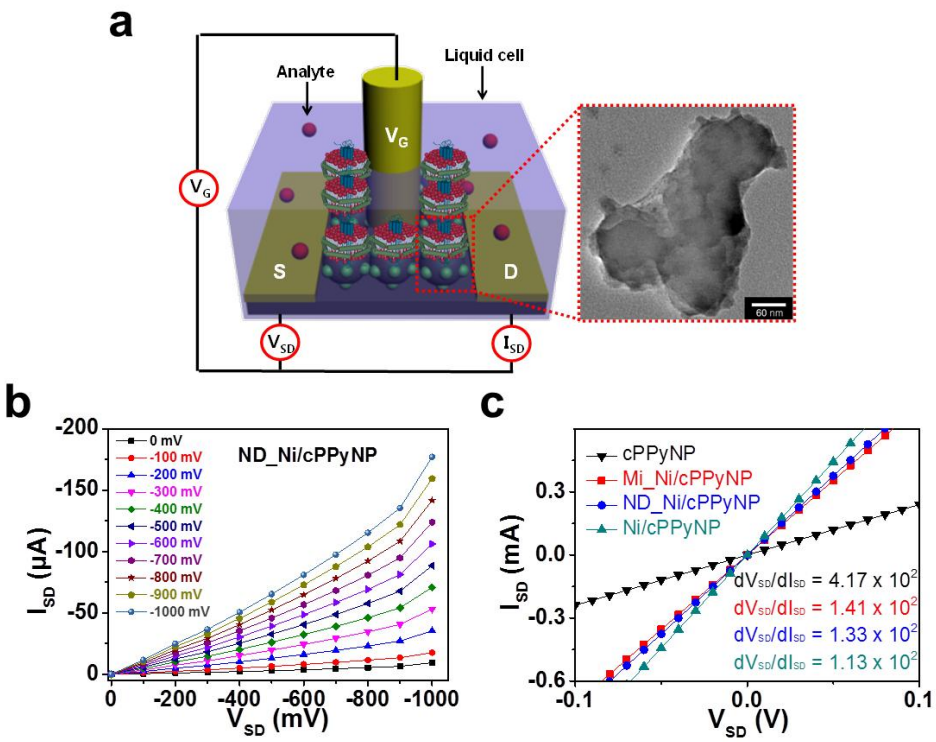

Figure 6.4 (a) Schematic diagram of the liquid-ion-gate FET sensor electrode and SEM image of nanodisc-shaped receptor adhered Ni/cPPyNP. (b) Source–drain current-voltage (I_{SD}–V_{SD}) curves of ND_Ni/cPPyNP for variable gate voltages (V_G) ranging from 0 mV to 1000 mV in 100 mV steps. (c) Source–drain current-voltage (I_{SD}–V_{SD}) curves of FETs with different transducer nanomaterials.

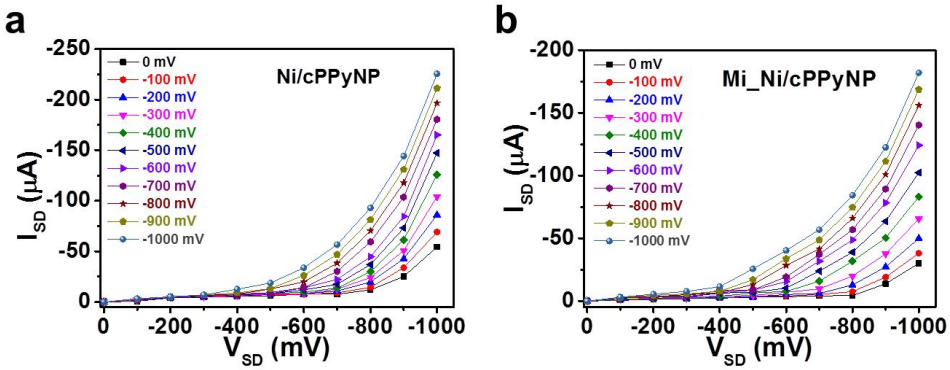

Figure 6.5 Source–drain current-voltage (I_{SD}–V_{SD}) curves of (a) Ni/cPPyNP and (b) Mi_Ni/cPPyNP FET electrodes for variable gate voltages (V_G) ranging from 0 mV to 1000 mV in 100 mV steps.

6.4 Highly stable and ultrasensitive nanodisc-based biosensor detecting the liquid and gaseous cadaverine

6.4.1 Detection of the liquid cadaverine

The real-time responses of T13ND-based biosensor to the CV and other amines were monitored. Also, TAAR13c-detergent micelles (Mi) were also tested to be compared with T13NDs in terms of performance. **Figure 6.6a** shows the real-time response of Mi- and ND-based biosensor to various concentrations of CV, respectively. Here, while adding various concentrations of target solutions, drain-source currents of the sensor using a semiconductor analyzer were measured. The measured data of current changes during the additions of CV were normalized by the original current values to estimate the normalized conductance change $\Delta I/I_0$. Note that the conductance of the biosensor was sharply increased after adding various concentrations of CV solutions. The Mi-based sensor increased conductance by CV solutions with concentration as low as 1 pM, indicating the high sensitivity of our device. *Interestingly*, the ND-based biosensor was 1000 times more sensitive than Mi-based sensor. These results clearly demonstrate that the ND was more stable and elaborate, which lead to effective charge transfer, thus the ND-based device can be ultrasensitive platform. Moreover, the limit of detection of ND-based sensor is about 100 aM which is much lower than previous study and that of tolerance of CV in various foods [12]. Therefore, this platform could be practically used to assessment of food quality. To compare the performances of the biosensing systems, the most efficient method is to estimate the K value assuming a small molecule because the Langmuir isotherm model, which is related to the equilibrium between analyte molecules and binding sites,

enables predicting their response characteristics. In previous work, *K* was founded using the adsorption and desorption of an olfactory receptor and a small analyte [51]. As a benchmark for the process, *K* is characterized as following equation:

$$N = \frac{C}{1/k + C}$$

K can be calculated from the ligand concentrations (*C*) in the solution and the normalized sensitivity (*N*), which is the same as the $\Delta I/I_0$ values in **Figure 6.6a**. Each *K* value was calculated from the dose-dependent responses and their curve shapes were similar to the curve shapes in **Figure 6.6b**. The *K* between T13NDs or Mi and CV as 6.253×10^{9} M^{-1} and 2.375×10^{10} M^{-1}, respectively. These results are a large compared with previously-reported values measured using cells or biological systems. This result implies that device can detect target CV molecules with a much higher sensitivity than cells or biological systems. Moreover, these results demonstrate that this platform could show the reproducible signals in repeated experiments.

Figure 6.6c shows the real-time responses of Mi- and ND-based biosensor to various molecules containing amine functional groups. Here, we injected PT, HA, Glu, TryA, and CV molecules to the sensor in series while measuring the sensor responses. PT has a similar structure with CV, HA is monoamine, Glu is an amino acid and TryA is derivative of tryptophan. Note that the ND-based device exhibited negligible sensor responses to non-target molecules even at a relatively high concentration of 30 μM. However, the conductance of the ONBN increased sharply by adding CV at a concentration of 1 μM, which is 30 times lower concentration than that of non-target molecular species. It seems that the Mi-based sensor slightly exhibit the nonspecific signal to PT and HA. This result clearly shows that the ND-based device can selectively detect CV at a very low concentration even in the

presence of high concentrations of similar molecular species. Also, the NDs have a higher selectivity to CV than Mi, because the ND could have more native-like environment than Mi using lipid bilayer and MSP, which lead to mimic the binding pocket of natural receptor.

To investigate the stability of receptor-based device, the stability of Mi- and ND-based sensor were also characterized by storage test during 35 days. **Figure 6.6d** shows the stability data of receptor-based devices. The Mi-based device exhibited the stability for 3 weeks, on the other hand, the ND-based device showed the high-stability for 5 weeks. This result clearly indicates the ND-based sensor is much more stable than Mi-based device. Therefore, the ND could be more practical tool for protein-based applications than detergent micelles.

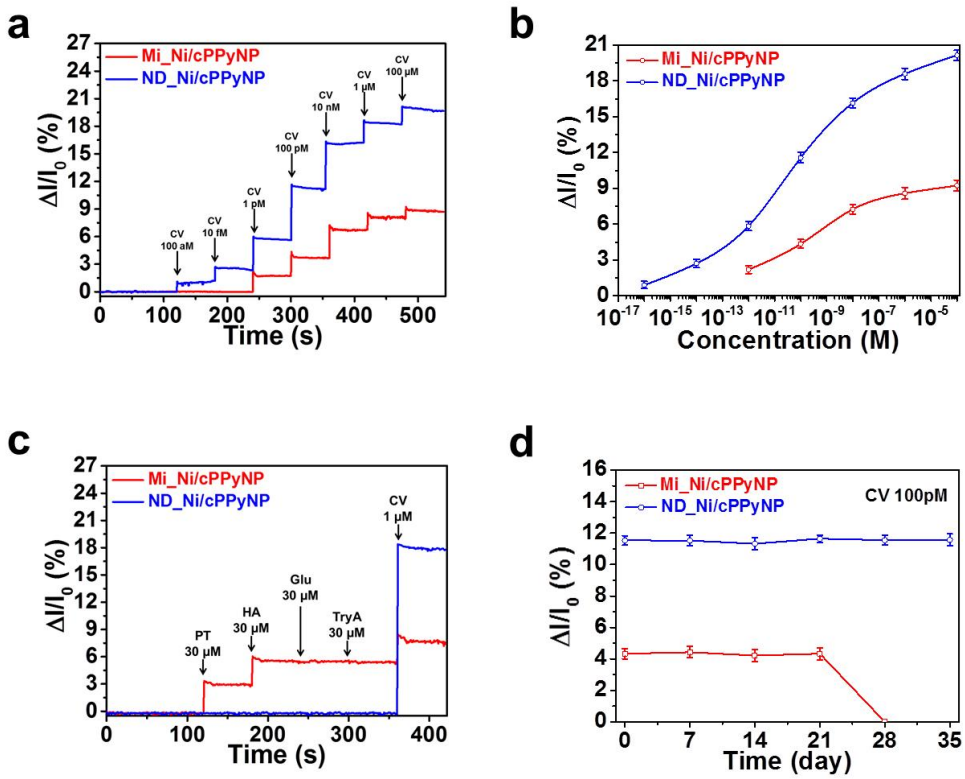

Figure 6.6 The response of Mi- and ND-based biosensor to the CV and other amines. (a) Real-time responses of the sensor (b) Normalized curves of the sensor (c) Selectivity tests of the sensors (d) Stability tests of the sensors. The stability tests were investigated by storing them in a sealed vessel at 4 ^{o}C during 35 days.

6.4.2 Detection of the gaseous cadaverine

To investigate the binding capability of Mi and ND to gaseous target, the receptor-based devices were exposed to gaseous CV. Schematic diagram of gas generation system and its measurement using the biosensor is depicted in **Figure 6.7a. Figure 6.7b** represents the real-time responses of the Mi- and ND-based sensor upon periodic exposure to CV gas. The real-time resistance difference was measured as a function of odorant concentration in a nitrogen stream to assess the sensing performance of the Mi- and ND-based biosensor. The minimum detectable level (MDL) of ND-based biosensor was *ca.* 0.01 ppb; however, the Mi-based sensor exhibited no meaningful responses to gaseous CV. In dried conditions, detergents could not form the detergent micelles, thus the secondary structure of receptor can be destroyed. On the other hand, the NDs can keep their structure in dried condition, because they are composed of lipid bilayer and MSP, which tightly wrap the receptor and support the receptor structure [13]. Thus the NDs have a great advantage in detecting the gaseous target.

The stability test of ND-based sensor for detecting the gaseous target was also performed following the liquid sensing procedures (**Figure 6.6d**). **Figure 6.7c** indicates the stability data of ND-based device with ~1 ppb CV. The ND-based sensor showed the repeatable responses to the CV over 6 weeks. This clearly indicates the ND-based sensor could be reusable for 6 weeks. These results significantly imply that the ND-based biosensor could enormous performance in stability and reusability as well as sensitivity and selectivity. Furthermore, this can effectively detect the gaseous target, which is impossible in the detergent micelle. Thus, ND-based platform can be practically used the gaseous system for the various applications, such as environmental monitoring, early diagnosis of disease and response of corpses.

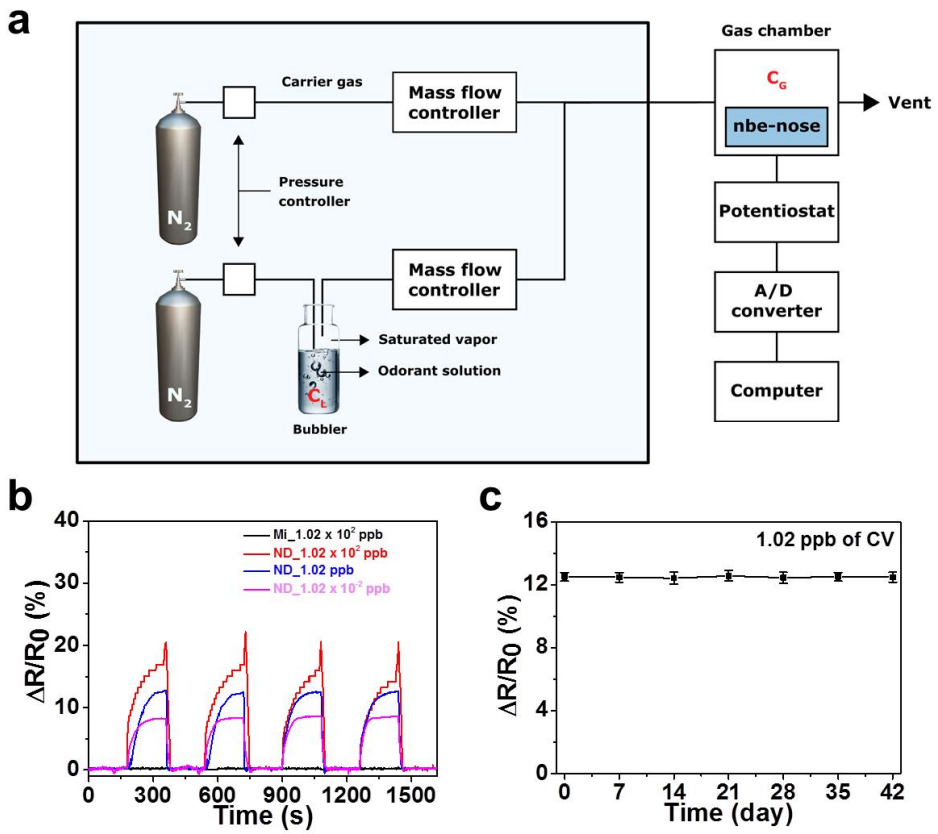

Figure 6.7 The responses of Mi- and ND-based sensor to the gaseous CV. (a) Schematic diagram of gas generation system and its measurement using the biosensor. CL and CG represent the odorant concentrations in the liquid and gas phases, respectively. The nanodisc-based bioelectronic nose (nbe-nose) could effectively detect the gaseous CV. (b) Real-time responses of Mi- and ND-based devices to the gaseous CV. (c) Stability test of ND-based biosensor to the CV for 6 weeks.

6.5 Conclusions

The T13ND-conjugated Ni-decorated cPPyNP in FET was successfully fabricated. The ND-based sensor shows high-performance than Mi-based sensor in sensitivity, selectivity and stability. The ND-based biosensor also can detect the gaseous CV with high sensitivity, stability and reusability. This study can be used as an attractive methodology for the receptor-based detection of death-associated odor CV. Moreover, ND-based platform can be practically used the gaseous system for the various applications, such as environmental monitoring and early diagnosis of disease.

Chapter 7

Production of human olfactory receptor-embedded nanodiscs for the development of human-like performance bioelectronic nose smelling a rose scent

7.1 Introduction

A rose scent is known to be a pleasant smell to humans, and it has been used as a key component to impart scents to various fragrances and flavorings [127]. Some of the well-known ingredients for a rose scent are geraniol, citronellol, phenylethyl alchol, nerol, and so on [128-130]. Rose oil products including such ingredients have often been utilized as one of the base materials for developing new perfumes, making the perfumes more complete and plentiful. [131,132] However, the overdose of such rose scent ingredients can cause bad smells and even allergic reactions to humans. Thus, the quantitative evaluation of rose scent ingredients in real samples such as rose oil can be an important issue and has been extensively studied in various areas such as cosmetic and pharmaceutical industries [133,134]. However, most of methods allow one to measure only specific well-known substances, and they cannot be used to measure how humans would respond to some new substances. Furthermore, they often exhibited a rather low selectivity compared with a human nose.

In humans and mammals, an olfactory system enables the discrimination of specific chemical components from other non-specific components, which has been critical in evaluating food qualities and recognizing dangers in various environments [135,136]. In an olfactory system, olfactory receptor (OR) proteins recognize and bind only to specific odorant molecules, enabling the identification of specific smells [137]. For example, the main ingredients of a rose scent, geraniol and citronellol, could specifically bind to human olfactory receptor 1A2 (hOR1A2) with different characteristics [131,138,139]. Such selective binding characteristics of ORs have been utilized to develop bioelectronic nose sensors with human-like responses [72,137]. For example, versatile bioelectronic noses have been

developed by hybridizing ORs onto electric channels based on various nanostructures such as CNTs, conducting polymer nanotubes, and graphenes [73,74]. However, it is often difficult to achieve the stable immobilization of ORs on such nanostructured material surfaces, degrading the stability and sensitivity of the bioelectronic nose devices based on them [118,53]. Furthermore, bioelectronic nose devices to detect general rose scent ingredients have not been developed yet.

Herein, a strategy to smell and quantitatively evaluate general rose scent ingredients just like human sensory systems *via* ND-based bioelectronic nose devices was reported. In this strategy, hOR1A2 was expressed from *E. coli* and reconstituted using ND. The hOR1A2-embedded NDs (hOR1A2NDs) were successfully incorporated on Au-based floating electrodes over a CNT-FET, and the binding of target rose scent molecules onto the NDs was monitored using the underlying CNT-FET. This method allowed us to identify and quantitatively monitor *geraniol* and *citronellol*, well-known rose odorants, down to *1 fM* and *10 fM*, respectively. This method can also be used to discriminate a specific rose odorant from other odorants just like a human olfactory system. Furthermore, the effect of scent enhancer materials on the responses of ORs could be quantitatively evaluated and found that the addition of 1 nM benzyl salicylate could enhance the response by $\sim 10^3$ times . Importantly, the method enabled the quantitative evaluation of rose odorants in real samples like rose oil, providing the results similar to those measured via conventional methods. Since this method allows one to quantitatively evaluate general ingredients providing a rose scent even in real samples, it should be a powerful tool for versatile basic research and industrial applications such as the screening of new rose scent ingredients and the quantitative evaluation of base materials for fragrances.

7.2 Structure of a bioelectronic nose comprised of hOR1A2-based nanodiscs and a floating electrode-based CNT-FET

Figure 7.1 shows a schematic diagram representing a bioelectronic nose which was fabricated *via* the hybridization of hOR1A2NDs and a CNT-based transducer with floating electrodes. The detailed experimental procedure is described in the Methods section and **Figure 7.2**. In brief, hOR1A2 was overexpressed in *E. coli* and purified via affinity chromatography. Then, the purified hOR1A2 was wrapped with lipids and MSP for the construction of hOR1A2-based NDs. The prepared hOR1A2NDs were selectively immobilized on the flat gold (Au)-based floating electrodes of the CNT-FET [112]. Here, the gold floating electrodes were first functionalized with thiol groups, and then half-V5 antibody (Ab) fragments as linker molecules were immobilized onto the gold floating electrodes via disulfide bonding. Lastly, the hOR1A2NDs were immobilized on the floating electrodes. When specific rose odorants bind to the hOR1A2 on the floating electrode, the conductance of the CNT-FET channel was changed, which allowed us to monitor rose scent ingredients in real time. In this fabrication strategy, receptor molecules stabilized in ND structures were directly immobilized on a flat Au-based floating electrode surface using well-known reliable chemical processes, which should simplify the chemical procedures and may enhance the reliability of the devices compared with previous CNT channel-based sensor devices [53,140]. Furthermore, the high sensitivity of floating electrode-based transducers as reported previously were used as a great advantage [115,109]. Finally, since the hOR1A2 molecules bind selectively to general rose odorant molecules like a human nose, thus sensors can be expected to smell a rose scent just like humans.

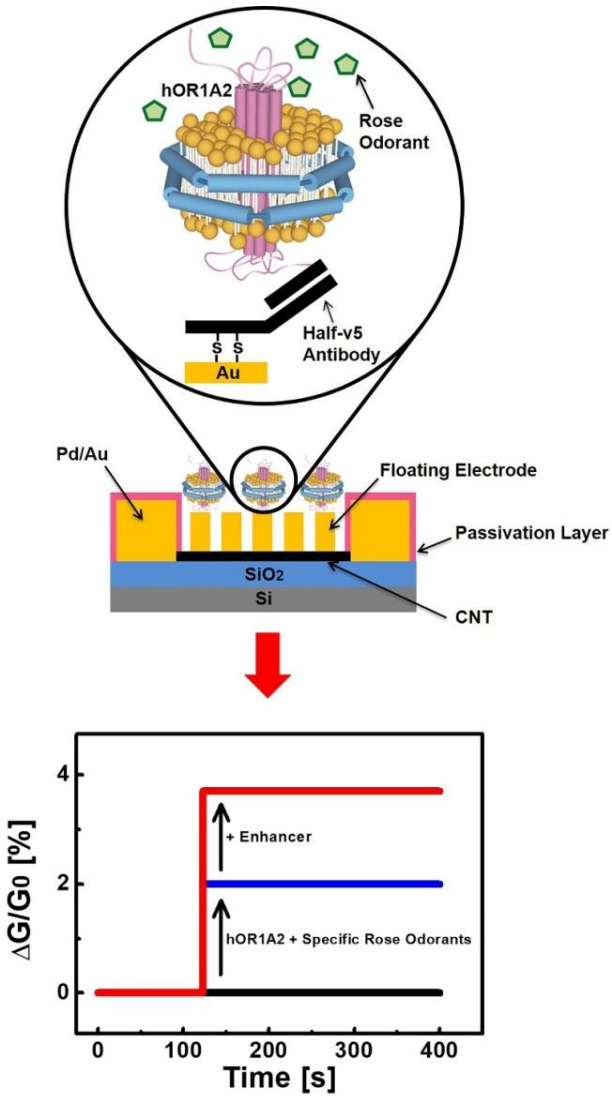

Figure 7.1 Schematic diagram depicting a bioelectronic nose based on the hybridization of hOR1A2NDs and floating electrodes and the simplified responses of the bioelectronic nose by application of rose odorants. The hOR1A2NDs were immobilized on the gold floating electrodes of the CNT-FET using half-V5 Ab fragments and thiol groups. The bioelectronic nose could respond to general rose ingredients, and the responses could be enhanced by the enhancer.

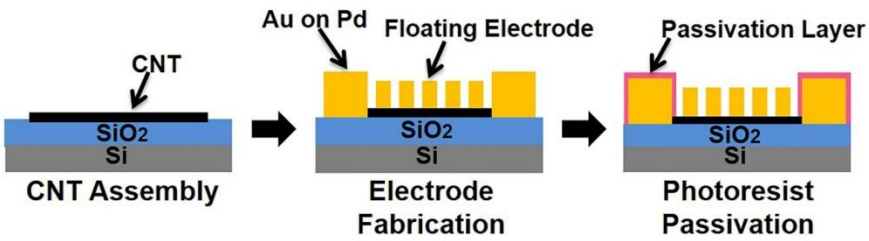

Figure 7.2 Schematic diagram depicting the fabrication processes of a CNT-FET with floating electrodes. First, CNTs were selectively assembled on a SiO_2 substrate. Following the CNT assembly method, source, drain, and floating electrodes were fabricated using photolithography and thermal evaporation. Finally, a passivation layer was formed on the source and drain electrodes.

7.3 Characterization of hOR1A2 expressed in HEK-293 cells

The cell-based assays were performed to evaluate the ligand/receptor binding activity of hOR1A2 in cells and to compare it with its responses in the bioelectronic nose devices [141]. **Figure 7.3a** shows the dose-dependent responses of hOR1A2 expressed in human embryonic kidney (HEK)-293 cells to geraniol and citronellol. In brief, hOR1A2 and luciferase gene were first transfected in the HEK-293 cells. When the binding of the specific odorants to hOR1A2 in the transfected cells occurred, the conformation of hOR1A2 was changed and signal transduction was initiated. A cyclic adenosine monophosphate (cAMP) pathway in the cells was sequentially activated. The activated cAMP pathway stimulated cAMP response element-binding protein (CREB), which resulted in the expression of luciferase gene [110]. A luminescence intensity in the cells was measured using a Dual-Glo luciferase assay system after the introduction of geraniol and citronellol. The normalized luminescence intensity was calculated by normalizing the responses of hOR1A2 to each rose odorant with respect to a positive control (forskolin, FSK) in HEK-293 cells (see Methods section). The HEK-293 cells expressing hOR1A2 exhibited luminescence intensities to *geraniol* and *citronellol* from the concentrations of $1\ \mu M$ and $10\ \mu M$, respectively. The dissociation constants (K_d) of hOR1A2 to *geraniol* and *citronellol* were calculated as $3.24 \times 10^{-6}\ M$ and $1.45 \times 10^{-5}\ M$, respectively. These constant values are quite similar to those in other studies using mammalian cell-based systems [142,143]. These results clearly show that that functional hOR1A2 was well expressed in the HEK-293 cells, while maintaining its functionality. Also, the receptors in the cells exhibited larger responses to geraniol than citronellol, presumably due to the higher affinity of hOR1A2 to geraniol than citronellol.

Figure 7.3b shows the responses of hOR1A2 in HEK-293 cells to various kinds of odorants. The responses of hOR1A2 in the HEK-293 cells to different odorants of 100 μM concentrations were measured by the luciferase assay system in a similar way to that in Figure 2a (see Methods section). Phenyl ethanol, linalool, and damascone have pleasant floral odors. They are often used to make an artificial rose scent with geraniol and citronellol. Geranyl chloride and geranyl formate have different functional groups from geraniol. Octadiene and dimethyl octanol have different numbers of carbon atoms and carbon-carbon double bonds compared with geraniol, respectively. The HEK-293 cells expressing hOR1A2 stimulated by geraniol and citronellol resulted in much higher luminescence intensities compared to those stimulated by other odorants. These results show that hOR1A2 discriminates the specific rose odorants from other odorants with a high selectivity, indicating that hOR1A2 was well expressed and retained its functionality in the cells.

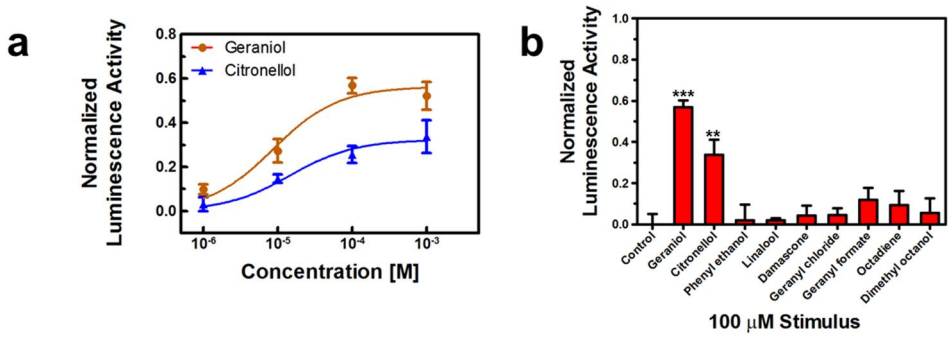

Figure 7.3 Characterization of hOR1A2 expressed in HEK-293 cells. (a) Dose-dependent responses of hOR1A2 expressed in HEK-293 cells upon the addition of geraniol and citronellol. The HEK-293 cells expressing hOR1A2 exhibited luminescence activities to geraniol and citronellol with different characteristics (n=5). (b) Specificity of hOR1A2 to geraniol and citronellol among various odorants. Only the stimulation of geraniol and citronellol caused responses in the HEK-293 cells expressing hOR1A2 ($^{**}p<0.01$, $^{***}p<0.001$) (n=5).

7.4 Reconstitution of hOR1A2 into nanodiscs

For the development of bioelectronic nose smelling a rose scent, the hOR1A2 were expressed in *E. coli,* purified and functionally reconstructed [7,17]. **Figure 7.4a** shows the sodium dodecyl sulfate polyacrylamide gel electrophoresis (SDS-PAGE) gel staining image (left) and western blot analysis (right) of purified hOR1A2 expressed in *E. coli*. For the formation of high-quality receptor proteins, hOR1A2 was overexpressed in *E. coli*, solubilized and purified with affinity chromatography. The purification and expression of hOR1A2 in *E. coli* were confirmed by a SDS-PAGE method and western blot analysis. The detailed experimental procedure is described in the Methods section. The bands of 34 kDa, which are in accord with the molecular weight of hOR1A2, were clearly observed. These results indicate that hOR1A2 was expressed in *E. coli* and purified with a high level. It should be pointed out that it has been very difficult to express and purify G protein-coupled receptors (GPCRs) in heterologous cells, especially in *E. coli* due to their complicate structures and hydrophobicity. Such a difficultly has been a stumbling block holding back the practical applications of OR-based biosensor devices [10,5]. Considering that the successful expression of hOR1A2 in *E. coli* has not been reported before, the results can be a breakthrough and should provide new opportunities for biosensors and other applications requiring a large amount of high-quality OR proteins responding to a rose scent.

To achieve a stable OR functionality on the bioelectronic nose devices, hOR1A2 was embedded in ND structures. First, MSP1E3D1, which is MSP derived from apolipoprotein A-I in humans, was produced and purified to wrap lipid/receptor complexes. **Figure 7.4b** shows the SDS-PAGE gel staining image (left) and western blot analysis (right) of purified MSP1E3D1. The expression and purification of MSP1E3D1 were confirmed in a similar way to that in **Figure 7.4a**.

The thick bands around 26 kDa were clearly observed. The bands correspond to the molecular weight of MSP1E3D1. These indicate that MSP1E3D1 was overexpressed, successfully produced as a soluble form, and purified with high purity. Because it has been reported that MSP1E3D1 can be overexpressed in *E. coli* and its overexpression allows it to effectively wrap lipid/receptor complexes [144], the results imply that MSP1E3D1 was successfully overexpressed to construct stable ND structures for the development of bioelectronic devices. To construct hOR1A2-embedded NDs, the purified MSP1E3D1 was added to the mixture of hOR1A2 and lipids. Then, the detergent molecules of the mixture were removed with Bio-beads. The purified hOR1A2NDs were finally obtained by size exclusion chromatography (SEC). To confirm the size distribution of the constructed hOR1A2NDs, a dynamic light scattering (DLS) analysis were performed (**Figure 7.4c**). The hOR1A2NDs had uniform diameters from 15 nm to 20 nm with a quite narrow size distribution. The size distribution of hOR1A2NDs is also close to that of NDs containing other GPCRs in previous studies [16,99]. This implies that hOR1A2NDs can be successfully constructed as monomeric receptor forms and can be utilized as an ideal sensor unit.

Figure 7.4d is the field emission scanning electron microscopy (FE-SEM) image of hOR1A2NDs immobilized on a gold surface. For the FE-SEM imaging, the hOR1A2NDs immobilized on the gold surface were lyophilized using a freeze dryer. Then, the surface was coated with 5 nm thick platinum using a sputtering system. The hOR1A2NDs ranged in diameter from 15 nm to 20 nm, which is similar to that in Figure 2e. This clearly shows that hOR1A2NDs were successfully constructed with optimized sizes and could be immobilized uniformly on gold surfaces.

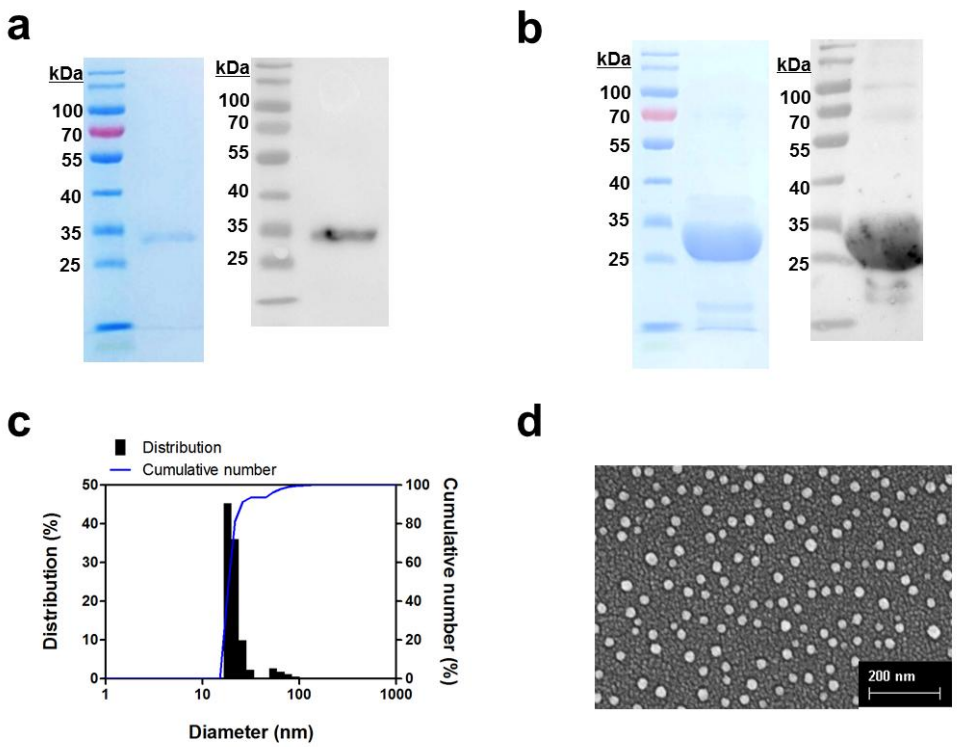

Figure 7.4 Characterization of hOR1A2NDs. (a) SDS-PAGE gel staining image and western blot analysis of purified hOR1A2 expressed in *E. coli*. The western blot analysis was performed using an anti-V5 epitope Ab. The band of 34 kDa indicates the molecular weight of hOR1A2. (b) SDS-PAGE gel staining image and western blot analysis of purified MSP1E3D1 expressed in *E. coli*. The western blot analysis was performed using an anti-His- probe mouse Ab. The band at the molecular weight of MSP1E3D1 about 26 kDa was observed. (c) Size distribution analysis of hOR1A2NDs. (d) FE-SEM image of hOR1A2NDs immobilized on a gold substrate.

7.5 Electrical characterization of bioelectronic noses and its responses to geraniol and citronellol

Figure 7.5a shows the liquid gate profiles of a CNT-FET with floating electrodes before and after the immobilization of hOR1A2NDs. Source-drain currents were measured at a gate bias voltage ranging from -0.4 V to 0.4 V with a source-drain bias voltage of 0.1 V. The source-drain currents decreased significantly as the applied gate voltage increased, indicating the typical p-type semiconducting behavior of the CNT-FET device. Note that the conductance of the CNT-FET channel decreased after the immobilization of hOR1A2NDs, which could be attributed to the negatively charged C-terminuses of the NDs immobilized on the floating electrodes [145]. The negatively-charged NDs reduced the CNT-FET channel conductance via the modulation of the Schottky barriers between the CNT networks and the floating electrodes. Also, it should be mentioned that the gating effect of the CNT-FET device was maintained even after the immobilization of hOR1A2NDs, indicating that it can be suitable for sensor applications [146].

Figure 7.5b shows the typical real-time response of a bioelectronic nose with hOR1A2NDs to the varying concentrations of geraniol in aqueous environments. Here, the source-drain currents were monitored during the addition of geraniol solutions with different concentrations while maintaining a 0.1 V source-drain bias voltage. In this sensor device, a relative CNT-FET channel conductance change $\Delta G/G_0$ was used as a sensor signal, where ΔG and G_0 are the *conductance change* and *original conductance* of the CNT-FET, respectively. The addition of geraniol solutions caused immediate increase in the conductance of the CNT-FET with hOR1A2NDs in a dose-dependent manner, while a bare CNT-FET without hOR1A2NDs did not exhibited a conductance change even after the addition of

geraniol (**Figure 7.5c**). A similar selective response was obtained when citronellol was applied to CNT-FET devices *with* or *without* hOR1A2NDs (**Figure 5d and e**). The result clearly shows that the sensor responses came from the specific binding between the rose odorants and hOR1A2. Such a specific response can be attributed to the change of electrical charges in the hOR1A2 caused by the selective binding of rose odorant molecules as discussed previously [72]. In brief, the specific binding of rose odorant molecules to hOR1A2 caused the conformational change of the receptor, resulting in the change of electrical charges in it [72]. Subsequently, the changed charge state of the receptor molecule would result in the increase of the CNT-FET channel conductance via the modulation of Schottky barriers between the CNT network channel and floating electrodes [115]. This result shows that this method can allow us to detect specific rose odorants in real-time with a high sensitivity.

Figure 7.6a shows the normalized sensor signals of the bioelectronic noses at the different concentrations of geraniol and citronellol. The normalized signals were calculated by normalizing sensor signals with respect to their maximum sensor signal values at high concentration conditions [64]. The sensing measurement at a single concentration was carried out repeatedly using four or more bioelectronic nose devices to obtain average values and standard deviations. The result shows the response curves similar to other bioelectronic nose devices reported previously [146]. In the case of geraniol, the bioelectronic noses began to show responses from the concentration of 1 fM, and the responses were almost saturated at around 1 μM. For citronellol, the bioelectronic noses exhibited the responses from the concentration of 10 fM. These results indicate that the bioelectronic noses could detect the rose scent odorants with a high sensitivity, and discriminate one rose scent odorant from the other odorant.

The dose-dependent responses of the bioelectronic noses can be analyzed further by fitting the experimental data using a model based on a Hill equation as reported previously [64]. If it is assumed that binding events between target odorant molecules (geraniol and citronellol) and receptors (hOR1A2) follow the Hill equation model, the density C_s of the odorant molecules bound to the receptors in the NDs can be written as

$$C_s = \frac{C_{s\_max} \cdot C^n}{(1/K)^n + C^n} \quad (1)$$

where C and K are *the odorant concentration in a solution* and *the equilibrium constant for the binding of the odorants to hOR1A2*, respectively. The C_{s_max} and n are *the density of hOR1A2 on the floating electrodes* and *a Hill coefficient*, respectively. Assuming a conductance change ΔG is linearly-proportional to the number of bound odorant molecules, the sensor signal $\left|\Delta G/G_0\right|$ can be approximated as $\left|\Delta G/G_0\right| \sim kC_s$, where k is a constant signifying the response characteristics of the bioelectronic nose [64,109]. When C becomes very large, the sensor signal $\left|\Delta G/G_0\right|$ converges to the value of kC_{s_max}. Thus, a normalized signal N could be written like

$$\mathrm{N} = \frac{C^n}{(1/K)^n + C^n} \quad (2)$$

By fitting the experimental data using Eq 2, the equilibrium constants of *geraniol* and *citronellol* to hOR1A2 could be estimated as $8.37 \times 10^{11}\ M^{-1}$ and $2.60 \times 10^{6}\ M^{-1}$, respectively. Note that the equilibrium constant of geraniol was found ~10^5 times larger than that of citronellol. The results imply that geraniol could be a more potent rose scent than citronellol, which is consistent with the result using cells in **Figure 7.3a**. However, the results show that the bioelectronic noses responded to much lower concentrations of geraniol and citronellol than the case of the cell-

based assays in **Figure 7.3a**. Presumably, it is because the device could directly measure the conformation of receptor proteins without any intermediate biological steps, while, the cell assays relied on complicated signal transduction steps based on multiple biological processes caused by the binding of odorant molecules to receptors [147,148]. The intermediate steps in the cell assays require several different materials other than rose odorants to generate the sensing signals, which could have resulted in much lower sensitivity than the bioelectronic nose [10]. Similar trends were also reported in case of other bioelectronic devices [109,64]. Since this method is based on these bioelectronic noses, it can be utilized for versatile applications such as the development of new fragrances.

Figure 7.6b shows the real-time responses of a bioelectronic nose to various odorants. *Trimethylamine* (TMA) and *amyl butyrate* (AB) are odorants generated from *spoiled seafood* and *reminiscent of an apricot*, respectively. The introduction of geraniol and citronellol solutions of 10 pM concentrations caused significant increase in the CNT-FET channel conductance, while the introduction of TMA and AB with the same concentrations induced negligible changes. This result indicates that the bioelectronic nose could discriminate rose scent odorants from other odorants with a high selectivity.

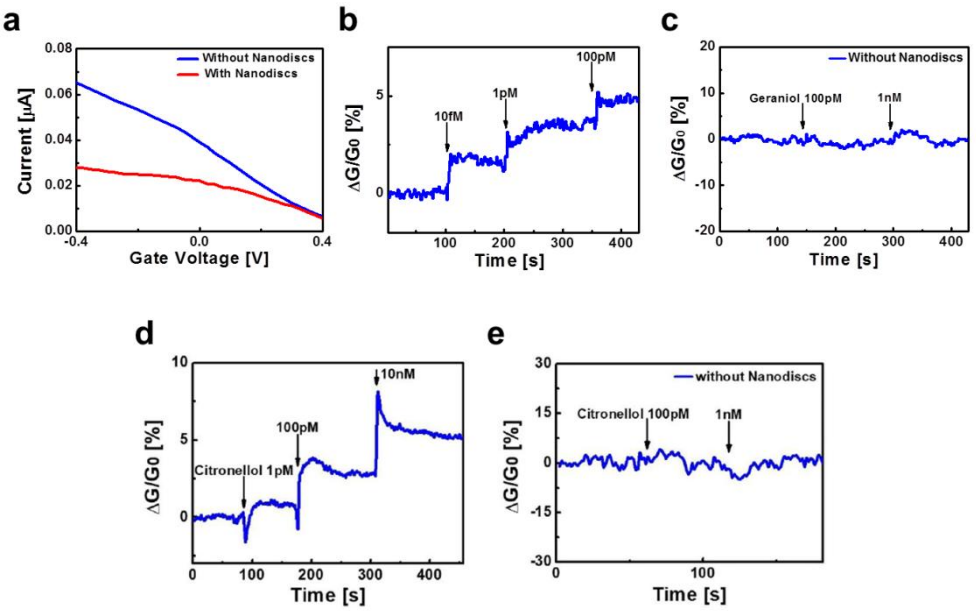

Figure 7.5 Electrical measurement data of bioelectronic noses based on the hybridization of hOR1A2NDs and floating electrode-based CNT-FETs. (a) Liquid gate profiles of a CNT-FET with floating electrodes before and after the immobilization of hOR1A2NDs. (b) Real-time responses of a bioelectronic nose to various concentrations of geraniol. The introduction of geraniol occurred sharp increase in the CNT-FET channel conductance. (c) Real-time responses of a bare CNT-FET without hOR1A2NDs to the various concentrations of geraniol. The addition of geraniol did not affect the conductance change of the bare CNT-FET. (d) Real-time responses to the different concentrations of citronellol. (e) Real-time responses of a bare CNT-FET to the various concentrations of citronellol.

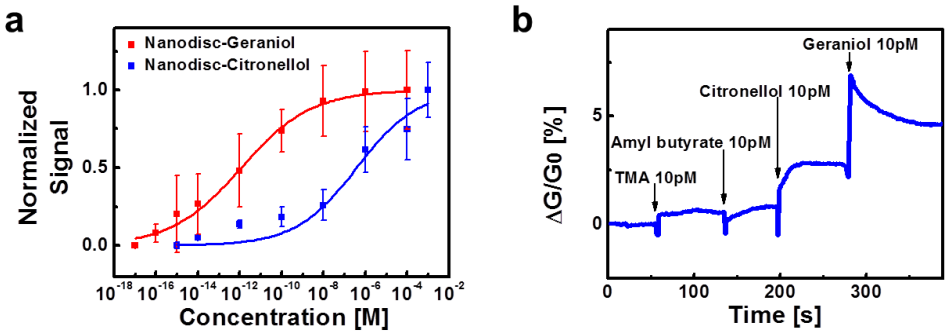

Figure 7.6 Dose-dependent and selective responses of the bioelectronic noses to geraniol and citronellol. (c) Dose-dependent responses of the bioelectronic noses to geraniol and citronellol. The sensing measurement was carried out repeatedly four or more times using bioelectronic noses for a quantitative analysis. The equilibrium constants of geraniol and citronellol to hOR1A2 were estimated as 8.37×10^{11} M^{-1} and 2.60×10^{6} M^{-1}, respectively. (d) Real-time responses of a bioelectronic nose to the different kinds of odorants. The addition of geraniol and citronellol of 10 pM concentrations caused significant increase in the CNT-FET channel conductance, while the addition of TMA and AB of 10 pM concentrations resulted in negligible changes in the CNT-FET channel conductance.

7.6 Measuring the effect of the enhancer on the assessment of rose scent ingredients

Previous works show that enhancer materials such as benzyl salicylate could enforce the richness and depth of floral compositions [149]. However, the effect of such enhancers has not been evaluated quantitatively before. Here, cell-based assays were performed to investigate whether the enhancer affects the responses of hOR1A2 in cells. **Figure 7.7a** is the cell assay results showing the responses of hOR1A2 to geraniol with or without the enhancer, benzyl salicylate. In brief, HEK-293 cells expressing hOR1A2 were stimulated with the various concentrations of geraniol in benzyl salicylate. In the presence of 0.1 μM benzyl salicylate, the responses of hOR1A2 to *1*, *10* and *100 μM* geraniol were found to be enhanced by *1.63-fold, 1.76-fold and 1.48-fold* compared with those without the enhancer, respectively. Likewise, benzyl salicylate with a 1 μM concentration led to *2.14-fold*, *2.09-fold* and *1.52-fold* enhancement in the responses of hOR1A2 to *1*, *10* and *100 μM* geraniol, respectively. In addition, benzyl salicylate alone did not stimulate hOR1A2. These results imply that benzyl salicylate could enhance the responses of ORs to their floral scent molecules and thus enables low detection thresholds to them. To the best of knowledge, this result is the first demonstration that benzyl salicylate could highly boost the responses of the cells expressing ORs to the specific odorant.

The effect of the enhancer on the assessment of geraniol was also investigated using the bioelectronic noses. **Figure 7.7b** shows the normalized signals of the bioelectronic noses to geraniol in the presence and absence of 1 nM benzyl salicylate. First, the mixture of geraniol and benzyl salicylate was prepared, holding the concentration of benzyl salicylate at 1 nM and varying the

concentrations of geraniol from 10 aM to 10 nM. Each data point was obtained by multiple measurements using four or more bioelectronic nose devices. Note that the normalized signal curve in the presence of benzyl salicylate was shifted to lower concentration regions, indicating that the bioelectronic noses began to exhibit responses at much lower concentrations of geraniol than the cases without the enhancer. It is also confirmed that benzyl salicylate alone did not respond to a CNT-FET with floating electrodes (**Figure 7.8**). Following the model based on the Hill equation as described above, the equilibrium constants between hOR1A2 and geraniol with or without benzyl salicylate could be estimated. In the presence of 1nM benzyl salicylate, the equilibrium constant between hOR1A2 and geraniol was estimated to be 1.64×10^{15} M^{-1}, while that without the enhancer was 8.37×10^{11} M^{-1} as shown in **Figure 7.6a**. These results clearly show that benzyl salicylate contributes significantly to the enhancement of the hOR1A2 responses to geraniol and thus decreases the thresholds of binding between hOR1A2 and geraniol. This is the first report showing that benzyl salicylate as the enhancer could affect the binding affinity of the receptor on bioelectronic devices. It also should be noted that since this method directly measured the responses of receptors without relying on complicated signal pathways like cell assays, it can be a powerful method to quantitatively evaluate the effect of enhancer materials on the binding of rose odorant molecules to receptors. Such a capability of the method should open up versatile applications in various areas such as drug, food, and cosmetic industries.

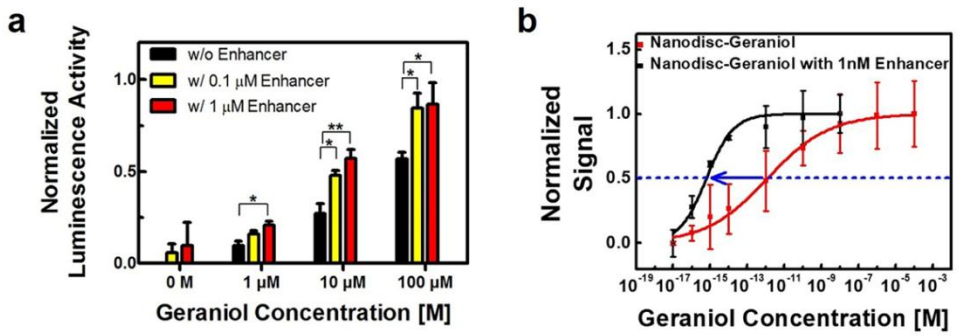

Figure 7.7 Effect of benzyl salicylate as the enhancer on the assessment of geraniol by utilizing hOR1A2-expressed HEK-293 cells and bioelectronic noses. (a) Normalized luminescence activities of hOR1A2 to geraniol and benzyl salicylate in HEK-293 cells. The HEK-293 cells expressing hOR1A2 were activated by geraniol with or without the varying concentrations of benzyl salicylate (0, 0.1, 1 μM). The responses of hOR1A2 to geraniol were enhanced by benzyl salicylate ($^{*}p<0.05$, $^{**}p<0.01$) (n=5). (b) Normalized signals of bioelectronic noses at the various concentrations of geraniol in the presence and absence of 1 nM benzyl salicylate. The sensing experiments were repeated with four or more bioelectronic noses for each data point. The equilibrium constant between hOR1A2 and geraniol in the absence of benzyl salicylate was estimated as 8.37×10^{11} M^{-1}. In the presence of benzyl salicylate, the estimated equilibrium constant between hOR1A2 and geraniol was found 1.64×10^{15} M^{-1}.

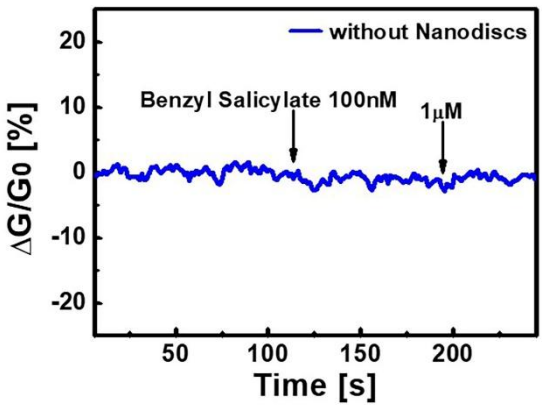

Figure 7.8 Real time responses of a bare CNT-FET without hOR1A2NDs to the varying concentrations of benzyl salicylate. The introduction of benzyl salicylate did not cause the CNT-FET channel conductance change.

7.7 Smelling rose scent ingredients in natural rose oil

Rose oil products extracted from roses have been utilized as base materials for versatile applications such as perfumes [150,151]. In this case, the quantitative evaluation of rose scent ingredients in the oil can be important because the overdose of the ingredients may result in bad smells [152]. To demonstrate the validity of the method for practical applications, experiments were performed to quantitatively evaluate rose scent ingredients in natural rose oil by utilizing the method. **Figure 7.9a** shows the responses of a bioelectronic nose to the different concentrations of the rose oil in real-time. The rose oil solutions were prepared by means of dilution of a natural rose oil stock solution with HEPES buffer II (see Methods section). The diluted rose oil solutions were consecutively applied to the bioelectronic nose while monitoring its responses. The rose oil diluted by $1/10^{11}$ caused negligible responses in the conductance of the bioelectronic nose. However, those diluted by $1/10^{10}$ and $1/10^{9}$ led to significant increase in the CNT-FET channel conductance. This result clearly shows that the bioelectronic nose could detect the specific rose compounds in real samples such as real rose oil.

Figure 7.9b shows the normalized signal of bioelectronic noses to the natural rose oil diluted for different concentrations. The rose oil stock solution was serially diluted with HEPES buffer II to prepare rose oil solutions diluted from $1/10^{11}$ to $1/10^{5}$. The detailed experimental procedure is described in the Methods section. The normalized signal of bioelectronic noses to the diluted rose oil solutions was obtained by fitting the response data in the same way as shown in **Figure 7.6a**. The measurements were repeated for four or more bioelectronic noses to obtain quantitative results. Since the bioelectronic noses detect general species which bind to hOR1A2, this strategy can efficiently evaluate general ingredients giving a rose scent. It is assumed that the geraniol could be more dominant to hOR1A2 than

citronellol by the results of **Figure 7.3a** and **Figure 7.6a**. That is, hOR1A2 of the bioelectronic nose responds to geraniol mainly. This indicates that geraniol could play a dominant role in the responses of bioelectronic noses to the natural rose oil [153,1]. Then, the concentration of geraniol in the undiluted rose oil solution could be estimated by comparing $K_{rose\ oil}$ with $K_{geraniol}$, where $K_{rose\ oil}$ and $K_{geraniol}$ are the dissociation constants of hOR1A2 to the diluted rose oil and geraniol, respectively. The $K_{rose\ oil}$ was found 1.62×10^{-9} from the normalized signal of bioelectronic noses to the diluted rose oil solutions. Likewise, the $K_{geraniol}$ was found 1.19×10^{-12} M from the section of **Figure 7.6a**. On the basis of comparison of $K_{rose\ oil}$ to $K_{geraniol}$, the concentration of geraniol in the undiluted rose oil could be estimated as about 7.35×10^{-4} M. This value is quite close to the geraniol concentration estimated by a gas chromatography mass spectrometry (GC-MS) method (**Figure 7.10**). The concentration of geraniol in the undiluted rose oil was estimated as 9.47×10^{-4} M by the GC-MS analysis. This means that the binding affinity of hOR1A2 with geraniol could be slightly underestimated in complicated environments containing various chemicals which could lead to lower effective concentration of geraniol to the receptor [44]. This result clearly shows that the bioelectronic noses could recognize geraniol in complex environments such as real rose oil. Also, this result indicates that the bioelectronic nose could be utilized for practical applications, which could open up various applications such as a stable and reliable sensor platform.

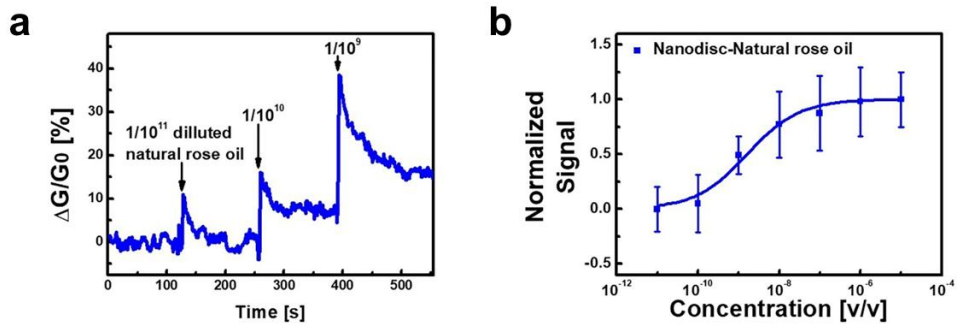

Figure 7.9 Responses of bioelectronic noses to natural rose oil. (a) Real-time responses of a bioelectronic nose to the different concentrations of natural rose oil. The introduction of the rose oil solution diluted by $1/10^{11}$ occurred negligible responses in the conductance of the bioelectronic nose. The rose oil solutions diluted by $1/10^{10}$ and $1/10^{9}$ caused significant increase in the CNT-FET channel conductance. (b) Normalized signal of bioelectronic noses to the natural rose oil solutions diluted from $1/10^{11}$ to $1/10^{5}$. The x-axis (v/v) represents the volume/volume percent of the natural rose oil in the HEPES buffer solution. The sensing measurement was conducted using four or more bioelectronic noses to obtain quantitative results. The concentration of geraniol in the undiluted rose oil was estimated as 7.35×10^{-4} M.

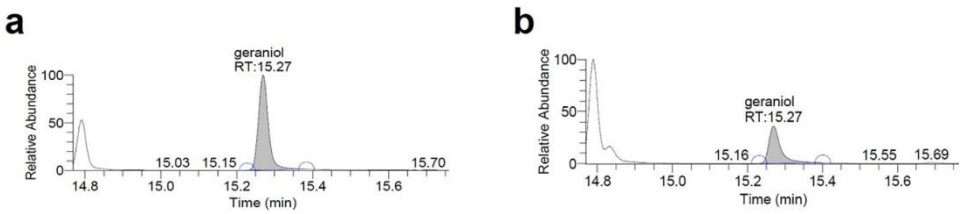

Figure 7.10 GC-MS chromatogram of geraniol of an authentic reference and natural rose oil. (a) GC-MS chromatogram of geraniol of an authentic reference compound. Geraniol of the authentic reference compound has a peak at retention time 15.27 min. (b) GC-MS chromatogram of geraniol in natural rose oil. Geraniol in the natural rose oil has also a peak at retention time 15.27 min. The concentration of geraniol in the undiluted natural rose oil was found 9.47×10^{-4} M.

7.8 Conclusions

A method to quantitatively smell and evaluate rose scent ingredients *via* ND-based bioelectronic nose was successfully developed. In this method, hOR1A2NDs were directly immobilized on the gold floating electrodes of a CNT-FET, and the binding events between hOR1A2NDs and specific rose scent components were monitored electrically by the underlying CNT-FET. Using this method, this platform could quantitatively recognize geraniol and citronellol down to 1 fM and 10 fM, respectively. Additionally, the method allowed us to distinguish a specific rose odorant from other odorants with a high selectivity. Most noticeable, it is investigated the effect of the scent enhancer on the responses of ORs to a rose scent and found that the responses could be enhanced by ~10^3 times in the presence of 1 nM benzyl salicylate. Furthermore, the method facilitated the quantitative detection of rose odorants in real rose oil just like a human nose. These results clearly show that the strategy could be a simple but powerful impetus for basic research and various applications in perfume and cosmetic industries.

Chapter 8

Overall discussion and further suggestions

Overall discussion and further suggestions

GPCRs composed of seven transmembrane domains have been considered to be very important, because they are significantly involved in a large number of diverse process and many human diseases, and 40% of all drug targets. For this reason, many researches of GPCR have been reported, which can provide a wide view of GPCR-related study, such as structural analysis, prediction of their function and development of drug. Also, GPCR-based platform, especially, highly purified and well-reconstituted receptor-conjugated platform, can be a useful tool for the development of a practical biosensor that can be applied to various applications, such as scientific investigation, diagnosis of diseases and fragrance development. Significant efforts have been made to develop the receptor-based bioelectronic sensor; nevertheless, they remain as a challenge because of their complicated structure and hydrophobicity.

The *E. coli* has been widely used as a host cell to produce the recombinant proteins, because of its great advantage in low cost, simplicitiy, convenience, and high productivity. However, the production of membrane proteins in *E. coli*, especially GPCR, remains a challenge because of their strong hydrophobicity, a complicated charge distribution and membrane inserting mechanism of bacterial cells.

The produced GPCR should be purified for receptor-based accurate researches, and reconstituted with hydrophobic environment because of their strong hydrophobicity. Also, the functional reconstitution technique of GPCRs has been considered to be important tool for more stable and accurate receptor-based research. These techniques have been studied to acquire basic knowledge of the crystal structure, receptor-signaling and pharmacological research. Moreover, many

studies have suggested that highly purified and well-reconstituted receptor with biomimetic environments could have native-like receptor structure and binding pocket. Also, the high-quality GPCRs can be used as a powerful tool for qualitative and quantitative biophysical information on receptor/ligand binding details and could be applied to bioelectronic sensor, which is used to various fields, such as assessment of food quality, disease diagnosis, response of disaster and drug-interaction researches.

In chapter 4, the approach for studying receptor agonism and antagonism was proposed by combining the roles of FETs and GPCRs in a DRD1-conjugated FET system, which is a suitable substitute for conventional cell-based receptor assays. The DRD1 was reconstituted and purified to mimic native binding pockets that have highly discriminative interactions with DRD1 agonists/antagonists. The real-time responses from the DRD1-nanohybrid FET were highly sensitive and selective for dopamine agonists/antagonists, and their maximal response levels were clearly different depending on their DRD1 affinities. Moreover, the *K* were estimated by fitting the response levels. Each *K* value indicates the variation in the affinity between DRD1 and the agonists/antagonists; a greater *K* value corresponds to a stronger DRD1 affinity in agonism, whereas a lower *K* value in antagonism indicates a stronger DA-blocking effect.

In chapter 5, the receptor-embedded NDs was assembled and their size was optimized with various conditons. Also, the function of NDs was compared with the receptor in HEK-293 cell. As a results, the receptor in NDs can effectively mimics the binding pocket of natural receptor. Also, an oriented ND-functionalized bioelectronic nose (ONBN), based on carbon nanotube transistors and NDs embedded with an OR produced in *E. coli,* was developed for detection of CV. To fabricate ONBN devices, a TAAR13c binding to CV was produced in *E. coli*,

purified, reconstituted into NDs and assembled, in the desired orientation, onto CNT-based field effect transistor with floating electrodes. The ONBN showed high performance in terms of sensitivity and selectivity. Moreover, the ONBN was used to measure CV in diverse real-food samples for the determination of food freshness. These results indicate ONBN devices can be utilized to evaluate the quality of food samples quantitatively, which should enable versatile practical applications such as food safety and preservative development. Moreover, the ONBN could provide a useful tool for detection of corpses, which could be practically used in disaster responses.

In chapter 6, the ND-based high-performance biosensor was developed for the detection of liquid and gaseous target. The T13NDs was successfully constructed and the T13ND-conjugated Ni-decorated cPPyNP in FET were successfully assembled to detect the liquid and gaseous CV. The T13NDs could mimic the native-like binding pocket of natural receptor and exist with high-stability in the aqueous and dried conditions. The Ni-decorated cPPyNP could enhance the sensor sensitivity and enable to the oriented immobilization of NDs on the FET. As a result, the ND-based biosensor can have a high-stability and reliability as well as a high-sensitivity and selectivity. Moreover, they also can detect the gaseous CV with high sensitivity, stability and reusability. Furthermore, this platform detects the CV in the real-samples by the extent of corruption. This study can be used as an attractive methodology for the receptor-based detection of liquid and gaseous target.

In chapter 7, a strategy to quantitatively smell general rose scent ingredients just like a human olfactory system was reported by utilizing a ND-based bioelectronic nose. In this strategy, hOR1A2-embedded NDs were immobilized on the gold-based floating electrodes of a CNT-FET. The hOR1A2NDs responded to rose scent

molecules specifically, which were monitored electrically using the underlying CNT-FET. This strategy allowed us to quantitatively assess the contents of geraniol and citronellol, the main components of a rose scent, as low as 1 fM and 10 fM, respectively. In addition, it enabled us to selectively discriminate a specific rose odorant from other odorants. Significantly, we also demonstrated that the responses of hOR1A2NDs to a rose scent could be strongly enhanced by enhancer materials like a human nose. Furthermore, the method provided a means to quantitatively evaluate rose scent components in real samples such as rose oil. Since our method allows one to quantitatively evaluate general rose scent ingredients just like a human nose, it could be a powerful strategy for versatile basic research and various applications such as fragrance development.

In this thesis, the expression of GPCR in *E. coli*, solubilization and purification of the receptor, functional reconstitution receptor using detergent micelles and NDs and their applications to the high-performance biosensor were developed. The DR, TAAR and hOR were successfully produced, purified and reconstituted. Also, they were applied to a biosensor, which lead to practical application. Especially, the NDs embedded with GPCR produced in *E. coli* can have a native-like binding pocket, which leads it to mimic the response of a natural receptor. In addition, the receptor-based biosensor, especially ND-based platform, shows the high-performance in sensitivity, selectivity, reliability and stability. Also, the ND-based platform can detect the gaseous target molecule as well as the target of aqueous condition. This work represents significant progress in nano-bio technology toward a practical bioelectronic sensor. Moreover, this study can be used an advanced method for purification and functional reconstitution of GPCRs produced in *E. coli*. Furthermore, this could offer the receptor-based approaches including quality control of food, basic research on GPCR, drug discovery and disease diagnosis.

Bibliography

1. Firestein S (2001) How the olfactory system makes sense of scents. Nature 413: 211-218

2. Bockaert J, Claeysen S, Becamel C et al (2002) G protein-coupled receptors: dominant players in cell-cell communication. Int. Rev. Cytol. 212: 63-132

3. Terstappen GC, Reggiani A (2001) In silico research in drug discovery. Trends Pharmacol. Sci. 22: 23-26

4. Serebryany E, Zhu GA, Yan EC (2012) Artificial membrane-like environments for *in vitro* studies of purified G-protein coupled receptors. Biochim. Biophys. Acta 1818: 225-233

5. Kaiser L, Graveland-Bikker J, Steuerwald D et al (2008) Efficient cell-free production of olfactory receptors: detergent optimization, structure, and ligand binding analyses. Proc. Natl. Acad. Sci. U. S. A. 105: 15726-15731

6. Michalke K, Huyghe C, Lichiere J et al (2010) Mammalian G protein-coupled receptor expression in *Escherichia coli*: II. Refolding and biophysical characterization of mouse cannabinoid receptor 1 and human parathyroid hormone receptor 1. Anal. Biochem. 401: 74-80

7. Yang H, Song H, Ahn S et al (2015) Purification and functional reconstitution of human olfactory receptor expressed in *Escherichia coli*. Biotechnol. Bioproc. E. 20: 423-430

8. Kiefer H, Krieger J, Olszewski JD et al (1996) Expression of an olfactory receptor in *Escherichia coli*: purification, reconstitution, and ligand binding. Biochemistry 35: 16077-16084

9. Park CS, Lee C, Kwon OS (2016) Conducting polymer based nanobiosensors. Polymers 8: 249

10. Park SJ, Yang H, Lee SH et al (2017) Dopamine receptor D1 agonism and antagonism using a field-effect transistor assay. ACS Nano 11: 5950-5959

11. Rosano GL, Ceccarelli EA (2014) Recombinant protein expression in *Escherichia coli*: advances and challenges. Front. Microbiol. 5: 172

12. Yang H, Kim D, Kim J et al (2017) Nanodisc-based bioelectronic nose using olfactory receptor produced in *Escherichia coli* for the assessment of the death-associated odor cadaverine. ACS Nano 11: 11755-12864

13. Denisov IG, Sligar SG (2017) Nanodiscs in membrane biochemistry and biophysics. Chem. Rev. 117: 4669-4713

14. Goldsmith BR, Mitala JJ, Josue J et al (2011) Biomimetic chemical sensors using nanoelectronic readout of olfactory receptor proteins. ACS Nano 5: 5408-5416

15. Ritchie T, Grinkova Y, Bayburt T et al (2009) Chapter eleven-reconstitution of membrane proteins in phospholipid bilayer nanodiscs. Methods Enzymol. 464: 211-231

16. Denisov IG, Sligar SG (2016) Nanodiscs for structural and functional studies of membrane proteins. Nat. Struct. Mol. Biol. 23: 481-486

17. Son M, Kim D, Ko HJ et al (2017) A portable and multiplexed bioelectronic sensor using human olfactory and taste receptors. Biosens. Bioelectron. 87: 901-907

18. Ahn SR, An JH, Song HS et al (2016) Duplex bioelectronic tongue for sensing umami and sweet tastes based on human taste receptor nanovesicles. ACS Nano 10: 7287-7296

19. Lim JH, Park J, Oh EH et al (2014) Nanovesicle-based bioelectronic nose for the diagnosis of lung cancer from human blood. Adv. Healthc. Mater. 3: 360-366

20. Rosenbaum DM, Rasmussen SG, Kobilka BK (2009) The structure and function of G-protein-coupled receptors. Nature 459: 356-363

21. Kobilka B, Schertler GF (2008) New G-protein-coupled receptor crystal structures: insights and limitations. Trends Pharmacol. Sci. 29: 79-83

22. Bridges TM, Lindsley CW (2008) G-protein-coupled receptors: from classical modes of modulation to allosteric mechanisms. ACS Chem. Biol. 3: 530-541

23. Rasmussen SG, Choi HJ, Rosenbaum DM et al (2007) Crystal structure of the human β2 adrenergic G-protein-coupled receptor. Nature 450: 383-387

24. Scheerer P, Park JH, Hildebrand PW et al (2008) Crystal structure of opsin in its G-protein-interacting conformation. Nature 455: 497-502

25. Venkatakrishnan AJ, Deupi X, Lebon G et al (2013) Molecular signatures of G-protein-coupled receptors. Nature 494: 185-194

26. Mancia F, Hendrickson WA (2007) Expression of recombinant G-protein coupled receptors for structural biology. Mol. BioSyst. 3: 723-734

27. Sarramegna V, Muller I, Mousseau G et al (2005) Solubilization, purification, and mass spectrometry analysis of the human mu-opioid receptor expressed in Pichia pastoris. Protein Expression Purif. 43: 85-93

28. Lundstrom K, Wagner R, Reinhart C et al (2006) Structural genomics on membrane proteins: comparison of more than 100 GPCRs in 3 expression systems. J. Struct. Funct. Genomics 7: 77-91

29. Michalke K, Graviere ME, Huyghe C et al (2009) Mammalian G-protein-coupled receptor expression in *Escherichia coli*: I. High-throughput large-scale production as inclusion bodies. Anal. Biochem. 386: 147-155

30. Song HS, Lee SH, Oh EH et al (2009) Expression, solubilization and purification of a human olfactory receptor from *Escherichia coli*. Curr. Microbiol. 59: 309-314

31. Grisshammer R (2009) Purification of recombinant G-protein-coupled receptors. Methods Enzymol. 463: 631-645

32. Chiu ML, Tsang C, Grihalde N et al (2008) Over-expression, solubilization, and purification of G protein-coupled receptors for structural biology. Comb. Chem. High Throughput Screening 11: 439-462

33. Seddon AM, Curnow P, Booth PJ (2004) Membrane proteins, lipids and detergents: not just a soap opera. Biochim. Biophys. Acta 1666: 105-117

34. Rigaud J-L, Mosser G, Lacapere J-J et al (1997) Bio-Beads: an efficient strategy for two-dimensional crystallization of membrane proteins. J. Struct. Biol. 118: 226-235

35. Franke R, Sakmar T, Graham R et al (1992) Structure and function in rhodopsin. Studies of the interaction between the rhodopsin cytoplasmic domain and transducin. J. Biol. Chem. 267: 14767-14774

36. Brown MF (1994) Modulation of rhodopsin function by properties of the membrane bilayer. Chem. Phys. Lipids 73: 159-180

37. Li J, Edwards PC, Burghammer M et al (2004) Structure of bovine rhodopsin in a trigonal crystal form. J. Mol. Biol. 343: 1409-1438

38. Milligan G (2007) G protein-coupled receptor dimerisation: molecular basis and relevance to function. Biochim. Biophys. Acta 1768: 825-835

39. Prinster SC, Hague C, Hall RA (2005) Heterodimerization of g protein-coupled receptors: specificity and functional significance. Pharmacol. Rev. 57: 289-298

40. Schwendener RA (2014) Liposomes as vaccine delivery systems: a review of the recent advances. Ther. Adv. Vaccines 2: 159-182

41. Mao D, Wallace B (1984) Differential light scattering and absorption flattening optical effects are minimal in the circular dichroism spectra of small unilamellar vesicles. Biochemistry 23: 2667-2673

42. Oh EH, Lee SH, Ko HJ et al (2014) Odorant detection using liposome containing olfactory receptor in the SPR system. Sens. Actuators, B 198: 188-193

43. Johnson ZL, Lee S-Y (2015) Chapter seventeen-liposome reconstitution and transport assay for recombinant transporters. Methods Enzymol. 556: 373-383

44. Parmar MJ, Lousa CDM, Muench SP et al (2016) Artificial membranes for membrane protein purification, functionality and structure studies. Biochem. Soc. Trans. 44: 877-882

45. Kucharska I, Seelheim P, Edrington T et al (2015) OprG harnesses the dynamics of its extracellular loops to transport small amino acids across the outer membrane of Pseudomonas aeruginosa. Structure 23: 2234-2245

46. Vestergaard M, Kraft JF, Vosegaard T et al (2015) Bicelles and other membrane mimics: comparison of structure, properties, and dynamics from MD simulations. J. Phys. Chem. B 119: 15831-15843

47. Glover KJ, Whiles JA, Wu G et al (2001) Structural evaluation of phospholipid bicelles for solution-state studies of membrane-associated biomolecules. Biophys. J. 81: 2163-2171

48. McKibbin C, Farmer NA, Jeans C et al (2007) Opsin stability and folding: modulation by phospholipid bicelles. J. Mol. Biol. 374: 1319-1332

49. Prosser RS, Evanics F, Kitevski JL et al (2006) Current applications of bicelles in NMR studies of membrane-associated amphiphiles and proteins. Biochemistry 45: 8453-8465

50. Wang L, Xie J, Schultz PG (2006) Expanding the genetic code. Annu. Rev. Biophys. Biomol. Struct. 35: 225-249

51. Kwon OS, Ahn SR, Park SJ et al (2012) Ultrasensitive and selective recognition of peptide hormone using close-packed arrays of hPTHR-conjugated polymer nanoparticles. ACS Nano 6: 5549-5558

52. Lee SH, Sung JH, Park TH (2012) Nanomaterial-based biosensor as an emerging tool for biomedical applications. Ann. Biomed. Eng. 40: 1384-1397

53. Kim TH, Lee SH, Lee J et al (2009) Single-carbon-atomic-resolution detection of odorant molecules using a human olfactory receptor-based bioelectronic nose. Adv. Mater. 21: 91-94

54. Park CS, Yoon H, Kwon OS (2016) Graphene-based nanoelectronic biosensors. J. Ind. Eng. Chem. 38: 13-22

55. Liu SF, Petty AR, Sazama GT et al (2015) Single-walled carbon nanotube/metalloporphyrin composites for the chemiresistive detection of amines and meat spoilage. Angew. Chem. Int. Ed. Engl. 54: 6554-6557

56. Ko HJ, Park TH (2006) Dual signal transduction mediated by a single type of olfactory receptor expressed in a heterologous system. Biol. Chem. 387: 59-68

57. Bleicher KH, Green LG, Martin RE et al (2004) Ligand identification for G-protein-coupled receptors: a lead generation perspective. Curr. Opin. Chem. Biol. 8: 287-296

58. Lee M, Im J, Lee B et al (2006) Linker-free directed assembly of high-performance integrated devices based on nanotubes and nanowires. Nat. Nanotechnol. 1: 66-71

59. Bogue R (2009) Nanosensors: a review of recent research. Sensor Review 29: 310-315

60. Lo YS, Nam DH, So HM et al (2009) Oriented immobilization of antibody fragments on Ni-decorated single-walled carbon nanotube devices. ACS Nano 3: 3649-3655

61. Son M, Lee JY, Ko HJ et al (2017) Bioelectronic nose: An emerging tool for odor standardization. Trends Biotechnol. 35: 301-307

62. Bachtold A, Hadley P, Nakanishi T et al (2001) Logic circuits with carbon nanotube transistors. Science 294: 1317-1320

63. Cui Y, Lauhon LJ, Gudiksen MS et al (2001) Diameter-controlled synthesis of single-crystal silicon nanowires. Appl. Phys. Lett. 78: 2214-2216

64. Song HS, Jin HJ, Ahn SR et al (2014) Bioelectronic tongue using heterodimeric human taste receptor for the discrimination of sweeteners with human-like performance. ACS Nano 8: 9781-9789

65. Hong JY, Yoon H, Jang J (2010) Kinetic study of the formation of polypyrrole nanoparticles in water-soluble polymer/metal cation systems: A light-scattering analysis. Small 6: 679-686

66. Gilman AG (1987) G proteins: transducers of receptor-generated signals. Annu. Rev. Biochem. 56: 615-649

67. Simon MI, Strathmann MP, Gautam N (1991) Diversity of G proteins in signal transduction. Science 252: 802-808

68. Milligan G (2004) G protein-coupled receptor dimerization: function and ligand pharmacology. Mol. Pharmacol. 66: 1-7

69. Chalmers DT, Behan DP (2002) The use of constitutively active GPCRs in drug discovery and functional genomics. Nat. Rev. Drug. Discov. 1: 599-608

70. Drews J (2000) Drug discovery: a historical perspective. Science 287: 1960-1964

71. Siehler S (2008) Cell-based assays in GPCR drug discovery. Biotechnol. J. 3: 471-483

72. Kwon OS, Song HS, Park SJ et al (2015) An ultrasensitive, selective, multiplexed superbioelectronic nose that mimics the human sense of smell. Nano lett. 15: 6559-6567

73. Park SJ, Kwon OS, Lee SH et al (2012) Ultrasensitive flexible graphene based field-effect transistor (FET)-type bioelectronic nose. Nano Lett. 12: 5082-5090

74. Yoon H, Lee SH, Kwon OS et al (2009) Polypyrrole nanotubes conjugated with human olfactory receptors: high-performance transducers for FET-type bioelectronic noses. Angew. Chem. Int. Ed. Engl. 48: 2755-2758

75. Sarramegn V, Muller I, Milon A et al (2006) Recombinant G protein-coupled receptors from expression to renaturation: a challenge towards structure. Cell Mol. Life Sci. 63: 1149-1164

76. Park SJ, Song HS, Kwon OS et al (2014) Human dopamine receptor nanovesicles for gate-potential modulators in high-performance field-effect transistor biosensors. Sci. Rep. 4: 4342

77. Clark D, White FJ (1987) D1 dopamine receptor—the search for a function: a critical evaluation of the D1/D2 dopamine receptor classification and its functional implications. Synapse 1: 347-388

78. Kim J-H, Auerbach JM, Rodríguez-Gómez JA et al (2002) Dopamine neurons derived from embryonic stem cells function in an animal model of Parkinson's disease. Nature 418: 50-56

79. Hyman BT, Van Hoesen GW, Damasio AR et al (1984) Alzheimer's disease: cell-specific pathology isolates the hippocampal formation. Science 225: 1168-1171

80. Swerdlow NR, Koob GF (1987) Dopamine, schizophrenia, mania, and depression: toward a unified hypothesis of cortico-striatopallido-thalamic function. J. Behav. Brain Sci. 10: 197-208

81. Khroyan TV, Barrett-Larimore RL, Rowlett JK et al (2000) Dopamine D1- and D2-like receptor mechanisms in relapse to cocaine-seeking behavior: effects of selective antagonists and agonists. J. Pharmacol. Exp. Ther. 294: 680-687

82. Crow TJ, Gillbe C (1973) Dopamine antagonism and antischizophrenic potency of neuroleptic drugs. Nat. New Biol. 245: 27-28

83. Creese I, Burt DR, Snyder SH (1976) Dopamine receptor binding predicts clinical and pharmacological potencies of antischizophrenic drugs. Science 192: 481-483

84. Kwon OS, Lee SH, Park SJ et al (2013) Large-scale graphene micropattern nano-biohybrids: high-performance transducers for FET-type flexible fluidic HIV immunoassays. Adv. Mater. 25: 4177-4185

85. Park SJ, Lee SH, Yang H et al (2016) Human dopamine receptor-conjugated multidimensional conducting polymer nanofiber membrane for dopamine detection. ACS Appl. Mater. Interfaces 8: 28897-28903

86. Park SJ, Kwon OS, Jang J (2013) A high-performance hydrogen gas sensor using ultrathin polypyrrole-coated CNT nanohybrids. Chem. Commun. 49: 4673-4675

87. Gasteiger E, Gattiker A, Hoogland C et al (2003) ExPASy: the proteomics server for in-depth protein knowledge and analysis. Nucleic Acids Res. 31: 3784-3788

88. Lee SH, Kwon OS, Song HS et al (2012) Mimicking the human smell sensing mechanism with an artificial nose platform. Biomaterials 33: 1722-1729

89. Yu P, Yang Z, Jones JE et al (2004) D 1 dopamine receptor signaling involves caveolin-2 in HEK-293 cells. Kidney Int. 66: 2167-2180

90. Chen K, Obinata H, Izumi T (2010) Detection of G protein-coupled receptor-mediated cellular response involved in cytoskeletal rearrangement using surface plasmon resonance. Biosens. Bioelectron. 25: 1675-1680

91. Warne T, Moukhametzianov R, Baker JG et al (2011) The structural basis for agonist and partial agonist action on a [bgr] 1-adrenergic receptor. Nature 469: 241-244

92. Bergman J, Spealman R, Madras B et al (1996) Agonist efficacy and the behavioral effects of dopamine D1 receptor ligands: drug interaction studies in squirrel monkeys. J. Pharmacol. Exp. Ther. 276: 942-950

93. Rosell DR, Zaluda LC, McClure MM et al (2015) Effects of the D1 dopamine receptor agonist dihydrexidine (DAR-0100A) on working memory in schizotypal personality disorder. Neuropsychopharmacology 40: 446-453

94. Hopkins AL, Groom CR (2002) The druggable genome. Nat. Rev. Drug. Discov. 1: 727-730

95. Criswell HE, Mueller RA, Breese GR (1992) Pharmacologic evaluation of SCH-39166, A-69024, NO-0756, and SCH-23390 in neonatal-6-OHDA-lesioned rats. Further evidence that self-mutilatory behavior induced by L-dopa is related to D1 dopamine receptors. Neuropsychopharmacology 7: 95-103

96. Millan MJ, Newman-Tancredi A, Quentric Y et al (2001) The “selective” dopamine D [sub 1] receptor antagonist, SCH23390, is a potent and high efficacy agonist at cloned human serotonin [sub 2C] receptors. Psychopharmacology 156: 58-62

97. Terry P, Katz JL (1994) A comparison of the effects of the D1 receptor antagonists SCH 23390 and SCH 39166 on suppression of feeding behavior by the D1 agonist SKF38393. Psychopharmacology 113: 328-333

98. Schetz JA, Kim O-J, Sibley DR (2003) Pharmacological Characterization of Mammalian D1 and D2 Dopamine Receptors Expressed in Drosophila Schneider-2 Cells. J. Recept. Signal Transduction 23: 99-109

99. Whorton MR, Jastrzebska B, Park PS et al (2008) Efficient coupling of transducin to monomeric rhodopsin in a phospholipid bilayer. J. Biol. Chem. 283: 4387-4394

100. Hussain A, Saraiva LR, Ferrero DM et al (2013) High-affinity olfactory receptor for the death-associated odor cadaverine. Proc. Natl. Acad. Sci. U. S. A. 110: 19579-19584

101. Liberles SD (2009) Trace amine-associated receptors are olfactory receptors in vertebrates. Ann. N. Y. Acad. Sci. 1170: 168-172

102. Sharma K, Ahuja G, Hussain A et al (2016) Elimination of a ligand gating site generates a supersensitive olfactory receptor. Sci. Rep. 6: 28359

103. Liberles SD, Buck LB (2006) A second class of chemosensory receptors in the olfactory epithelium. Nature 442: 645-650

104. Liberles SD (2015) Trace amine-associated receptors: ligands, neural circuits, and behaviors. Curr. Opin. Neurobiol. 34: 1-7

105. Grisshammer R, Tate CG (1995) Overexpression of integral membrane proteins for structural studies. Q. Rev. Biophys. 28: 315-422

106. Gafvelin G, von Heijne G (1994) Topological “frustration” in multispanning *E. coli* inner membrane proteins. Cell 77: 401-412

107. Glück JM, Koenig BW, Willbold D (2011) Nanodiscs allow the use of integral membrane proteins as analytes in surface plasmon resonance studies. Anal. Biochem. 408: 46-52

108. Lee J, Lee H, Kim T et al (2012) Floating electrode transistor based on purified semiconducting carbon nanotubes for high source-drain voltage operation. Nanotechnology 23: 85204

109. Lee M, Jung JW, Kim D et al (2015) Discrimination of umami tastants using floating electrode-based bioelectronic tongue mimicking insect taste systems. ACS Nano 9: 11728-11736

110. Zhuang H, Matsunami H (2008) Evaluating cell-surface expression and measuring activation of mammalian odorant receptors in heterologous cells. Nat. Protoc. 3: 1402

111. Imura T, Tsukui Y, Taira T et al (2014) Surfactant-like properties of an amphiphilic α-helical peptide leading to lipid nanodisc formation. Langmuir 30: 4752-4759

112. Karyakin AA, Presnova GV, Rubtsova MY et al (2000) Oriented immobilization of antibodies onto the gold surfaces via their native thiol groups. Anal. Chem. 72: 3805-3811

113. Oh J, Yoo G, Chang YW et al (2013) A carbon nanotube metal semiconductor field effect transistor-based biosensor for detection of amyloid-beta in human serum. Biosens. Bioelectron. 50: 345-350

114. Rauscher-Gabernig E, Gabernig R, Brueller W et al (2012) Dietary exposure assessment of putrescine and cadaverine and derivation of tolerable levels in selected foods consumed in Austria. Eur. Food Res. Technol. 235: 209-220

115. Kim B, Lee J, Namgung S et al (2012) DNA sensors based on CNT-FET with floating electrodes. Sens. Actuators, B 169: 182-187

116. Kim TH, Song HS, Jin HJ et al (2011) "Bioelectronic super-taster" device based on taste receptor-carbon nanotube hybrid structures. Lab Chip 11: 2262-2267

117. Takagi S, Toko K, Wada K et al (2001) Quantification of suppression of bitterness using an electronic tongue. J. Pharm. Sci. 90: 2042-2048

118. Jin HJ, Lee SH, Kim TH et al (2012) Nanovesicle-based bioelectronic nose platform mimicking human olfactory signal transduction. Biosens. Bioelectron. 35: 335-341

119. Patnaik P, Dean JA (2004) Dean's analytical chemistry handbook. McGraw-Hill, New York

120. Pipek P, Rohlík B-A, Potůček T et al (2012) The composition of pork lard as a raw material in meat production. Maso International 2: 115-119

121. Pinel JP, Gorzalka BB, Ladak F (1981) Cadaverine and putrescine initiate the burial of dead conspecifics by rats. Physiol. Behav. 27: 819-824

122. Liu CHJ, Lu WC (2007) Optical amine sensor based on metallophthalocyanine. J. Chin. Inst. Chem. Eng. 38: 483-488

123. Pacquit A, Lau KT, McLaughlin H et al (2006) Development of a volatile amine sensor for the monitoring of fish spoilage. Talanta 69: 515-520

124. Ko S, Jang J (2007) Controlled amine functionalization on conducting polypyrrole nanotubes as effective transducers for volatile acetic acid. Biomacromolecules 8: 182-187

125. Hong J-Y, Yoon H, Jang J (2010) Kinetic study of the formation of polypyrrole nanoparticles in water-soluble polymer/metal cation systems: A light-scattering analysis. Small 6: 679-686

126. Qiu L, Liu B, Peng Y et al (2011) Fabrication of ionic liquid-functionalized polypyrrole nanotubes decorated with platinum nanoparticles and their electrocatalytic oxidation of methanol. Chem. Comm. 47: 2934-2936

127. Guterman I, Shalit M, Menda N et al (2002) Rose scent: Genomics approach to discovering novel floral fragrance-related genes. Plant Cell 14: 2325-2338

128. Babu KGD, Singh B, Joshi VP et al (2002) Essential oil composition of Damask rose (Rosa damascena Mill.) distilled under different pressures and temperatures. Flavour Frag. J. 17: 136-140

129. Katsukawa M, Nakata R, Koeji S et al (2011) Citronellol and geraniol, components of rose oil, activate peroxisome proliferator-activated receptor alpha and gamma and suppress cyclooxygenase-2 expression. Biosci. Biotech. Bioch. 75: 1010-1012

130. Verma RS, Padalia RC, Chauhan A et al (2011) Volatile constituents of essential oil and rose water of damask rose (Rosa damascena Mill.) cultivars from North Indian hills. Nat. Prod. Res. 25: 1577-1584

131. de March CA, Ryu S, Sicard G et al (2015) Structure-odour relationships reviewed in the postgenomic era. Flavour Frag. J. 30: 342-361

132. Mitsui T (1997) New cosmetic science. Elsevier Science, New York

133. Sharma P, Ghosh A, Tudu B et al (2015) A quartz crystal microbalance sensor for detection of geraniol in black tea. Ieee Sens. J. 15: 1178-1185

134. Mitachi S, Sasaki K, Kondoh M et al (2005) Odor sensing in natural environment using quartz crystal resonators: Application to aroma sensing of roses cultivated in an outside garden. Acta Horticulturae: 113-119

135. Sarafoleanu C, Mella C, Georgescu M et al (2009) The importance of the olfactory sense in the human behavior and evolution. J. Med. Life 2: 196-198

136. Croy I, Negoias S, Novakova L et al (2012) Learning about the functions of the olfactory system from people without a sense of smell. Plos One 7: 33365

137. Malnic B, Hirono J, Sato T et al (1999) Combinatorial receptor codes for odors. Cell 96: 713-723

138. Knape K, Beyer A, Stary A et al (2009) Evolutionary trace of human odorant receptors of chromosome 17. Flavour Frag. J. 24: 192-197

139. Oh EH, Lee SH, Lee SH et al (2014) Cell-based high-throughput odorant screening system through visualization on a microwell array. Biosens. Bioelectron. 53: 18-25

140. Lee SH, Jin HJ, Song HS et al (2012) Bioelectronic nose with high sensitivity and selectivity using chemically functionalized carbon nanotube combined with human olfactory receptor. J. Biotechnol. 157: 467-472

141. Son M, Cho DG, Lim JH et al (2015) Real-time monitoring of geosmin and 2-methylisoborneol, representative odor compounds in water pollution using bioelectronic nose with human-like performance. Biosens. Bioelectron. 74: 199-206

142. Schmiedeberg K, Shirokova E, Weber HP et al (2007) Structural determinants of odorant recognition by the human olfactory receptors OR1A1 and OR1A2. J. Struct. Biol. 159: 400-412

143. Massberg D, Simon A, Haussinger D et al (2015) Monoterpene (-)-citronellal affects hepatocarcinoma cell signaling via an olfactory receptor. Arch. Biochem. Biophys. 566: 100-109

144. Denisov IG, Baas BJ, Grinkova YV et al (2007) Cooperativity in Cytochrome P450 3A4 LINKAGES IN SUBSTRATE BINDING, SPIN STATE, UNCOUPLING, AND PRODUCT FORMATION. J. Biol. Chem. 282: 7066-7076

145. Hollenstein K, de Graaf C, Bortolato A et al (2014) Insights into the structure of class B GPCRs. Trends Pharmacol. Sci. 35: 12-22

146. Lim JH, Park J, Ahn JH et al (2013) A peptide receptor-based bioelectronic nose for the real-time determination of seafood quality. Biosens. Bioelectron. 39: 244-249

147. England CG, Ehlerding EB, Cai W (2016) NanoLuc: a small luciferase is brightening up the field of bioluminescence. Bioconjug. Chem. 27: 1175-1187

148. Luker KE, Luker GD (2008) Applications of bioluminescence imaging to antiviral research and therapy: multiple luciferase enzymes and quantitation. Antiviral research 78: 179-187

149. Turin L (2007) The secret of scent: adventures in perfume and the science of smell. Harper Collins, New York

150. Jalali-Heravi M, Parastar H, Sereshti H (2008) Development of a method for analysis of Iranian damask rose oil: combination of gas chromatography-mass spectrometry with Chemometric techniques. Anal. Chim. Acta 623: 11-21

151. Kumar A, Nadda G, Shanker A (2004) Determination of chlorpyrifos 20% EC (Dursban 20 EC) in scented rose and its products. J. Chromatogr. A 1050: 193-199

152. Greenman J, EL-MAAYTAH M, DUFFIELD J et al (2005) Assessing the relationship between concentrations of malodor compounds and odor scores from judges. J. Natl. Dent. Assoc. 136: 749-757

153. Vogt AD, Di Cera E (2013) Conformational selection is a dominant mechanism of ligand binding. Biochemistry 52: 5723-5729

국문초록

G 단백질 연결 수용체(GPCR)는 7 개의 막 통과구조를 가지고 있는 막 단백질로, 여러 질병 및 전체 상용화된 약물의 40% 이상과 관련이 있는 매우 중요한 단백질이다. 이러한 이유로 안정적이며 높은 품질의 GPCR 을 포함하는 플랫폼은 질병의 조기진단, 환경 평가 및 약물 스크리닝과 같은 다양한 분야에 적용 할 수 있는 바이오센서의 개발에 매우 유용 할 수 있다. 그동안 단백질이나 세포 유래 나노베시클, 혹은 GPCR 을 발현하는 세포와 같은 생체분자물질들을 나노재료와 결합하여 GPCR 접합 바이오센서를 개발하기 위한 많은 노력이 있어왔다. 특히, 단백질 기반 바이오센서는 민감도, 선택성, 재현성, 재사용성 및 정량 분석에서 큰 장점을 가질 수 있다. 대장균에서의 재조합 단백질의 생산은 생산성 및 편리성면에서 큰 장점이 있어 널리 사용되어 왔다. 그러나, 대장균에서의 GPCR 생산은 강한 소수성, 복잡한 전하 분포 및 상이한 막 삽입 메카니즘으로 인해 여전히 한계가 있다.

GPCR 의 구조형성기술은 보다 안정하고 정확한 수용체 기반 연구를 위한 중요한 기술로 여겨져 왔다. 이러한 기술은 결정구조분석, 수용체 신호 및 약리학 연구에 대한 기본 지식을 습득하기 위해 연구되어왔다.

또한 많은 연구에서, 순도 높게 정제되고 구조형성된 수용체가 천연 수용체 구조 및 결합 주머니를 모사할 수 있다고 보고하고 있다. 특히, 수용체가 내장된 나노디스크는 수용체/리간드 결합에 대한 정량적 및 생물 물리학적 분석을 위한 강력한 방법으로 여겨지며, 식품 품질, 질병 진단 및 약물 상호 작용 연구등과 관련된 실용적인 바이오센서의 개발에 실질적으로 사용될 수 있다.

본 논문에서 GPCR 은 대장균에서 과량생산 되었으며, 계면활성제를 통해 용해 되었고, 컬럼 크로마토그래피를 통해 고순도로 정제되었다. 이후 미셀 또는 나노디스크로 정제된 수용체의 구조형성이 성공적으로 최적화 되었고, 그 특성들이 분석되었다. 또한 수용체의 결합 특성은 세포기반 분석에서의 반응과 비교함으로써 확인되었다. 이렇게 정제 및 구조형성된 수용체들은 단백질 기반의 고성능 바이오 센서 플랫폼을 개발하기 위해 전계 효과 트랜지스터(FET) 인 나노전자센서에 적용되었다.

먼저, 수용체 작용 및 길항작용 연구를 위해 수용체기반의 작용제 및 길항제 분석방법이 개발되었다. 도파민 수용체 D1(DRD1) 이 기능화된 FET 시스템은 FET 및 구조형성된 DRD1 단백질을 결합함으로써

구성되었으며, 이것은 종래의 세포기반의 수용체 분석법을 대체할 수 있는 방법으로 개발되었다. DRD1 을 정제 및 구조형성하여 DRD1 의 작용제와 길항제에 대해 효과적으로 구분할 수 있는 자연유래의 수용체 결합주머니를 모방하였다. 개발된 DRD1 나노하이브리드 FET 의 도파민 작용제 및 길항제에 대한 매우 민감하고 선택적인 특성은 실시간 반응을 통해 확인되었고, 최대 응답 레벨 또한 DRD1 친화력에 따라 성공적으로 구분될 수 있었다. 결과적으로 수용체기반의 플랫폼을 통해 수용체 작용 및 길항작용을 성공적으로 분석할 수 있었다.

둘째로, 기능을 갖는 수용체의 안정화를 위해 수용체가 내장된 나노디스크가 성공적으로 최적화되고 조립되었다. 사망 관련 악취냄새인 카다베린에 결합하는 미량아민 관련 수용체 13c(TAAR13c)는 대장균에서 생산되어 정제되었고, 나노디스크로 성공적으로 재구성되었다. 이의 특성은 트립토판 형광 분석, 동적 광 산란 분석 및 주사 전자 현미경 분석을 통해 확인되었다. 또한 부유전극이 있는 탄소나노튜브 기반 FET 에 방향성 있게 고정화 되었다. 이러한 나노디스크 기반의 바이오 센서는 민감도와 선택성 측면에서 높은 성능을 보였다. 또한 식품

신선도 결정을 위한 다양한 실제 식품 샘플분석에서도 정량적으로 카다베린을 측정할 수 있었다.

셋째로, 액체 및 기체 표적물질을 검출하는 고성능 바이오 센서 플랫폼을 개발하기 위해 TAAR13c 나노디스크(T13NDs)가 결합된 전도성 고분자 나노입자 기반의 FET 가 성공적으로 개발되었다. 이 플랫폼에서 T13NDs 는 자연 수용체의 천연결합 주머니를 모방 할 수 있었으며 수성 및 대기환경에서 높은 안정성으로 존재할 수 있었다. 또한 전도성 고분자 나노입자를 통해서 센서 민감도를 높이고 FET 에 나노디스크를 방향성 있게 고정화시킬 수 있었다. 이러한 나노디스크 기반의 바이오센서는 높은 안정성과 신뢰성은 물론 수성조건에서 높은 민감도와 선택성을 가질 수 있었다. 또한, 기체 표적물질 검출의 경우도, 높은 민감도, 안정성 및 재사용성을 나타내며 기체상태의 카다베린을 성공적으로 검출 할 수 있었다.

마지막으로, 인간의 감각 반응을 모방하도록 인간과 같은 성능의 바이오전자코가 수용체 기반 플랫폼을 통해 성공적으로 구성되었다. 인간의 후각 수용체 1A2 가 내재된 나노디스크(hOR1A2NDs)를 조립하여 CNT-FET 의 부유전극에 부착시켜 바이오전자코를 구현하였다.

hOR1A2NDs 는 장미 향기 분자에 특이적으로 반응했으며, 이는 전기적 신호분석법을 통해 성공적으로 모니터링되었다. 이러한 수용체기반의 바이오전자코는 민감도와 선택성을 가지고 특정 장미향에 대한 정량적인 평가를 가능하게 하였다. 이를 통해 증강물질에 의한 장미 향기에 대한 hOR1A2ND 의 인간의 코와 유사한 반응 또한 성공적으로 입증되었다. 더욱이, 이러한 방법은 장미 오일과 같은 실제 샘플에서 장미향 성분을 정량적으로 평가할 수 있었다.

결과적으로 단백질 기반의 바이오 전자센서는 민감도, 선택성, 재현성, 안정성 및 정량 분석 측면에서 높은 성능을 보일 수 있었다. 또한, 이를 통하여 수용체 작용 및 길항 작용과 인간 후각반응을 성공적으로 모방할 수 있을 뿐만 아니라 액체 및 기체 표적 분자까지 성공적으로 검출할 수 있었다. 이러한 단백질 기반의 플랫폼은 실제 바이오센서를 향한 나노바이오기술의 진보를 나타내는 수용체 기반 감지 접근법의 실용적인 방법으로 사용될 수 있을 것으로 기대된다.

주요어: G 단백질 연결 수용체, 대장균, 정제, 구조형성, 나노디스크, 바이오센서

학번: 2014-30249